ECI Final Report: Closing of Critical Technology Gaps for Rotating Detonation Rocket Engines

Principal Investigator and Project Manager: Thomas Teasley ER13 MSFC

Project Start Date: 10/3/2022
Project End Date: 10/31/2024
TechPort ID Number:

Contributing Early Career Team Members:
Jonah Burgin ET10 MSFC
Tessa Fedotowsky ER41 MSFC
Kendall Feist ET10 MSFC
Dillon Petty ER13 MSFC
Shawn Skinner ER41 MSFC
Robert Thacker LTC0 GRC
Benjamin Williams ER13 MSFC

ECI Mentors:
Michael Allison - ER12 MSFC
Doug Perkins LTA0 GRC

Industry Partner
Venus Aerospace, Houston, Texas, 77034, United States
Primary Contacts: Hannah McCallum and Wade McElroy

Table of Contents

1 OVERVIEW

NASA has successfully fired several configurations of a dual regenerative 10K lbf class Rotating Detonation Rocket Engines using cryogenic liquid methane, liquid hydrogen, and RP-1 as fuel and liquid or gaseous oxygen as the oxidizer. In addition, 3 hot fire test phases were conducted to evaluate parametrically varying combustor geometries using a subscale 500-1K lbf class thruster RDRE. Several studies were successfully completed to evaluate the impacts of contraction ratio, annulus L', heat transfer through calorimetry, and varying injector designs. Laser powder bed fusion GRCop-42, GRX-810, and C-103 alloys were used for the outer bodies, inner bodies, nozzles, and injector variations. The development of RDRE technology is only now possible with additive manufacturing techniques and these specialized alloys. Critical design parameters, design rules of thumb, and operability limitations have been identified. Major lessons learned in the development of critical components have also been documented. All critical technology gaps have been demonstrated at one scale or another and closed. A major finding of this work is that the combustion efficiency of the RDRE is far superior to that of the traditional liquid rocket engine requiring an order of magnitude lower chamber volume and residence time to react. Because of this, the design trade space opens up significantly. More compact chamber geometries are now possible with potential mass savings and significant length savings possible to flight geometries. In addition, the ceiling for the technology, in terms of Isp, has not yet been reached. It is likely that an additional ~10% better Isp over equivalent state-of-the-art combustion devices may be achieved over the next decade should the technology continue to be developed. This technology has been shown to be viable for near term infusion (2-5 years) into space missions and enable cost effective space access for US industry. This final report documents all major findings from this early career initiative (ECI) project and lays out what is needed post ECI.

2 INTRODUCTION

NASA's development of detonative combustion devices such as the rotating detonation rocket engine (RDRE) has continued past the successful feasibility work conducted in 2022. That project successfully integrated additive manufacturing techniques and novel extreme environment alloys such as GRCop-42 and GRCop-84 to demonstrate flight relevant durations with multiple hot fires lasting longer than 100 seconds [1]. In those efforts, Marshall partnered with IN Space LLC and Purdue University who contributed design requirements, operability limits, and sizing of components. Following that success, NASA Space Technology Mission Directorate (STMD) funded an early career initiative (ECI) project seeking to close the remaining critical technology gaps preventing widespread use within industry. These technology gaps were determined through discussion with industry some of which were chosen as Key Performance Parameters (KPP) for this work and are listed in Table 1.

Table 1. Critical technology gaps for RDRE.

Description	Quantification
Reduced Injection Pressures	ΔP/Pc = 50-100% and < 500 psid
Integrated Ignition	10 stable starts or greater
Self-sustained cooling	No reliance on secondary systems
Hardware Duty Cycle	10 starts at >500 seconds total duration
Scalability of Thrust	5-10 klbf (Vac); thrust design dependance

NASAs first efforts in this follow-on work was aimed at testing a 10K lbf class RDRE and was conducted during the late summer of 2023. The hardware designed, developed, and tested is dubbed SWORDFISH. This hardware made use of key lessons learned from the previous 2022 work. The primary industry collaborator selected and approved by the Space Technology Mission Directorate (STMD) under the ECI was Venus Aerospace who contributed design requirements, supported critical hardware design and development, data analysis, and strategies for test. The project was broken up into 3 phases, determined by which propellant combinations were used. Phase 1 utilized liquid methane and liquid oxygen in a dual regenerative configuration (Figure 1), phase 2 utilized liquid hydrogen and liquid oxygen in a dual regenerative configuration, and phase 3 was actively cooled with de-ionized water while directly injecting Kerosene /LOx.

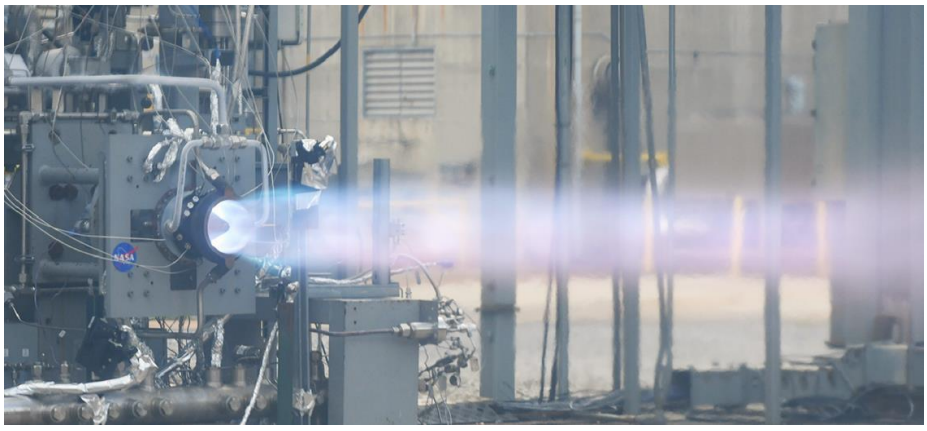

Figure 1. Phase 1 testing of NASA SWORDFISH in a dual regenerative configuration using LCH_4/LOx.

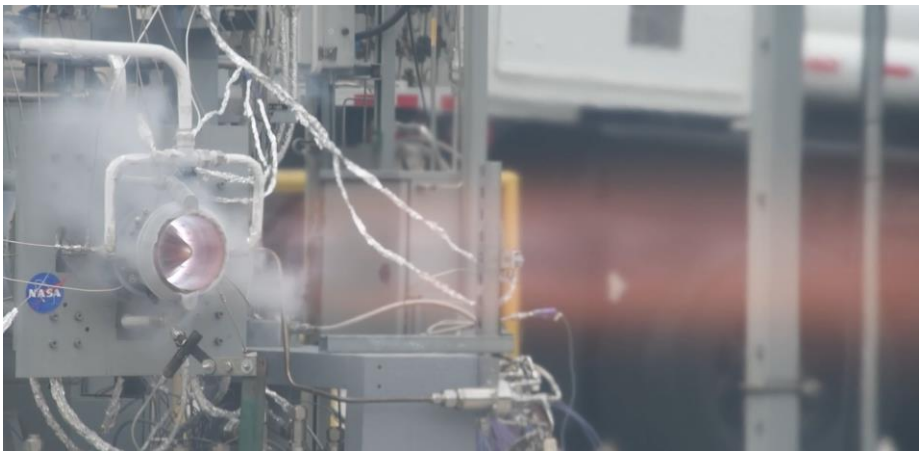

Figure 2. Phase 2 testing of NASA SWORDFISH in a dual regenerative configuration using LH_2/LOx

Figure 3. NASA RDRE pivotal hot fire test using RP1/oxygen.

2.1 CHAMBER HARDWARE

All hardware was produced using laser powder bed fusion GRCop-42 or a new alloy called GRX-810. GRX-810 is a Ni-Co-Cr superalloy designed specifically for extreme environment operation under the NASA ORCA project. The alloy was originally demonstrated as a viable injector and nozzle material using NASAs constant pressure 7K lbf class liquid rocket engine hardware, results of which will be presented at this conference. Images of RDRE hardware during processing and development are shown in Figure 4.

Figure 4. From left to right, computer rendering of thrust chamber assembly, inner body and outer body manifold post print, and outer body post print.

Several different configurations of chamber hardware were tested. Contraction ratio (CR) was varied from 1.0 to 1.7 achieved by a gradual contour along either the inner, outer, or both walls meeting at a minimum area constriction at the throat. Pertinent design parameters are provided in Table 2 for all the configurations tested.

Figure 5. Hardware contours for phase 1 and phase 2 hot fire testing.

Table 2. Phase 1 and 2 hardware critical parameters tested.

Configuration Tested	Contraction Ratio	Design Throat Area (in^2)	Expansion Ratio
OB1 + IB1	1	8.284	4.01
OB1 + IB1.1	1.13	7.341	4.52
OB1.3 + IB1	1.3	6.379	5.20
Stub OB1.3 + IB1	1.3	6.379	2.69
OB1.7 + IB1	1.7	4.908	6.76

The annular geometry used under phase 1 and 2 testing had a gap width of 0.455 inches and an outer body diameter of 6.25 inches at the injection plane. Three of the four outer body configurations had an exit diameter of 6.5 inches that terminated at the inner body plug nozzle tip. The final outer body configuration shown in Figure 5 is an outer body with truncated nozzle expansion section dubbed the stub outer body. This variant of hardware also created a subsonic area ratio of 1.3 with Inner Body 1. This was done to identify the proportional contribution of heat input from the nozzle section relative to the chamber section. A primary goal of the hardware configurations tested was to ascertain the impact of contraction ratio (CR) on total chamber heat load. It was determined that the inclusion of CR only served to amplify the total heat input into the walls of the hardware. Comparing to previous data, a scaling factor was found to exist that closely matches the total heat load trends of the current hardware. In essence, with this scaling it is possible to collapse the total heat load regardless of the fluid used to cool the hardware.

Four total injectors were manufactured and tested. Three of which were tested under the methane test phase and one tested under the hydrogen test phase. One injector was tested under both phases with an additional chemical mechanical polishing (CMP) step added to increase the injection flow area of the fuel and oxidizer circuits to reduce unwarranted pressure losses.

Initial design points were injection stiffnesses of 50% and 75% $\Delta P/Pc$ at a mean chamber pressure of 650 psia. However, print shrinkage, higher than anticipated heat loads, and reduced

combustion performance in methane testing resulted in much higher stiffnesses. Those data were then utilized to iterate on orifice design such that both hydrogen injectors would have a true stiffness of 50% and 30% ΔP/Pc at 650 psia chamber pressure.

2.2 LIQUID OXYGEN COOLING

After completion of feasibility testing under the ACO, it was identified that fuel cooling alone is insufficient and oxygen cooling is a prerequisite for any RDRE design [1]. This is particularly the case for thrust classes below about 15,000 lbf. Above this thrust class cooling only with fuel may become viable depending on cooled surface area and other factors such as mean operating pressure. The initial work completed during phase 1 testing successfully demonstrated cooling of the inner body with liquid oxygen. Several design and post processing requirements were implemented to enable successful oxygen cooling. This section documents those requirements and post processing assumptions.

The requirements for oxygen cooling are below.

1. Hot wall thicknesses must exceed a specific limit to prevent leaks from high porosity.
2. A thorough cleaning processes removed all machining chips and oils post machining.
3. Chemical Mechanical Polishing (CMP) was applied to the coolant channels to reduce wall surface roughness, remove excess wall powder and machining particulates, and minimize pressure losses.
4. Oxygen cleaning per MSFC-SPEC-164E Class IIIA.

The primary concern for a minimum hot wall thickness are instances of leaks from high porosity or witness lines. No leaks are acceptable on a component being cooled with oxygen as the likely point of total failure would be at the point of the leak.

Several methods were used to ensure the chamber was clean, with the primary focus being removal of machining chips and lubricants. Common detergents in addition to inert gas and water purges were used in most cases. Light shaking of the component was first used to remove the bulk of machining chips followed by a borescope inspection. After it was determined that the majority of the chips were removed, water was flowed in both the reverse and forward directions. Initial water flow was conducted at low mass flow rates to verify chip and powder removal before proceeding to higher flow rates. Next, the component was placed in a detergent bath and scrubbed until clear of all machining lubricants. Internal manifolds were partially filled with water and shaken to help dislodge and remove larger and compacted machining chips. Finally, a high-pressure inert gas purge was applied in the forward and reverse flow directions. In some cases up to several hundred psi was measured within the inlet manifolds. This also served as the drying step post water flow procedures. A final inspection was conducted with a borescope to confirm all visible chips are removed.

The next post-processing step was a CMP protocol that was previously developed under the RAMPT/ORCA project with REM Surface Engineering. Extrusion honing or other polishing techniques may also be used with similar results. An added advantage of the chemical component of CMP allowed for dislodging of unseen machining chips and dissolving of fine powder and chips adhered to internal passages. Once received back from REM Surface Engineering, the water flow and inert gas purges were repeated to gain certainty in a cleared part. Flow resistance measurements were taken before and after CMP, with a reduction in resistance of 25%. This roughly equates to a reduction in pressure loss, using cryogenic fluids, of about 70% as previously identified under the RAMPT project.

Finally, oxygen cleaning per MSFC-SPEC-164E Class IIIA was chosen such that the maximum number of particles did not exceed >800 microns in diameter per 0.1 square meters and the nonvolatile residue is measured to be a maximum of 1 mg/0.1 square meters. This methodology ensured no instances of burn through were caused by particle impact ignition or compression heating of coolant.

2.3 PLUG NOZZLE CLOSEOUT

In addition to the manufacturing and post processing steps implemented, another design consideration was the incorporation of fluid bypass orifices. These orifices relieved pressure and reclaimed potential pressure losses near the tip of the plug nozzle where heat fluxes are relatively low.

An inevitable outcome of a plug or aerospike nozzle geometry is the need to reverse flow direction of regenerative coolant. As the plug crossectional area decreases moving away from the chamber exit plane, flow area of the coolant channels also decreases. Thus, at some point, the tip of the nozzle is required to be solid and rely solely on passive cooling from the internal manifold where flow direction is reversed. The geometry under phase 1 and 2 survived with minimal discoloration but did have some copper deposition from within the annulus.

Figure 6. Images of the plug nozzle solid tip post hot fire.

This design feature will be further incorporated into future hot fire test projects with RDREs.

3 EXPERIMENTAL DATA – METHANE TEST PHASE 1

Hot fires were performed using Test Stand 115 at MSFC utilizing throttling with a bypass line and cycle sequencing. Both the fuel and oxidizer lines had separate bypass legs with isolated venturis to control additional flow rate into the combustor. During any given hot fire, the main lines would open supplying a baselined flow rate to start, followed by a sequence of valve open and close commands at different intervals. This effectively allowed for multiple set points in a single test to be explored. Specifically, a low-pressure baselined mixture ratio, the fuel bypass valve then opens thus supplying a higher total mass flow rate at lower mixture ratio, followed by the Ox bypass valve thus matching mixture ratio from startup but at a higher total mass flow rate, and finally followed by closure of the fuel bypass valve thus reducing mass flow rate and increasing mixture ratio. A plot of all test conditions explored is shown in Figure 7.

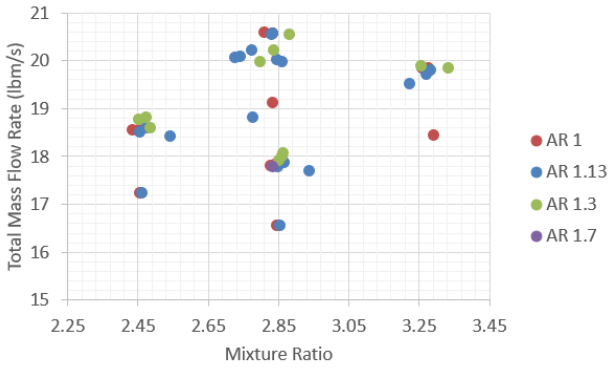

Figure 7. Total mass flow rate and mixture ratio for all tests conducted with each chamber configuration.

In addition to adjusting operating conditions during hot fire, a handful of cycle tests were also conducted. This is where the RDRE is shutdown and reignited with modifications made to the tank pressure thus allowing the sequence to be rerun at a slightly different inlet condition. This test methodology is considered to be aggressive with higher risk placed on hardware. However, the payoff in experimental data is high. For "hardware rich" test projects such as this one made possible only by additive manufacturing, this was considered a favorable trade.

Most of the hot fire test cases showed a single wave which often traveled in the clockwise direction. Figure 8 shows a still image of this single wave mode from high-speed video.

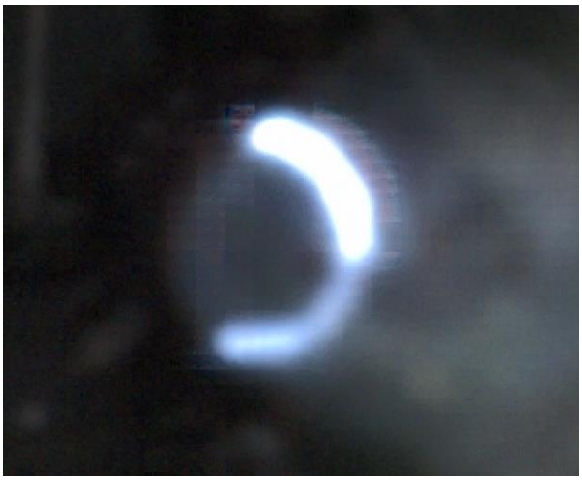

Figure 8. Single wave traveling clockwise about the annulus.

3.1 VALIDITY OF TIME AVERAGE PRESSURE MEASUREMENTS

In all hardware, measurements of time-averaged total or static pressure were obtained at the injector face, P_0, and at the geometric throat, P_t, where the minimum area occurred. In traditional liquid rocket engines, the measurement at the injector face has been found to match the total pressure measured at the nozzle contraction inlet, $P_{c,ns,}$ after correction for Rayleigh Flow losses. If the constant pressure combustor does not have a geometric throat and is thus an open cylinder with CR of 1, then the loss in total pressure is expected to be maximized. The nozzle inlet total pressure in this case would be approximately 81% of the measured value at the injector face. As such, it is expected that a straight open annulus should show the same detriment if the total pressure were computed from the throat pressure and compared with the measured P_0. As the

Mach number is decreased, via increasing the CR, the loss is expected to decrease but not completely go away. Since P_t was directly measured and the average P_0 and P_t were far above the ambient atmospheric pressure, then the Mach number at the throat can be approximated to be 1. Using isentropic flow, the $P_{c,ns}$ can be computed and directly compared with P_0 a plot of which is shown in Figure 9.

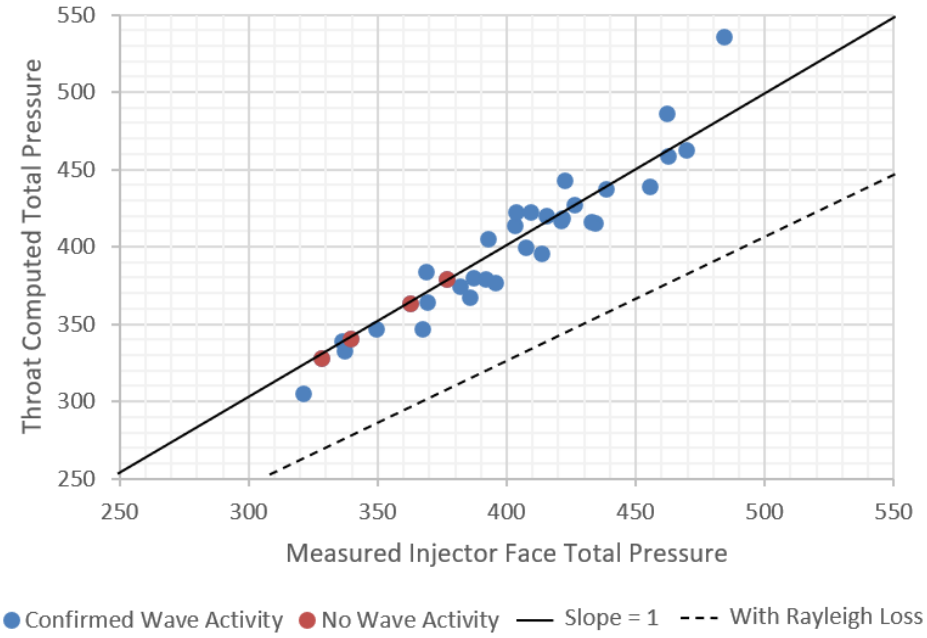

Figure 9. Throat computed total pressure as a function of measured injector face total pressure.

It is apparent that all test cases fall close to the line with slope of 1, the solid black line, while they should have been much closer to the dashed black line assuming Rayleigh losses apply. Even cases where no wave activity was observed showed what appears to be no loss in total pressure. The percentage of theoretical constant pressure engine total pressure is plotted against the Rayleigh loss factor for the different CR tested in Figure 10.

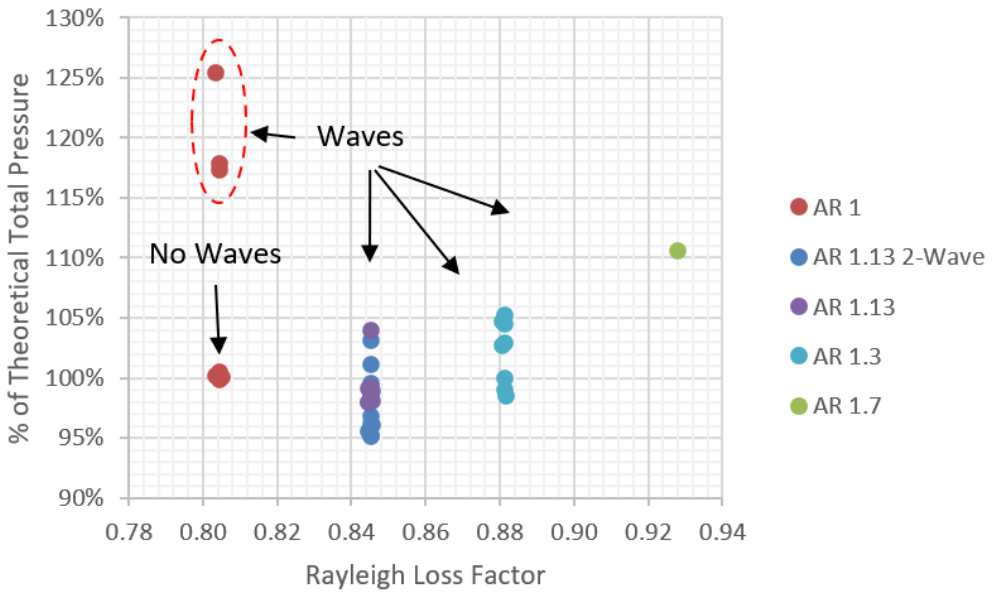

Figure 10. Percentage of theoretical constant pressure calculated total pressure as a function of Rayleigh loss factor for different contraction ratios and wave conditions.

This quantity is the ratio of the measured injector face total pressure to the total pressure, $\frac{P_{1,ns}}{P_0}$, computed from the throat static pressure using isentropic flow relations (assuming Mach 1 at the throat). In all cases, this value appears to be minimized at a CR of around 1.13. The practical and physical meaning of this is unclear and likely will need to be elucidated with CFD. Cases where no wave activity was observed, and thus operating in a deflagrative mode, are comparably lower in % of P_0 in contrast to cases with waves. As such, the application of the Rayleigh loss should apply to these cases and by proxy to all other cases as well since the geometry tested is not a perfectly ideal RDRE.

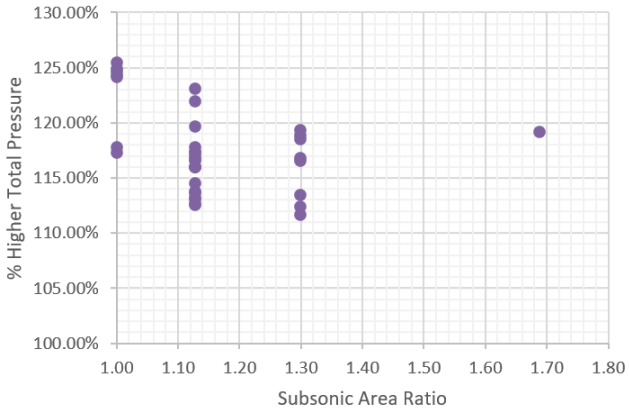

Figure 11. % higher total pressure as a funtion of contraction ratio.

The percentage higher total pressure is computed from $\frac{P_{1,ns}}{P_0 * R_l}$ where $R_l = \frac{\left(1+\left(\frac{\gamma-1}{2}\right)\right)(CR^{-1.639})^{2\left(\frac{\gamma}{\gamma-1}\right)}}{(1+\gamma)(CR^{-1.639})^2}$ and $M = CR^{-1.639}$. CR is the contraction ratio, M is assumed to be the mean Mach number in the annulus, and R_l is the computed Rayleigh loss for the configuration. Mach number is simply related to the CR via best fit curve. These data are shown in Figure 11. All test cases have at least an increase of 11% in total pressure with respect to what the total pressure

should be for a constant pressure combustor. A quantity that may better explain these measurements is the equivalent available pressure (EAP) [2]. This quantity is used to compare thrust potential between steady and unsteady combustion devices.

Several tests were chosen to compute the equivalent available pressure, or EAP. However, experimental EAP as described in [2] presumes an RDE with only an exit throat (i.e., the RDE terminates at station 8 per [2]). For the present experiment this presumption requires the subtraction of the thrust produced by the expanding portion of the nozzle. This force contribution was computed from time averaged static pressure measurements obtained through evenly spaced CTAPs along the outer body nozzle expansion section in conjunction with a known channel crossectional area profile. A potential source of error with this method is that it assumes the same wall static pressure profile on the inner body plug nozzle as the outer body shroud nozzle. The static pressure was directly measured down the length of the outer body nozzle section alone. It was not possible to place static pressure measurements on the inner body due to its design complexity. A computational fluid dynamic (CFD) study of an RDRE nozzle similar to the one used in [3] showed that the inner and outer body profiles can be different, on the order of 15-25% in wall surface pressure, or a 4-7% increase in EAP. The geometry assumed and hot wall static pressure is shown in Figure 12.

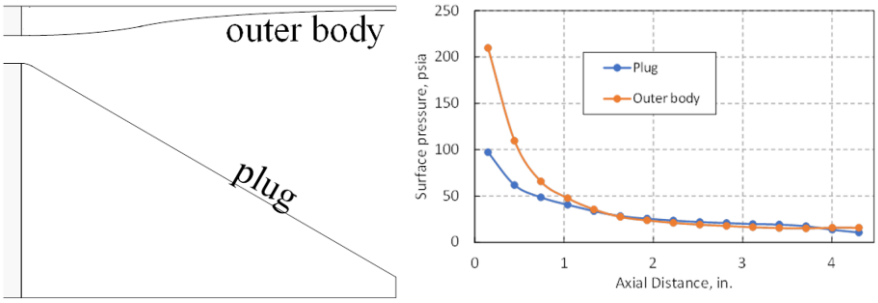

Figure 12. CFD modeled nozzle expansion section geometry (left) and wall surface pressure for the plug and outer body nozzle (right). Courtesy of Dr. Dan Paxson NASA GRC.

Thus, the assumption of the same wall static pressure profile for the inner body plug nozzle as what was measured on the outer body shroud nozzle would reduce the true throat level thrust and the computed EAP. Table 3 shows the resultant EAP and percentage of measured injector face pressure for each test case.

Table 3. Select tests to compute EAP.

Test	Level	EAP (psia)	% of Injector Face Measured Pressure
`001*	2	306	93.4
`002	2	379	93.9
`008	2	462	95.4

*no waves observed for this test.

These three test cases consistently show that the computed EAP is in the mid-90's as a percentage of the actual measured injector face total pressure. Incorporating back in the assumption of lost throat level thrust from higher nozzle thrust would only increase that percentage, presumably to be very close to 100%. This is not to say that the expected percentage of the time averaged injector face pressure divided by the expected true EAP should be 100%. Only that with the assumptions and measurements made in this analysis does it appear as though the EAP would fall out to be approximately the same as the measured time averaged injector face pressure.

Further work is needed to understand how EAP compares with the measured injection plane total pressure. It does appear given the current limited analysis that these quantities are not completely dissimilar.

3.2 SPECIFIC IMPULSE AND COMBUSTION EFFICIENCY

The relative completion of combustion, C*, assumes Mach 1 at the throat, time-averaged mass flow rate into the combustor, and a computed total pressure measured from the throat. However, often this measurement is difficult or not possible to obtain thus translation from the injector face measured total pressure (assuming Rayleigh losses apply) is often used instead. In these hardware, C* was computed using both the injector face pressure, $P_{c,0}$, and throat computed total pressure, $P_{c,ns}$. This is also because the only critical pressure measurement from a systems perspective within the chamber is the injection plane static pressure (assumed to be close to the total pressure). This value determines the power balance and required pressure loss across the injector face. The total pressure can only be > the static pressure at the injection plane.

Thrust was measured using the previously validated NASA MSFC thrust measurement system [1], [4]. Total mass flow rates of propellants were measured via previously characterized cavitating venturis. All quantities were then compared directly with NASA CEA theoretical quantities at the same average total pressure and mixture ratio. Figure 13 shows the reduced η_{Isp} as a function of η_{C^*} (P_0 and $P_{c,ns}$) for varying CR configurations.

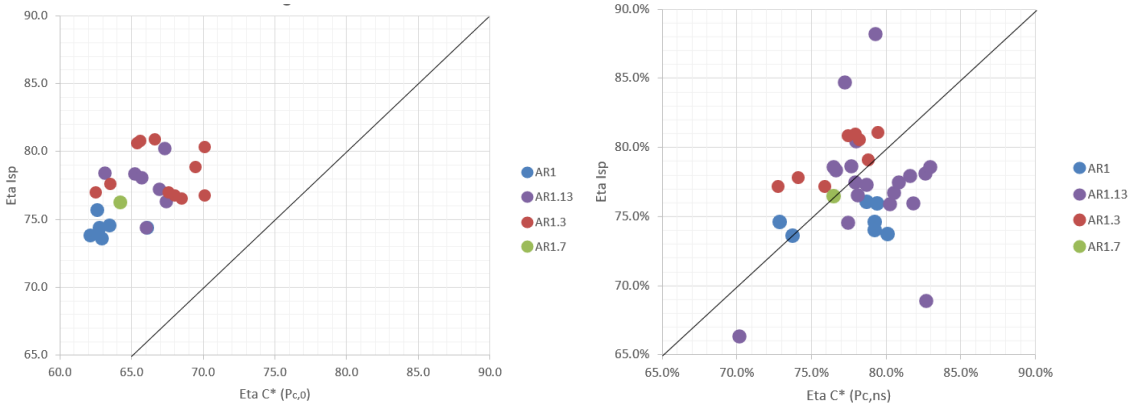

Figure 13. η_{Isp} vs η_{C^*} (P_0 and $P_{c,ns}$) for varying CR configuration with a line of slope = 1.

The hardware tested did not yield performances close to 100%. This is in contrast to the experimental results presented in [1] where η_{Isp} approached values > 90%. A major difference in this hardware relative to the hardware tested in [1], is the gap width. The gap width was increased to 0.455 inches from 0.33 inches.

Looking more closely at the relative magnitudes of efficiencies in Figure 13, the first plot computed from total pressure measured at the injector face shows Isp efficiencies well above that of C* efficiencies. This contrasts with what is expected given their linear relationship assuming similar trends to steady flow liquid rockets where $\frac{C_F * C^*}{g_0} = Isp$. It is expected that the % efficiency of Isp should lag slightly behind the % efficiency of C*. This has been confirmed with constant pressure engines where that lag percentage is usually 1-3% for well-designed combustors. The exception to this rule of thumb is very large thrust class engines. Looking at the second plot in Figure 13, the data aligns more closely with a line of slope = 1. These data are computed with $P_{c,ns}$. However, multiple test cases are still showing Isp above the line with slope of 1. Put simply, the measured specific impulse is far higher than it should be given the measured injector face stagnation pressure. Similarly, the throat stagnation pressure is far higher than it should be relative to what is expected in a constant pressure rocket.

To further expand on observations of CR and its impact on thrust chamber performances, Figure 14 plots η_{C^*} and η_{Isp} as a function of $P_{c,0}$. In general, as CR increases the two efficiencies increase. However, the CR 1.7 case does not continue this trend. Only a single data point was obtained for this CR because the local heat flux to the wall exceeded the burnout limit and destroyed the hardware. This does represent a potential limitation to this study and to RDRE development in general. However, if the trend had held it is expected that the η_{C^*} and η_{Isp} for the CR 1.7 would have

been near 69% and 79%, respectively. Instead, it was found to be about 5% and 3% below those values. In addition, the likelihood of obtaining a single data point from the lowest bound of performance-potential is unlikely. This indicates that the reduction in performance could be statistically significant.

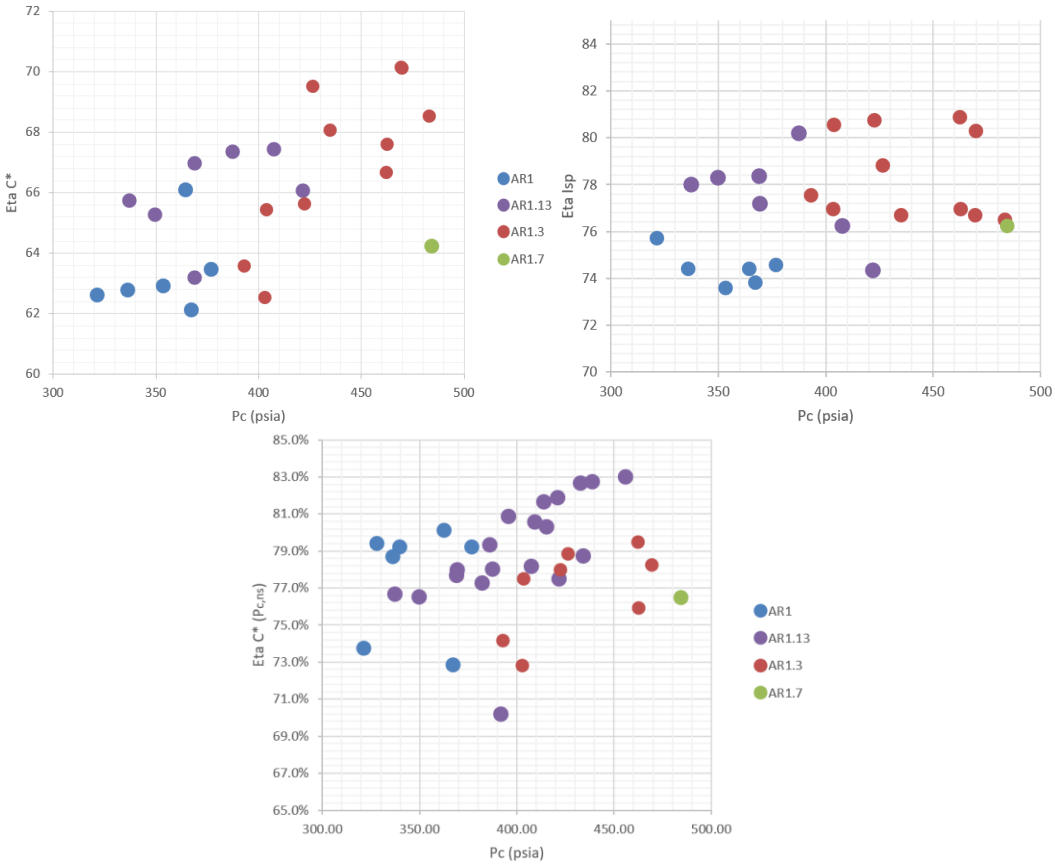

Figure 14. C* and Isp efficiency as a function of average CTAP.

Figure 15 takes all available data and averages them such that C* and Isp efficiencies can be plotted as a function of CR.

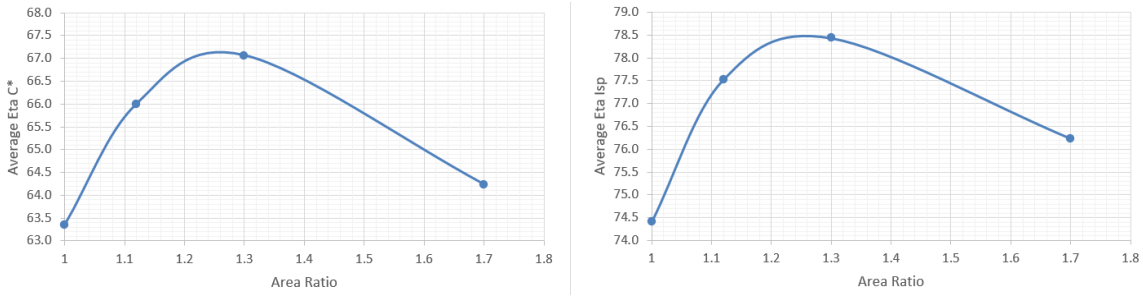

Figure 15. C* and Isp efficiency as a function of contraction ratio.

Based on these data, the ideal CR appears be about 1.25 when η_{C^*} is computed with $P_{c,0}$. However, the gains in performance may likely be due to increased burning of propellant inside the annulus rather than a direct impact on Isp. This is consistent with observations of CR and its impact on performance for a constant pressure combustor overviewed in Sutton and Biblarz [5]. This result may be ideal given experimental heat flux data obtained and presented in another paper. For cases

where the CR exceeded 1.3, the heat input to the chamber walls was found to be so extreme that existing cooling strategies and metal-alloys may not close a cooling solution at the thrust classes considered. As CR increases, the same proportion of coolant per unit wall surface area is available but at an ever-increasing wall temperature proportional to the increase in average chamber pressure.

If $P_{c,ns}$ were used to compute η_{C^*}, then the ideal CR appears to be closer to 1.13 shown in Figure 16.

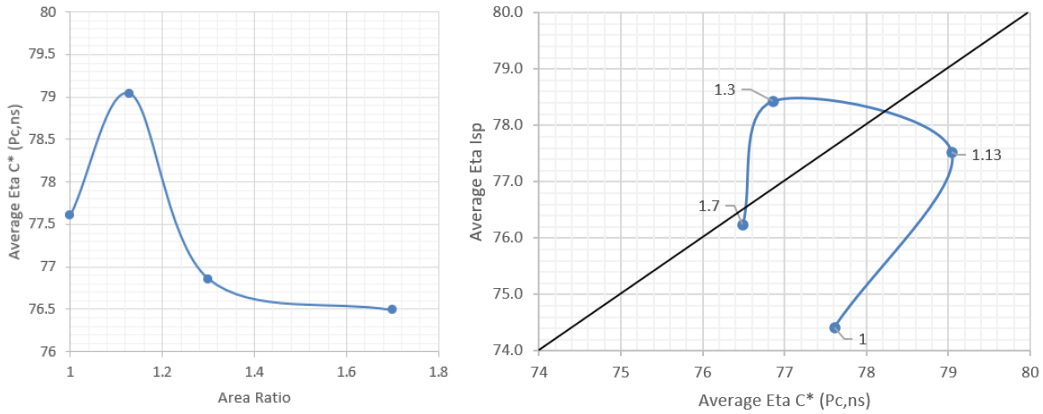

Figure 16. Average $\eta_{C^*}(P_{c,ns})$ dependance on contraction ratio and average Isp vs average $\eta_{C^*}(P_{c,ns})$.

In both plots, the highest η_{C^*} ($P_{c,ns}$) is achieved with the 1.13 CR. However, this is not the full story and Isp appears to be highest for the 1.3 CR. Another convoluting factor, such as the magnitude of chamber pressure, may be skewing Isp higher for certain cases. In addition, annulus volume is not the same for each configuration.

Figure 17 shows the average η_{C^*} (P_0) for multiple RDRE configurations in the experimental literature as a function of average chamber pressure. These data show a clear upwards trend in C* as average chamber pressure increases.

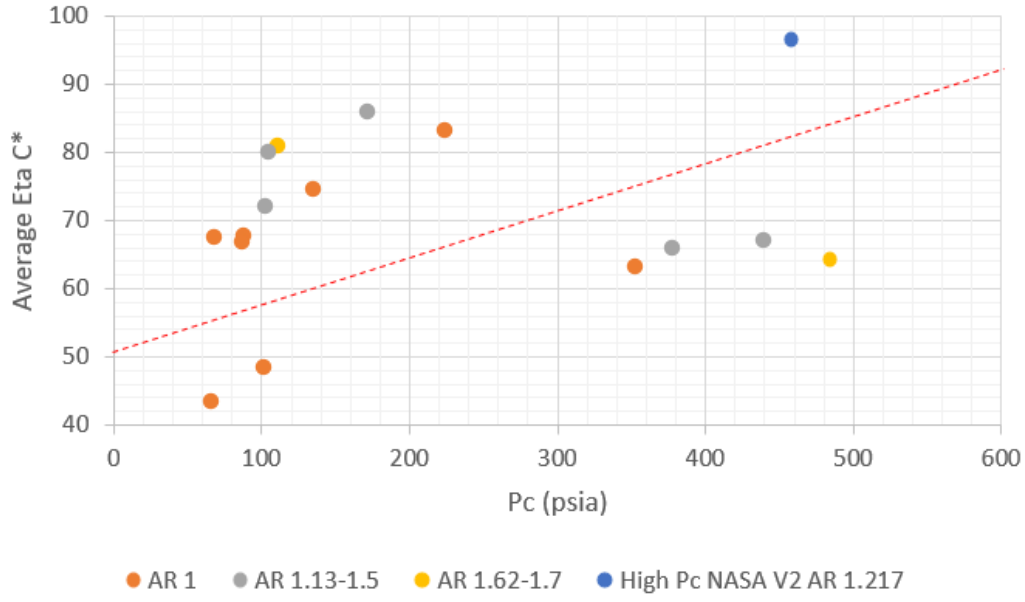

Figure 17. Average Eta C* vs Pc for various RDRE configurations in the experimental literature for various CH_4/Ox test data including [1], [6]**.**

These data illustrate the two different gap/length regimes where test data below the red dashed line have gap/length ratios > 0.12. If the annulus has a gap/length ratio of < 0.12, the propellant is able to remain within the annulus and complete combustion. This is somewhat of a feedback loop where more propellant can burn, contribute to a rise in average pressure, and thus more propellant can burn further.

To take this analysis a step further, if the data presented in Figure 17 were scaled for average chamber pressure then the two regimes collapse to an independence of η_{C^*}. This was done by taking the mean slope of the data, illustrated by the red line, and translating to a slope of 0 using the average chamber pressure of all data as the baseline. This is shown in Figure 18 where slope of the two regimes appears to be close to 0 with average head end chamber pressure.

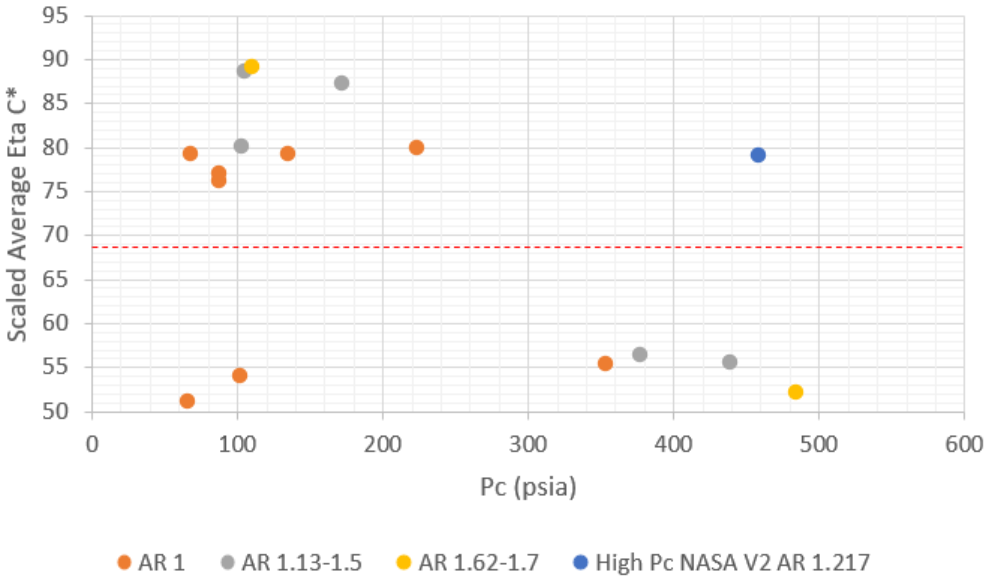

Figure 18. Scaled average η_{C^*} (P_0) as a function of average head end chamber pressure (P_0) for various CH_4/Ox test data including [1], [6]**.**

From here, scaled average plots of CR with η_{C^*} (P_0) and η_{C^*} ($P_{c,ns}$) can be shown normalized by chamber pressure.

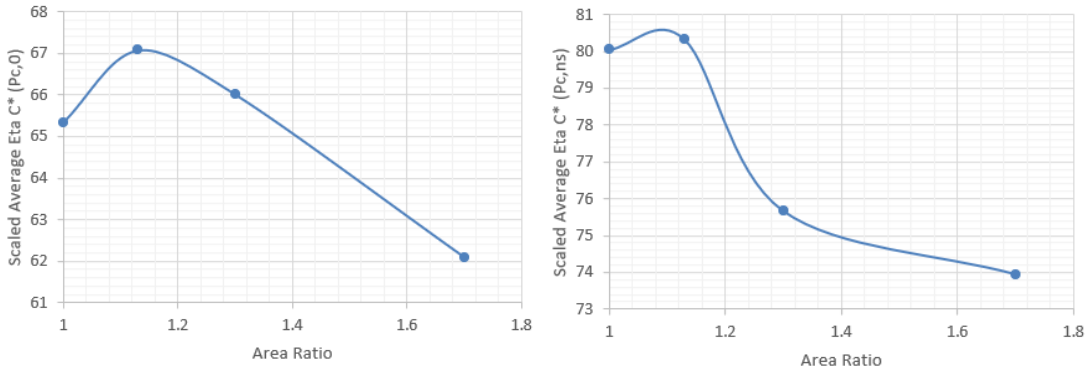

Figure 19. Plots of scaled average η_{C^*} (P_0) and η_{C^*} ($P_{c,ns}$) with contraction ratio.

These data show that C* appears to be maximized where with a slight CR with performance detriments at higher values.

To summarize, the following lessons learned have been identified.

1. CR does not appear to directly impact Isp but rather increases completion of combustion, thus increasing Isp proportionally.
2. The primary advantage to including a slight contraction appeared to be repeatability of detonation. The straight annulus was the only configuration that showed no wave activity in a handful of cases. However, this design feature may be ignored if other more important features cannot be implemented.
3. This work has identified a significant need to better understand the total and static pressure measurements made in RDREs and the role of losses and gains in average pressure.

3.3 PLUG NOZZLE FORCE ESTIMATION

A major area of concern for annular RDREs is the force contribution from the plug nozzle. The primary concern is that the plug surface sees an average pressure lower than ambient atmospheric pressure and thus experiences a net pressure drag. This will reduce the overall thrust in atmospheric operation. If the outer cowl is taken as the exit diameter, then the measured to theoretical thrust will show to be much lower than expected. To demonstrate this impact, a truncated and extended nozzle section was tested at the identical CR. These configurations are shown in Figure 1 and Figure 5. Their measured and corrected thrust as a function of total propellant mass flow rate is shown in Figure 20.

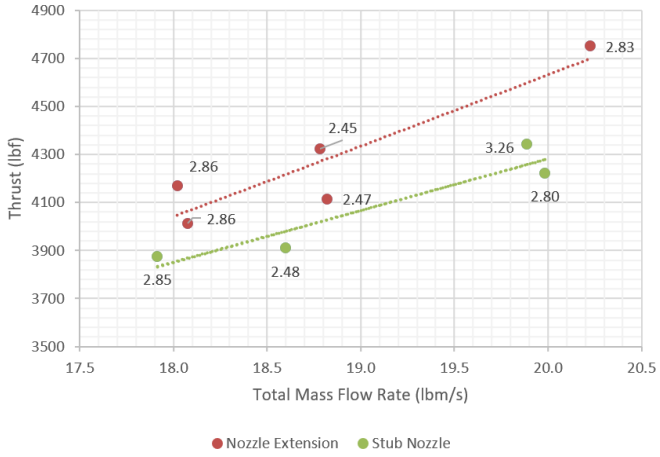

Figure 20. Measured thrust vs total mass flow rate for the stub nozzle and nozzle extension.

These data show a reduction in overall thrust for the truncated stub nozzle configuration. A significant component of this loss may be due to the outer shroud expansion angle of 30 degrees. This is a reduction in thrust from non-axisymmetric flow. A plot of thrust efficiency with nozzle exit half angle is shown in Figure 21.

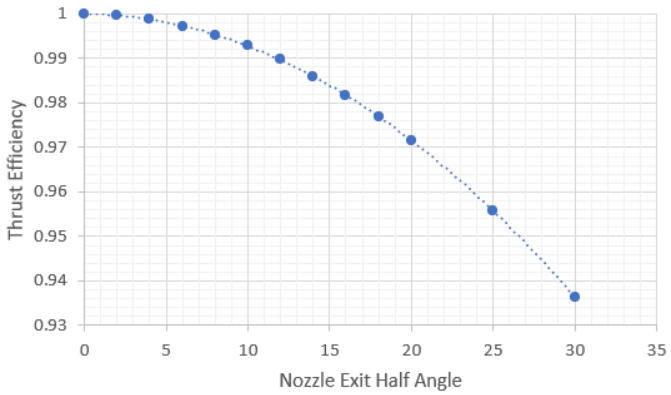

Figure 21. Thrust efficiency vs nozzle exit half angle.

With an expansion half angle of 30 degrees, the net thrust efficiency is 93.6%. The ideally computed thrust for configuration with the nozzle extension at 20 pounds per second of propellant is about 4673 lbf. With this efficiency term applied, the ideal thrust reduces to 4376 lbf. The measured thrust for the stub nozzle at 20 lbm/s is 4282 lbf meaning the remaining force on the plug nozzle reduces the force further by about 94 lbf and equates to an average wall static pressure of 5.4 psi. This shows that the net force on an unconfined plug nozzle will result in a drag force on the plug nozzle and further consideration for nozzle design will have to be given for configurations with no outer shroud nozzle extension. These findings are consistent with those of [7] using a subscale MMH/NTO RDRE.

3.4 METHANE TEST PHASE 1 HEAT TRANSFER

The impact of a nozzle extension on total heat load was also explored. These data show that the total heat load to the inner body via the plug nozzle remains unmodified with or without a shrouded nozzle section suggesting that the average wall static pressure is either comparable or the contribution of the nozzle section to total heat load is very small. Both are likely the case based on heat flux predictions.

Overall, the trends in heat load were found to be consistent with previously measured hot fire test data. The measurement errors in this study were higher due to persistent leaks in tubing caused by continuous high-power single wave modes - details of which are presented in a separate paper. The data presented in these figures are not scaled for variation in heat load measurement due to modification of the total mass flow rate of coolant. Since this combustor was dual regenerative, it was possible to maintain similar average chamber pressure while modifying the mixture ratio and thus mass flow of coolants. This does have an impact on the measured total heat load. Thus, variation in the total heat load as shown is higher than what is typical.

Finally, there was some measurement error caused by the location of the thermocouples in the system. In all cases, measurements were made on the inlet and exit lines of the hardware. This can have a fairly large impact on measurement variation but was unavoidable with this hardware due instrumentation fitment constraints from facility interfaces. Future designs will integrate measurement capability within inlet and exit manifolding reducing measurement error.

In general, an RDREs heat flux profile has 3 sections illustrated in Figure 22.

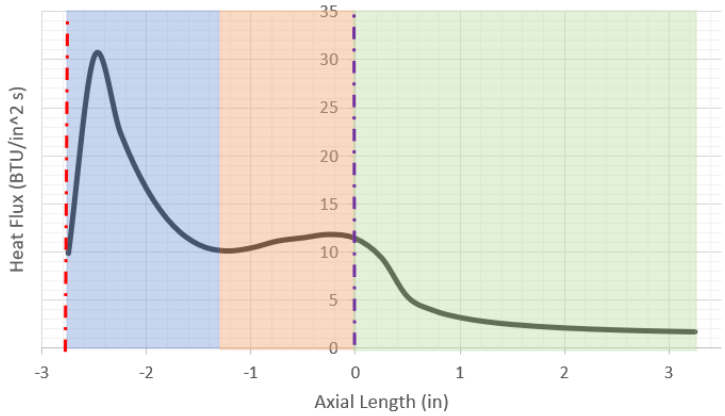

Figure 22. Illustration of heat flux sections in an annular RDRE.

1. Critical section – blue region in which highest heat release is observed due to residence of wave activity.
2. Throat contraction section – orange region in which a geometric throat is formed from an area contraction and afterburning occurs.
3. Nozzle expansion section – green region where combustion products are expanded to supersonic velocity from a sonic criterion at the geometric throat.

The red dashed line represents the injector face while the purple dashed line represents the geometric throat. It was found under this work that these three sections have different scaling requirements and are dependent on the average chamber pressure, gap width, and injection system. However, this figure has been scaled to an arbitrary mean chamber pressure and is not representative of any true measured heat flux profile. Those data are reported in an appropriate journal for CUI//SP-EXPT//CTI information. The reader should not use the scaled data above as specific regions are out of proportion to what was truly measured.

4 EXPERIMENTAL DATA – HYDROGEN TEST PHASE

Hardware remaining from the methane test phase included a single inner body with a slight CR of 1.13 using a straight outer body. It also included the straight outer body and truncated inner body which would have formed a CR of 1.5 with the same inner body. It was known soon after the methane test phase that the coolant channel geometry for the inner body was not ideal for CR > 1.3 in methane/oxygen. Subsequent thermal analysis suggested that this geometry was on the border of burnout if hydrogen/oxygen was used. A single hot fire was conducted in a dual regenerative configuration with the remaining hardware using a throttled bypass sequence. Flow rate was modulated into the combustor via primary venturis and bypass leg venturis enabling a lower pressure and high pressure set point. All throttle points targeted a mixture ratio close to stoichiometric. Approximately 23 seconds into the test, at the end of the high throttle point, the inner body experienced a burn through at the 12 O'clock position at the geometric throat. Time averaged pressure traces at critical interfaces are shown in Figure 23.

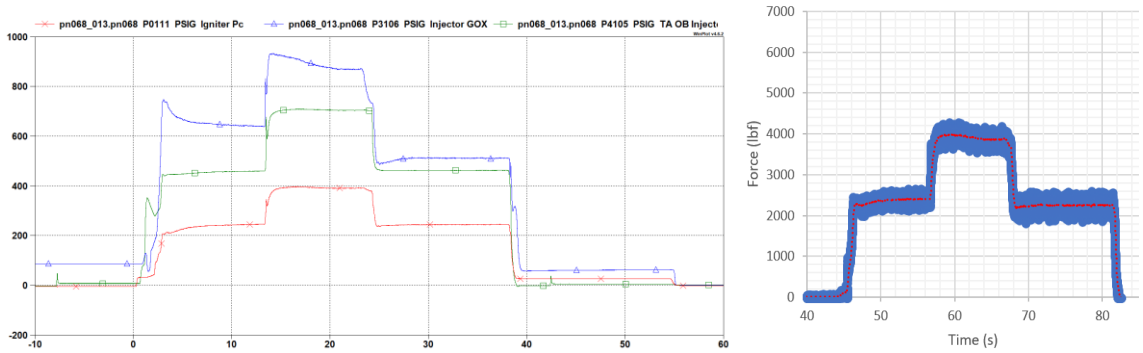

Figure 23. Pressure traces at the injector oxygen manifold (blue triangles), injector fuel manifold (green squares), and chamber pressure (red X). Thrust trace data.

All pressure traces, thrust data, microphone data, and high-speed video all corroborated no wave activity outside of the first ~1 second at low pressure conditions during ignition.

Testing under SWORDFISH Phase 2 was conducted in early April of 2024. The project directly assessed the feasibility of detonation using liquid hydrogen and oxygen in a dual regenerative configuration. Previous gaseous hydrogen testing at NASA showed uncertain detonability and thus a second phase was devised. In addition to the high-speed cameras, microphones were now available to further corroborate what the high-speed videography may or may not have observed. Reduced injection temperatures may also induce wave activity if the cause of the lack of wave activity previously observed was due to deflagration dominating the flow field. The average injection temperature was approximately 100 F during gaseous hydrogen testing in 2022 and -120 F to -90 F at the injector manifold during liquid hydrogen testing. The ignition delay for liquid hydrogen testing would thus be an order of magnitude longer than gaseous hydrogen based on the results of [8].

Given that this test exhibited only deflagrative behavior, the measured Isp and combustion efficiencies are not a surprise. Both performance metrics showed somewhat poor performance overall relative to results obtained during previous NASA work with GH_2/LOx with a smaller annular gap width. Combustion efficiency plotted with Isp efficiency is shown in Figure 24.

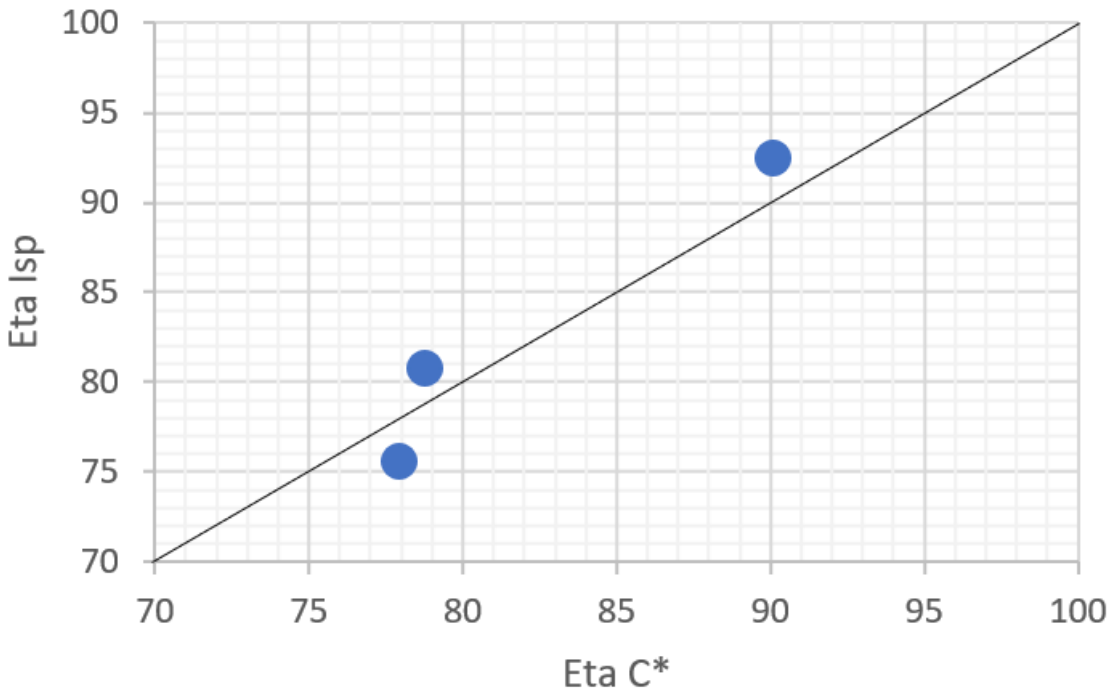

Figure 24. Combustion efficiency as a function of Isp efficiency using head end chamber pressure and with a line of slope = 1.

These data show close correlation and slightly higher performance trends to those presented in Figure 13 using CH_4/Ox. Ultimately, it appears as though a large annular gap width of 0.455 for rocket RDE applications yields poor performance, even for hydrogen/oxygen combustion. However, the nozzle extension on the outer body allows for better capturing of thrust that a plug nozzle alone. Based on performance trends observed, this larger gap width may be non-ideal for any propellant combination and further work is needed to understand the relationship between performance parameters and annular geometry.

Only a single hot fire was conducted with the CR = 1.13 full length nozzle configuration where the inner body experienced a burn through at the geometric throat. This occurred approximately 23 seconds into the test at the end of the high-power set point. Regardless of the reduced injection temperatures, no wave activity was observed other than for a brief moment at ignition.

5 EXPERIMENTAL DATA – KEROSENE TEST PHASE

5.1 CHAMBER, INJECTOR, AND IGNITER HARDWARE

All chamber and injector hardware were produced using L-PBF GRCop-42 (Cu-4Cr-2Nb) as it has potential to withstand high pressure detonative environments given its high strength at substantial hot wall temperature [9]–[11]. Each individual component was fabricated at a select additive powder bed fusion vendor within the US. Table 4 lists pertinent design features of the annular chamber.

Table 4. Summary of Chamber Geometry

L", Overall length to nozzle exit (in)	9.00
L', length from injector face to throat (in)	4.00
Inner Body Diameter (in)	5.59
Outer Body Diameter (in)	6.25
Annulus Gap Width G_c (in)	0.33
Expansion Ratio, A_e/A_t	6.30
Subsonic Area Ratio, A_{inj}/A_t	1.25

This geometry has been found to be non-ideal for direct liquid injection of RP/liquid Oxygen. In addition, this investigation was an initial step towards evaluating large scale Kerosene RDRE designs. The use of non-heated liquid injection would likely be reserved to an ablative chamber design, but the combination does theoretically provide the highest performance detonation conditions [12]. More practical designs would regeneratively cool hardware with the propellant and inject in a heated or conditioned state. Oxygen rich staged combustion cycles, for example, may require gas injection temperatures up to 1400 F which would dramatically change the detonative response of the combustor.

The coolant channel geometry for the inner body was designed explicitly using previously obtained NASA lessons learned from methane hot fire calorimetry data. However, overcooling with water is a major advantage for experimental work that is uncertain of specific heat flux contours subjected to hardware. Furthermore, the coolant channel geometry was designed specifically to the maximum allowable pressure budget of the facility rather than to meet a specific hot wall temperature.

Each injector was designed using typical element schemes with appropriate pressure losses to combat backflow. Many of the considerations implemented into the injector design were specific to additive manufacturing requirements and targeted obtaining correct discharge coefficients. Printed orifices will not have typical discharge coefficients, and are generally lower than anticipated values, since they include shrinkage and roughness factors incorporated. Details on the injector design specifics will be shared at the upcoming JANNAF conference or by request from ITAR qualified individuals. The primary injector tested utilized a GRCop-42 injector face and bimetallic L-PBF body made of Monel K500. This design was manufactured in partnership with Quadrus Corp. under an existing SBIR phase 2 effort. An image of the injector is shown in Figure 25.

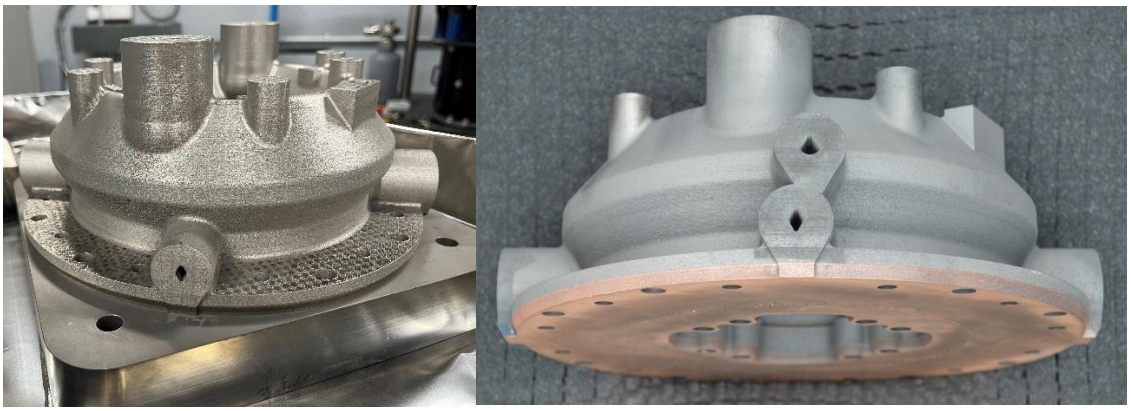

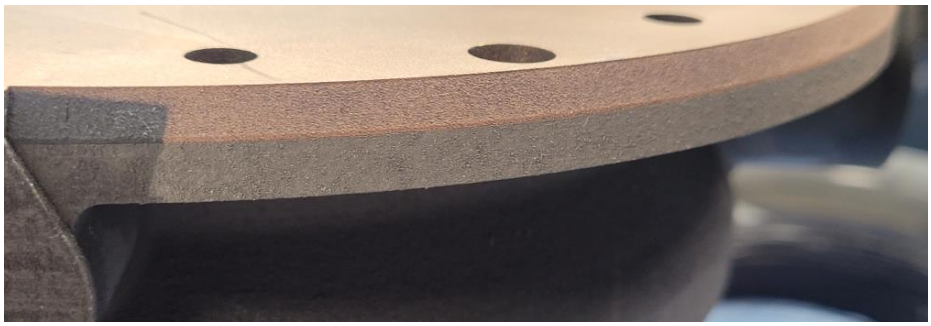

Figure 25. Bimetallic L-PBF (GRCop-42 and Monel K500) RDRE injector.

The specific combination of GRCop-42 and Monel K500 was chosen to enable survival of the injector face in an extreme combustion environment while the injector body would need to survive a high oxygen content environment. The injector survived all tests and operating environments, thus proving out the technology and elevating its TRL from a 2 to a 3. The injector face did not show any indication of heat staining and likely could have utilized a thinner layer of GRCop-42.

An integrated variant of NASAs compact augmented spark impinging (CASI) igniter previously utilized under nearly a dozen other NASA test projects since 2019 [13]–[17] was modified for use with TEA/TEB and nitrogen. Nitrogen was specifically used to aid in the atomization and distribution of TEA/TEB with the CASI igniter manifold to avoid overfilling the manifold with an excess of the pyrophoric fluid.

The propellant utilized in this investigation were liquid kerosene (RP-1) and liquid oxygen for tests 001 and 002. Test 003 utilized a Kerosene alternative fuel whose data will be shared at the upcoming JANNAF conference. Kerosene was injected at ambient conditions (~70 F) while liquid oxygen typically entered the injector manifold at about -250 F/120K on average. A wide range of total mass flow rates were explored yielding a large range of capillary tube attenuated pressures (CTAP) within the annulus specifically at the injector face, geometric throat, and nozzle exit plane. Only 3 hot fires were achieved with several throttle points evaluated within each hot fire. A plot of the mean chamber pressure and mixture ratios explored are shown in Figure 26.

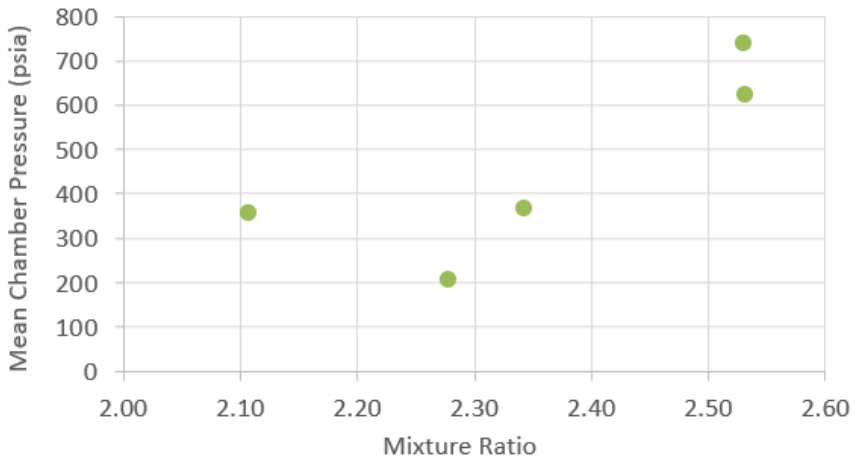

Figure 26. Mean chamber pressure (CTAP) at the injection plane as a function of mixture ratio.

In all cases, only a single detonation wave was observed. Dynamic loads, more specifically vibrations, on the hardware were extreme causing the failure of a machined mating groove on the back side of the inner body thus leaking water into the annulus during test 002. The inner body was then repaired with a weldment of copper alloy rod and re-machined. The third hot

fire burned through several coolant channels on the inner body and ultimately was discovered that weldment had blocked off several coolant channels in posttest evaluation. Regardless, a sufficient range in total mass flow rate and mixture ratio was explored to inform the investigators that only the single wave mode could be achieved with this current design. Subsequent testing would only have caused further damage to the test stand and hardware from the extreme vibrational environments.

5.2 WAVE ACTIVITY AND PERFORMANCE

In all hot fire tests conducted, only a single strong detonation wave was observed. The dynamic vibrations imparted on the thrust structure and hardware were so extreme that multiple torqued fittings backed out, bolts loosened, and instrumentation failed. To illustrate the range in dynamic forces, a plot of the measured thrust as a function of time from test 001 is shown in Figure 27 showing large amounts of noise during the hot fire interval between 60 and 66 seconds. The mean Z axis thrust is also plotted in red.

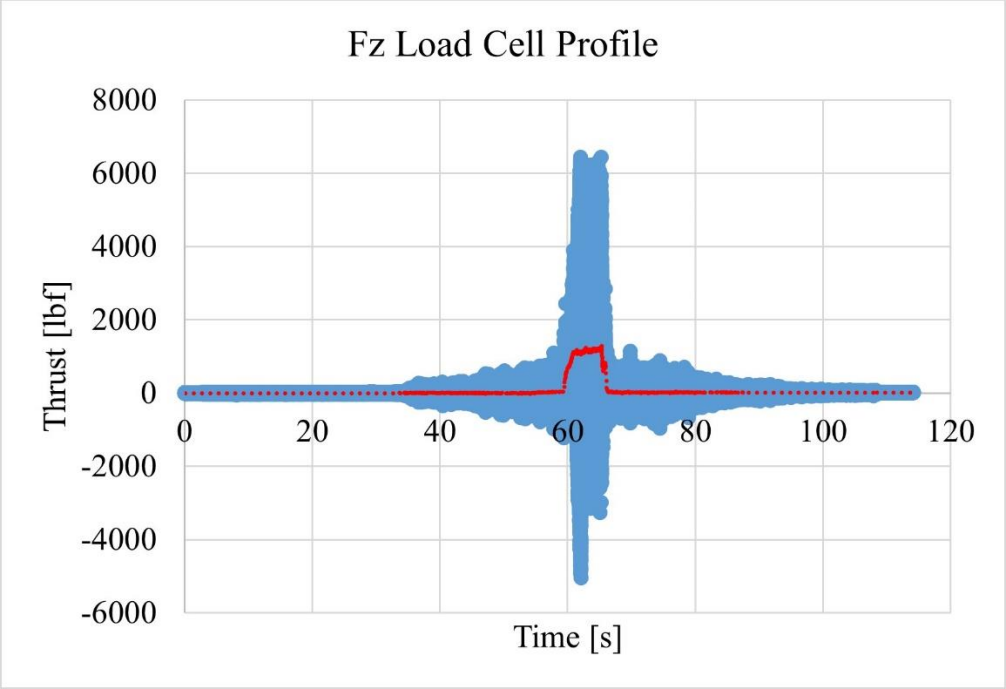

Figure 27. Z-axis thrust measurements capturing dynamic forces imparted on the thrust structure during hot fire from the single wave modes.

Accelerometer data corroborated these measurements with over 1000 G's measured, clipping the measurement capability of the sensor. The min to max force was found to be greater than 11,000 lbf for this test case with tests 002 and 003 clipping the measurement capability of the load cells. Accelerometer data is presented in Figure 28.

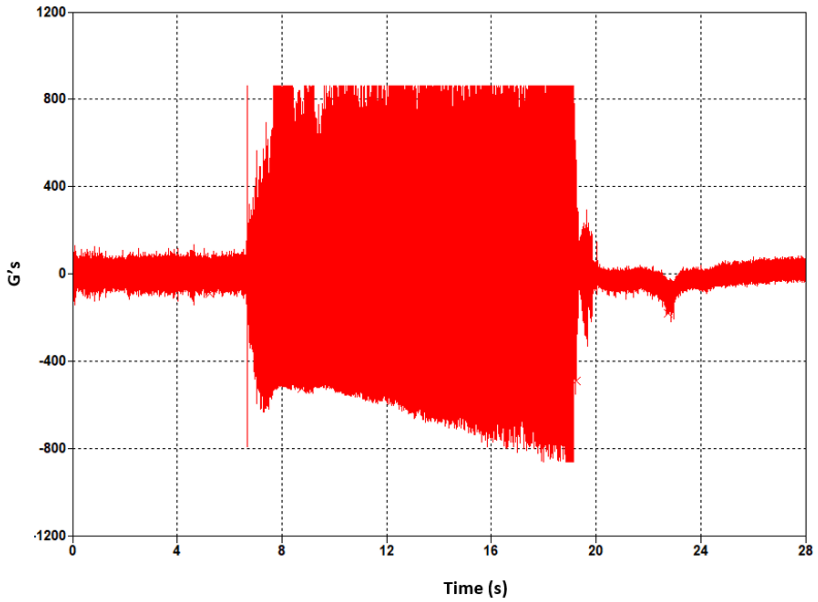

Figure 28. Accelerometer data for test 002 in the Z axis of thrust, G Force as a function of time (seconds).

These data show clipping of the accelerometer's measurement capability at about 850 G's with the bulk of forces measured in the Z axis. An image of the clockwise rotating detonation from test 002 is shown in Figure 29.

Figure 29. Test 002 clockwise rotating detonation image from high-speed video.

Because the thrust class of this test article is in the 1000-10,000 lbf range, the high-speed camera had to be offset from the centerline of thrust. Thus, only a portion of the annulus could be observed in each test without irreparable damage to the high-speed camera.

Wave speeds were found to increase with increasing total mass flow rate. This behavior has been observed previously in open data sets and other NASA hardware. The highest wave speed found in test 002 was measured to be just under 4200 ft/s at a mean chamber pressure of

about 360 psia. In all test cases, with the exception of test 001, the wave direction was clockwise. The wave direction did not appear to impact heat flux profile or other performance metrics.

Two high frequency microphones were used to capture the acoustic environments exterior to the test article. They were mounted approximately 3 feet off to the side of the combustor. The measured sound pressure level was found to exceed about 175 dB at the peak with a root mean square (RMS) value as high as 170 dB at ignition. The power spectral density showed two major peaks at 2.15K Hz and 6.43 K Hz. The former matched the rotating frequency of the single wave mode confirmed via high-speed videography. The latter is likely the second harmonic resonating with the thrust structure as no underlying was activity outside of the primary single wave mode was observed in the high speed data. These data are shown in Figure 30.

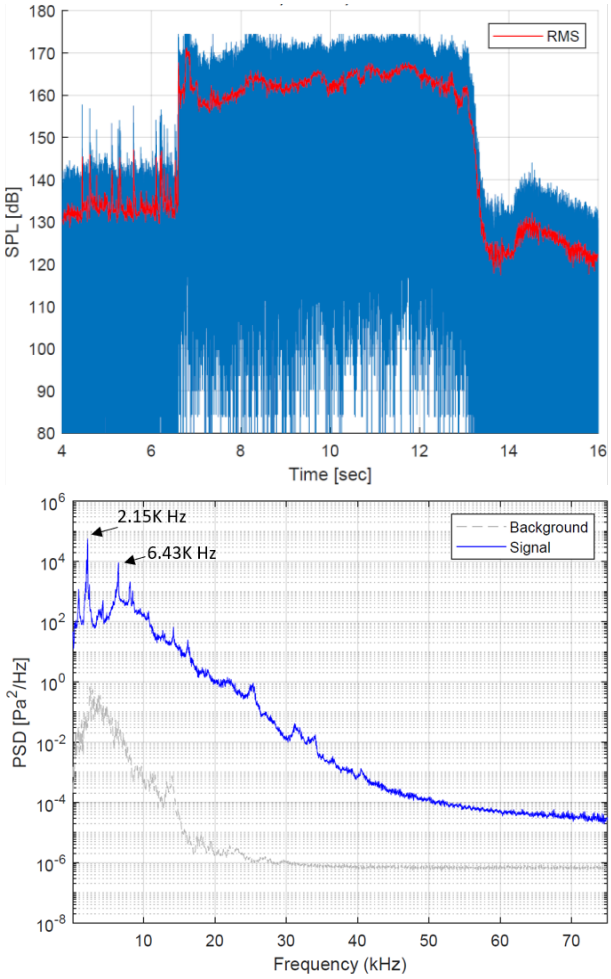

Figure 30. Sound pressure level and power spectral density plots for test 001.

5.3 WALL SOOT AND TEA-ASH OBSERVATIONS

Heavy wall soot and TEA-ash buildup was observed on the hot wall post tests 001 and 002. Heavy soot formation within the plume was observed and is characterized by the typical bright yellow exhaust with some green hues from burned TEA/TEB. TEA-ash is characterized by white buildup on the hot wall. Images of the test articles post hot fire are shown in Figure 31.

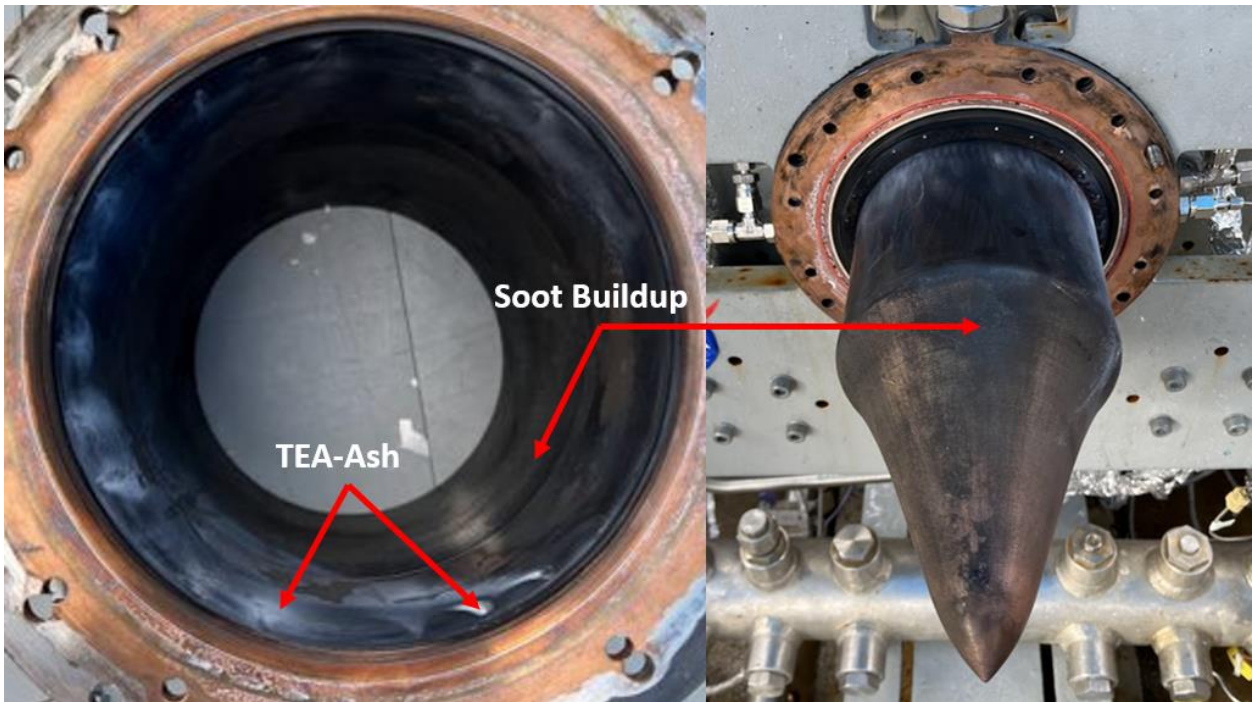

Figure 31. Post test 002 images of the outer body and inner body hot walls with substantial soot and TEA-ash buildup.

Previous hot fire testing of combustion device hardware has shown the buildup of soot and TEA-ash can reduce overall wall heat loads by anywhere from 10-40% depending on the severity [4]. The buildup on the hot wall of these hardware suggests a 25% reduction based solely on hot fire test experience of the test requesting engineers. Under the previously mentioned CIF work with Purdue University, the hardware geometry and injection conditions tested enabled multi-mode operation with very little wall soot buildup. Images of these hardware post several dozen tests are shown in Figure 32.

Figure 32. Purdue/NASA CIF hardware post dozens of hot fire tests courtesy of Dr. Ariana Martinez from [18]**.**

A stark difference in plume coloration was observed between these two test articles. A lack of soot formation was observed with the CIF hardware yielding a purple/blue plume. Images comparing these hardware hot fires are shown in Figure 33.

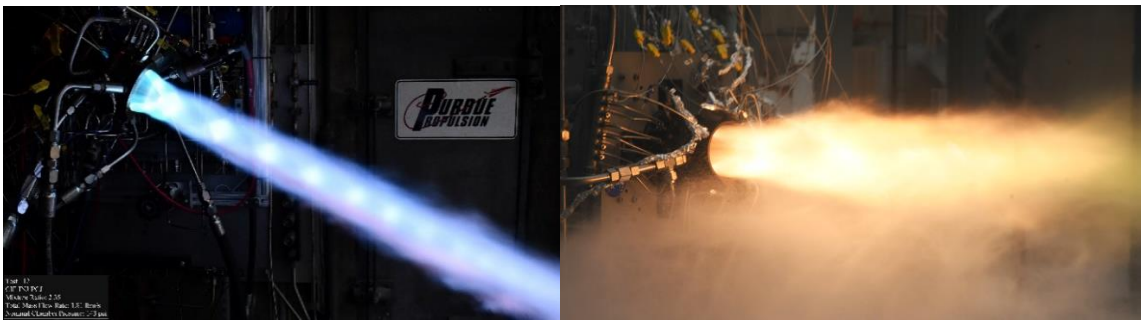

Figure 33. Purdue/NASA CIF hardware [18] **(left) and NASA ECI hardware (right) during hot fire.**

Ultimately, soot formation may be considered an indication of lower efficiency combustion while a lack of soot in the plume may indicate reduced combustion time scales inhibiting soot formation. Further investigation is needed to better understand this phenomenon. Both test articles likely represent the extreme ends of the design space where an ideally performing Kerosene RDRE may exist.

5.4 HEAT TRANSFER MEASUREMENTS

The heat transfer to the walls of the inner and outer bodies was obtained by calculating the change in enthalpy to the coolant and multiplying by the total mass flow rate of coolant. In most cases below, these data are presented as a function of measured injection plane pressure. In the majority of cases, the severity of vibrations from the detonation wave caused significant error in the measurement of coolant inlet and exit temperature and pressure. Only once the combustor was shutdown were the measurements able to reestablish meaningful values and yield reliable data. All data presented in this section were obtained in this fashion prior to the coolant temperature reducing in the ramp down of coolant mass flow rate at the end of each test. Figure 34 and Figure 35 show the measured total heat load and mean heat flux, respectively, to the coolant as a function of the measured injection plane pressure.

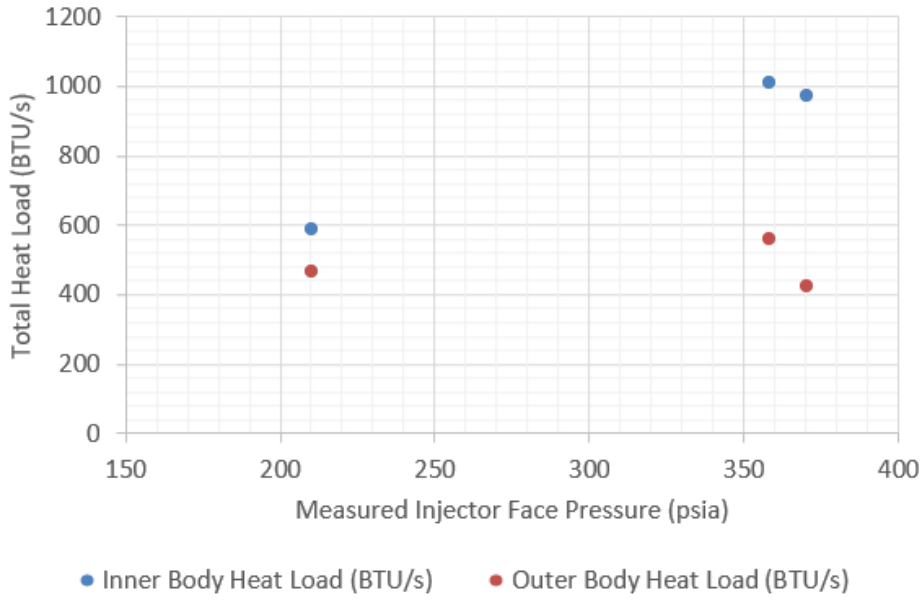

Figure 34. Total heat load to the inner body and outer body as a function of measured injection plane pressure.

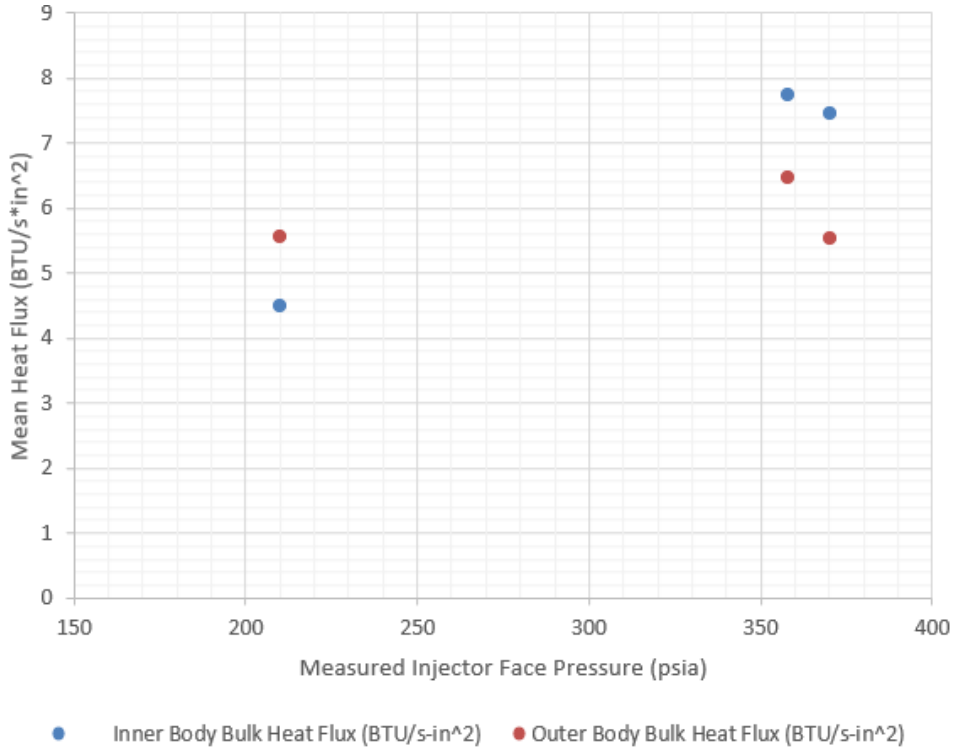

Figure 35. Mean wall heat flux to the inner body and outer body as a function of measured injection plane pressure.

The inner body included the heat addition to the plug nozzle however, it is estimated that this proportion of heat addition likely contributes less than 8% of the total heat input, even though surface area is approximately 35% of the component. This is entirely due to low on average heat flux in the expansion section of the nozzle relative to the annulus. In addition, the influence of

leaking water into the annulus during hot fires 002 and 003 likely are introducing error in the quantities presented. However, it is unknown what this error may be. The measurements from the calorimetry outer body and nozzle extension captured usable trends in the heat flux shown in Figure 36.

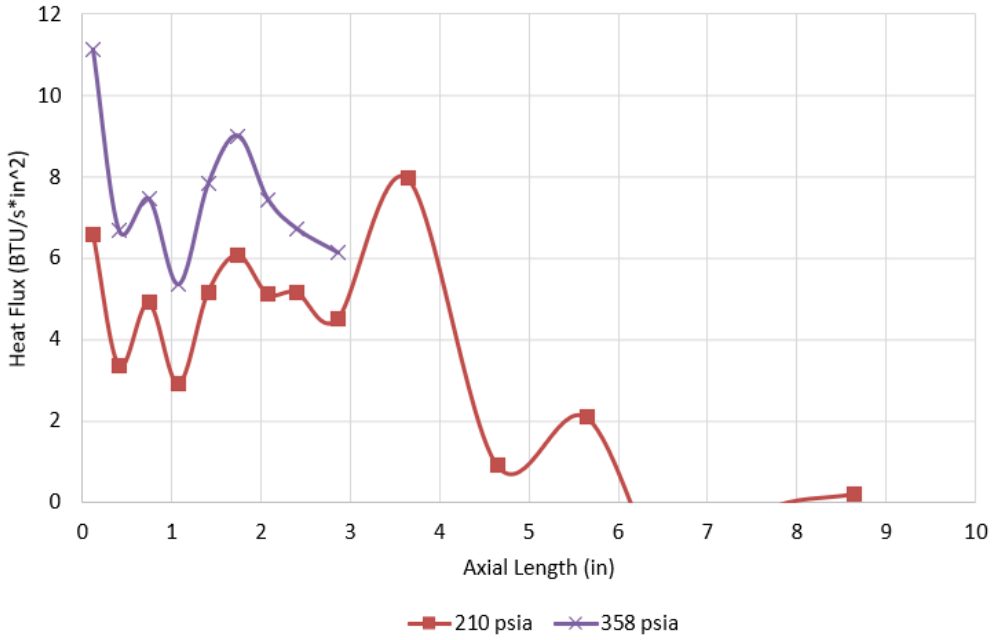

Figure 36. Heat flux profile as a function of axial length for varying injection plane pressures.

These data show a large jump in the heat flux at the injection plane where the detonation wave resides, followed by a plateau and an abrupt rise where the throat area contraction is, located at +4 inches. Note that the thermocouples from X = 3” and further for test 002 did not yield data of value. Those thermocouple data were not recoverable. Generally, this profile resembles what was expected and looks like other experimental data sets in the open and closed experimental literature. However, attempts at scaling these data at each axial location does not match the more reliable data sets NASA currently has. This was also expected given that hardware leaks, dynamic vibrations from the detonation, and uneven wall soot and TEA-ash buildup are likely imparting substantial error. The wall heat fluxes presented are much lower compared with data presented by [18] with NASA/Purdue CIF RP/GOx hardware and substantially lower than high performing methane/oxygen NASA hardware. Regardless, these data further illustrate the needs for corroborating data from the pressure gain combustion community.

To further evaluate these data, direct comparison to constant pressure theory throat level heat fluxes was conducted. The throat level heat flux was computed using Bartz heat flux correlation assuming frozen chemistry [19]. It is well known that Bartz throat level heat flux dramatically overpredicts the true heat flux a constant pressure rocket experiences. This is particularly the case for Kerosene engines. In addition, the soot buildup on the walls of the test article likely insulated and reduced the measured heat flux further. The computed Bartz throat level heat flux as a function of mean chamber pressure is shown in Figure 37. In addition, the ratio was taken between the measured injection plane and throat heat fluxes to the computed Bartz throat heat flux also shown in Figure 37.

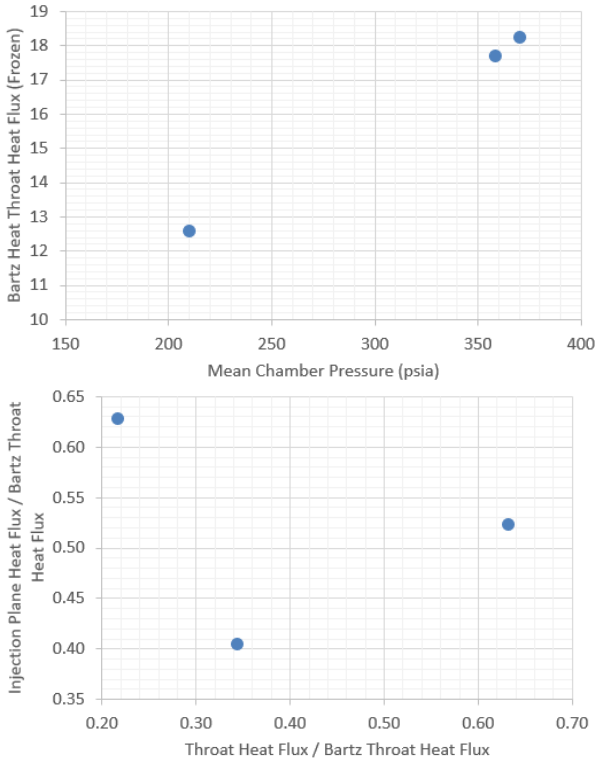

Figure 37. Bartz predicted throat level heat flux (frozen chemistry) as a function of mean chamber pressure (left) and ratio of the injection plane heat flux to Bartz throat heat flux as a function of the measured throat heat flux to Bartz throat heat flux.

The ratio of measured to predicted throat heat flux is also plotted as a function of mean chamber pressure in Figure 38.

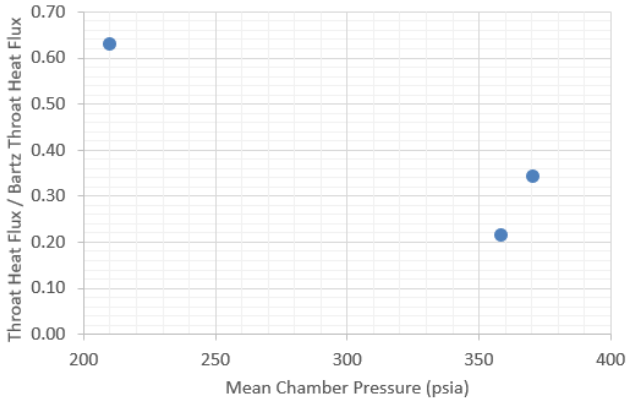

Figure 38. Ratio of measured throat heat flux to Bartz throat heat flux as a function of mean chamber pressure.

This analysis and data is limited but some inferences can be made. It appears that the throat heat flux widely varies while the injection plane heat flux where the detonation resides appears to average around 50%. From other data sets, it is known that the injection plane heat

flux is at least an order of magnitude higher for high performing methane RDREs. In addition, the throat heat flux ratio has been observed to be more than double the predicted value. With that said, this configuration is likely just a low performing RDRE relative to other designs tested. It is known how to improve this design going forward to achieve markedly higher performance, details of which will be shared at upcoming JANNAF conferences.

5.5 COMBUSTION AND SPECIFIC IMPULSE MEASUREMENTS

Of the more reliable data considered, the overall combustion efficiency and Isp efficiency were found to be high for a Kerosene combustor. Most public information on Kerosene constant pressure rockets show that the best C* and Isp efficiencies are 96% and 92%, respectively. The RD-180 operating close to 4000 psia, yields an Isp efficiency of about 96.6% assuming frozen chemistry, and 91.5% assuming equilibrium chemistry. Though likely there are better performing devices in the closed literature. The data obtained from this hardware yielded the highest Isp efficiency of 95% and combustion efficiency of 86% assuming equilibrium chemistry. And it is already known that this hardware is low performing relative to other data sets NASA currently has. For a constant pressure kerosene engine, it is typical to obtain Isp and combustion efficiencies near 80% in the first hot fire attempt. Subsequent design revisions often yield better performance in excess of 90% (frozen chemistry). Figure 39 shows the trend in Isp efficiency as a function of combustion efficiency and suggests a mismatch in the measured quantities from what is expected. Further evaluation of these data are needed to understand the complex interplay between the pressure environment and force generated from an unsteady combustion device such as an RDRE.

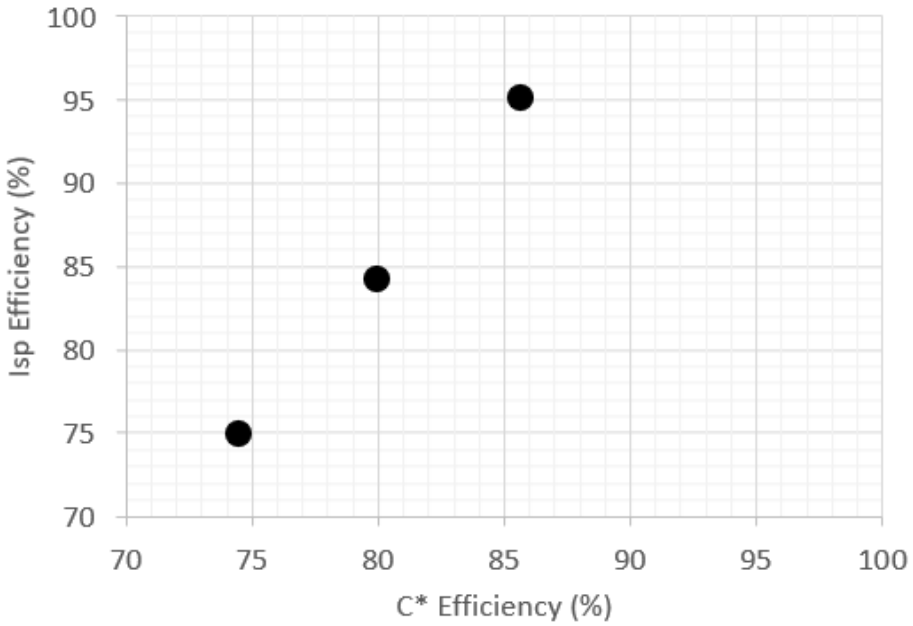

Figure 39. Isp efficiency as a function of combustion efficiency for several RDRE hot fires.

The highest measured thrust achieved in this test project was about 5300 lbf at a mean chamber pressure of about 740 psia and an Isp of 246 seconds.

Finally, the ratio of the nozzle exit pressure and the throat total pressure were taken with the ideal calculated quantities. It is expected that a constant pressure rocket may yield values that are slightly less than 1 due to cumulative losses. However, the RDRE measured values similar to or greater than the ideal calculated values shown in Figure 40.

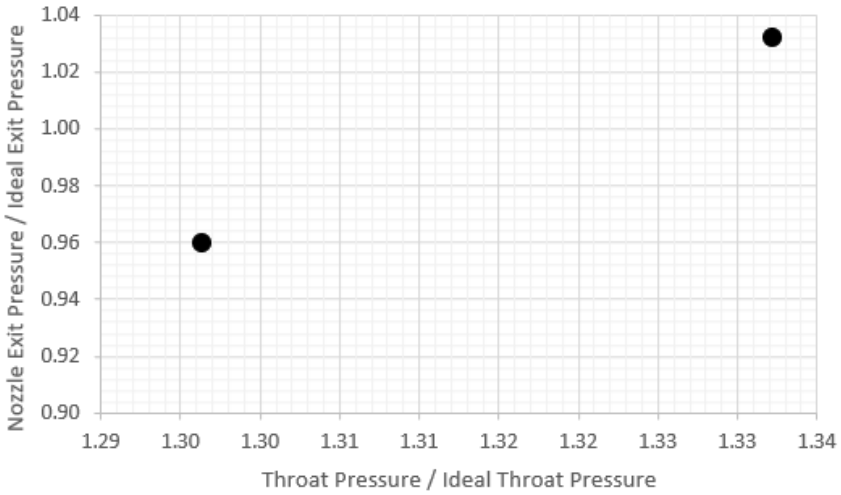

Figure 40. Ratio of the measured nozzle exit pressure and throat total pressure to the ideal calculated quantities.

These measurements are not in isolation as direct measurements on different scale RDREs have also been measured with similar results. While it is not clear what this means as of yet, it is expected that an inherently unsteady combustor may yield elevated total pressures since heat release is expected to be higher than a constant pressure rocket.

6 EXPERIMENTAL RESULTS - SUBSCALE CALORIMETRY

All hot fire test results are presented as a function of axial length and are primarily reported as a function of the measured mean chamber pressure at the injection plane. This has been found to be the most comparable across different combustor scales and geometries. Direct calorimetry measurements were made using a calorimeter outer body. The inner body was a monolithic piece with axial running coolant channels, and thus only a total heat load or bulk heat flux was obtained. In addition, several plots are presented as a scatter plot with smooth lines connecting data points. While this is likely incorrect for interpolating between points, the data are presented this way to give the reader a sense of variability between test cases and to delineate between each test more easily. Several tables are given with pertinent data for the reader to utilize outside of this work. All hardware was water cooled with mass flow rates validated using characterized cavitating venturis and orifices for back pressure.

6.1 MARLEN SUBSCALE CALORIMETER TESTING

Gaseous methane and oxygen at ambient temperatures averaging 80 F were used in conjunction with several configurations of AM GRCop-42 RDRE outer body, inner body, and injector. In addition, a single AM GRX-810 injector was also tested. The average chamber pressure measured at the injection plane was 228 psia with the maximum pressure of 522 psia and minimum pressure of 55 psia. All hardware was water cooled with typical mixture ratios of about 3.5, though a range in mixture ratios from 2.55 to 4.0 were also explored. Several varying geometries of hardware were evaluated. These included.

1. Annulus contraction ratios of 1, 1.25, and 1.5 achieved by tapering the inner body towards the outer body making a minimum area restriction some distance, L', from the injection plane. A contraction ratio is defined as the ratio of the annulus injection plane area to the geometric throat area.
2. Annulus length or L' values of 1, 1.5, 2, 2.5, and 3 inches. This is the distance from the injection plane to the geometric throat or beginning of the expansion section of the nozzle in the case of contraction ratios of 1.

3. Injection- element scheme and element density. Three injectors were evaluated: a 54-element triplet, a 108-element triplet, and a 54-element trio. The all injectors were oxygen centered with injection half angles of 30 degrees. The impingement distance from the face was approximately 0.075 inches, though with additive manufacturing limitations this was likely the closest possible impingement distance achievable with powder bed fusion.

Figure 41 shows a CAD crossectional of the calorimeter chamber, an image of the test cell with test article installed, and an example image of a typical hot fire.

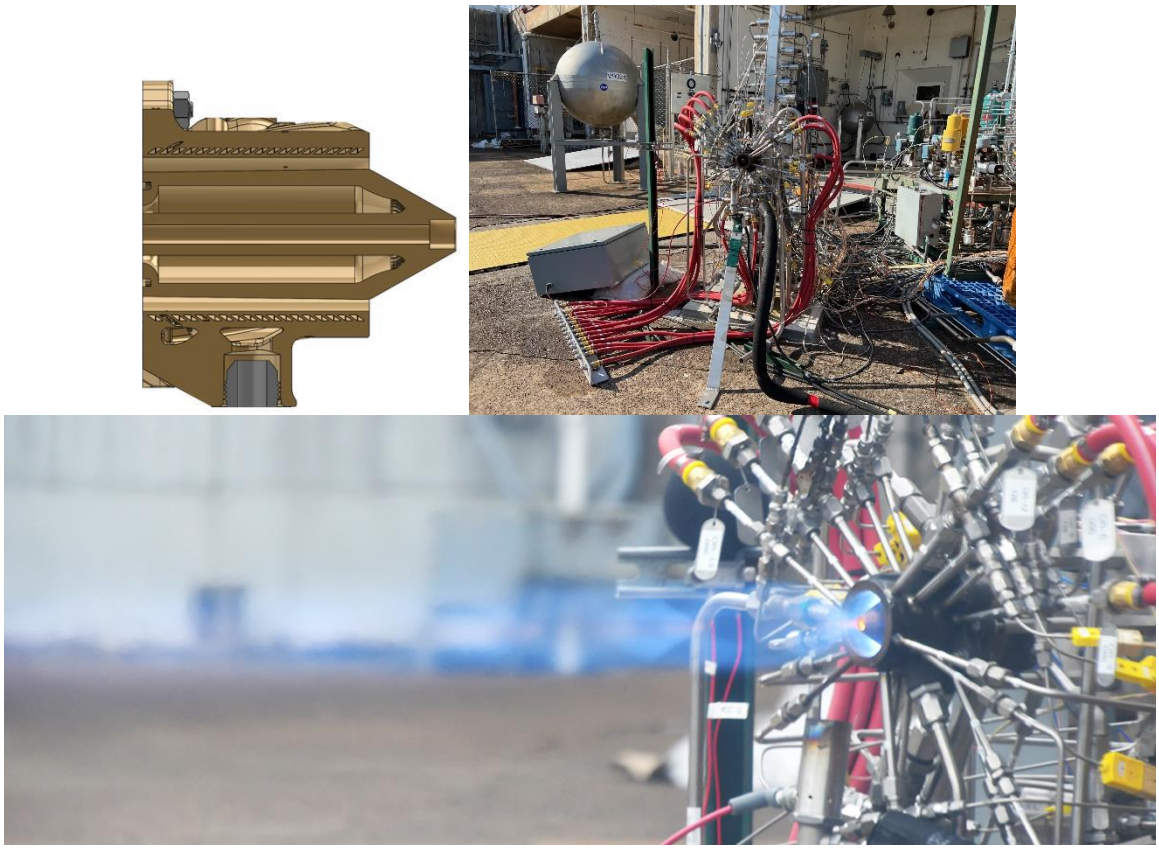

Figure 41. Computer aided design cross section of the calorimeter chamber (top left), test cell with test article installed (top right), and typical hot fire image (bottom).

As mentioned, much of the hardware was developed using typical AM processes and alloys. Images of the primary injectors and inner bodies are shown in Figure 42.

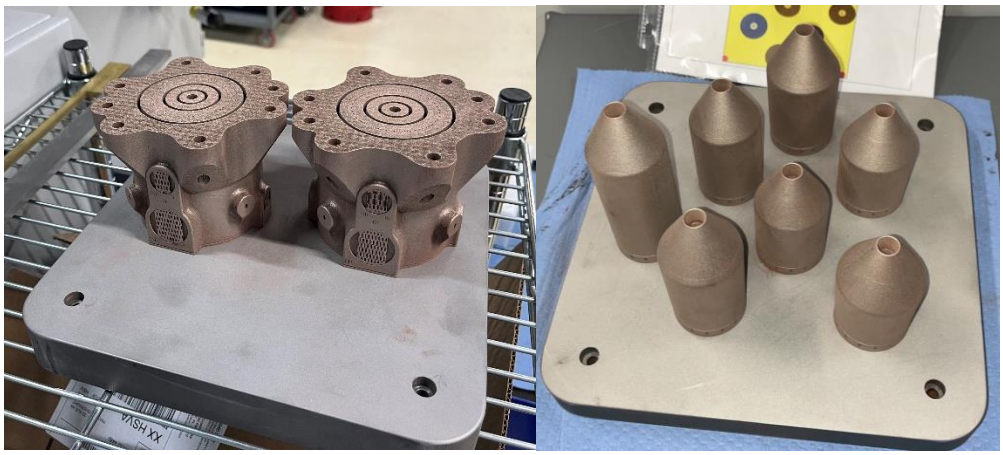

Figure 42. MARLEN RDRE injectors (left) and inner bodies (right) on the build plate post depowdering.

During the original design process, consideration was given to how much “dead space” was available on each injector face. It is now well known that the dead space allows for parasitic deflagration to occur and limit the performance of the RDRE. Though it is expected that some amount of deflagration may be desirable but is unknown what proportion may be ideal. The mixedness of the incoming propellants has also been found to be a critical parameter, though is hard to define quantitatively. The test conditions explored under this investigation are shown in Figure 43 by plotting the measured injection plane pressure with the test mixture ratio.

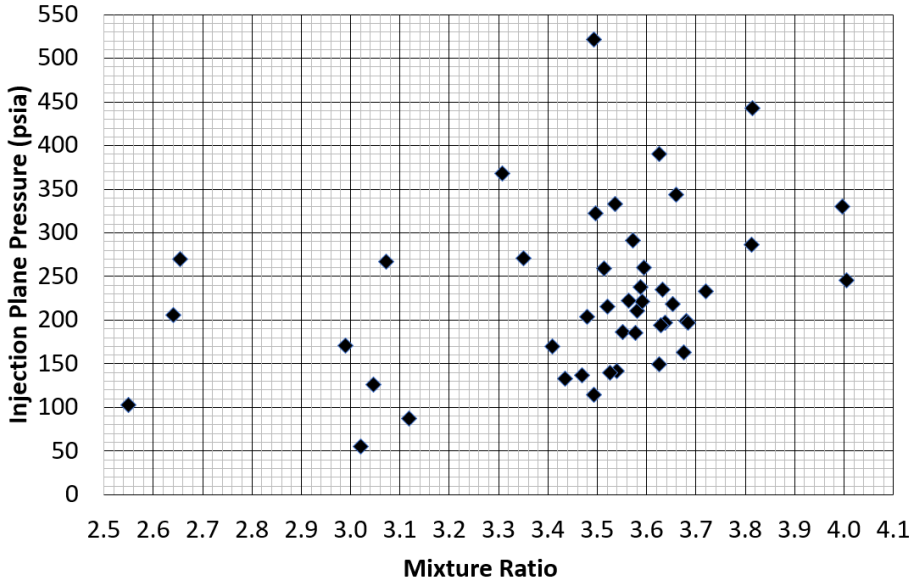

Figure 43. Measured injection plane pressure with test mixture ratio.

6.2 INFLUENCE OF WALL TOTAL HEAT LOAD ON HOT WALL SURFACES

The data presented in the previous sections give several major findings. The addition of a contraction does not impact the wall heat flux profile. In other words, as wall crossectional area changes between hardware configurations, the wall heat flux does not change as long as mean chamber pressure remains the same. Figure 44 shows that for the same annulus L' at differing contraction ratios, both the outer body and inner body trend similarly to each other with no significant variation about the mean. This indicates that the hot wall geometry or annulus cross section does not influence the wall heat flux other than by modification to the mean chamber pressure.

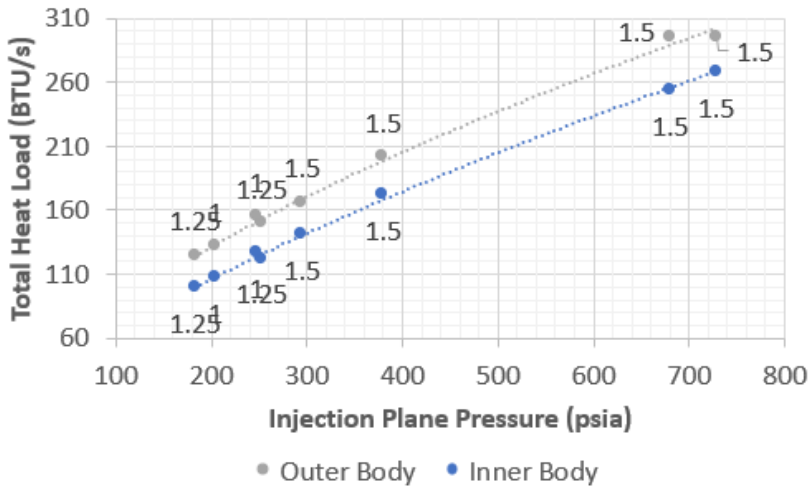

Figure 44. Total heat load trends for both outer body and inner body data at constant length for MARLEN hardware with varying contraction ratio.

Another trend apparent in Figure 44 is that for a configuration where both the outer and inner body lengths match at the throat (no additional nozzle length on the outer body for higher heat addition) the outer body consistently shows higher overall heat flux. This may be partly caused by lower average heat pickup on the plug nozzle due to expanding combustion products. However, the margin by which all configurations tested differ is greater than this if the surface area of the plug were subtracted out and assumed to have zero heat input to the inner bodies.

These data show consistently that the outer body yields higher bulk average wall heat flux when compared to its inner body counterpart. More interesting still is that two nearly identical injectors were tested and found to have about the same wall heat flux in both the inner and outer bodies. These two injectors were designed to have a stiffness ratio of 1 and 1.3 at a mixture ratio of 3.0. Meaning that the ratio of the fuel side pressure drop to the oxygen side pressure drop at constant mixture ratio were about 30% different. This did not appear to have any meaningful impact on wall heat flux. Lastly, It is unknown if the inner body wall sees a different heat flux profile altogether, however based on test data from the NASA ACO test series it is likely that the inner body does see a different profile.

6.3 DIRECT COMPARISON WITH CONSTANT PRESSURE DEVICES

Several investigations on hot wall surface finish have evaluated the total heat load and bulk heat flux to the hot wall of constant pressure combustion chambers. Much of which has found that roughened walls yield far higher wall heat loads compared to polished hot walls. This section compares the RDRE bulk wall heat flux with NASAs state-of-the-art methane/oxygen combustion chamber dubbed WHALE shown in Figure 45.

Figure 45. NASA SOA methane/oxygen constant pressure combustion chamber dubbed WHALE.

This thrust chamber assembly was initially developed to investigate novel coolant channel geometries for increased heat pickup in expander cycles, or wall heating for additive lander engines (WHALE). In addition to ultra low-pressure losses in the coolant channels, heat pickup was found to be substantially higher compared to traditionally manufactured chambers with polished walls. The combustor successfully survived all testing and was utilized as a benchmark for direct comparison with RDRE performances.

6.4 NEED FOR FURTHER DATA

Several gaps are still prominent in the knowledge base for predicting wall heat flux in RDREs. This data set goes a long way towards understanding and modeling this novel combustion environment, but further efforts are needed to better understand how detonation environments change the wall temperature and how the combustor annulus and wall profile are designed. Several of these gaps include:

1. Need for data at different gap widths in the detonation region.
2. Need for data with different element schemes.
3. Need for computational modeling work to better understand critical trends and specific features observed in those trends in heat flux.
4. Need for data with different propellants and coolants.

7 EXPERIMENTAL RESULTS – GENERAL WAVE BASED OBSERVATIONS

The following sections describe in detail the results that were discovered through analysis of the collected data from the NASA MSFC test projects. These sections include discussions on wave activity scaling, microphone diagnostics, torque measurements, hydrogen and methane comparisons, single wave modes, subscale testing observations, and contraction ratio-wave speed relationships.

7.1 SCALE OBSERVATIONS OF WAVE ACTIVITY

To date, multiple scales of RDRE have been evaluated through hot-fire testing at NASA MSFC. A 500 lbf 2-inch, a 5,000 lbf 6.25-inch, and a 10,000 lbf 6.25-inch geometry. Each of these

configurations have different gap widths ranging from 0.2 inches to 0.455 inches and contraction ratios from 1 to 1.7. Several general trends have been observed with these experimental data. Wave activity appears to be strongly correlated to hardware geometry parameters including, but not limited to, injector element density, gap width, and mean circumference.

Bykovskii's 2017 [20] paper essentially established that if the annulus circumference were increased, the wave spacing would remain constant with all else held the same. This means that the total number of waves at any given time will increase proportionally with an increase in combustor circumference. Thus, normalization of design parameters with the mean annulus circumference should yield meaningful trends across multiple combustor scales. One such valuable parameter is the wave spacing, which is simply the mean annulus circumference divided by the number of waves. Parameters such as gap width, injector element density, and combustor frequency all show what appear to be meaningful trends as well.

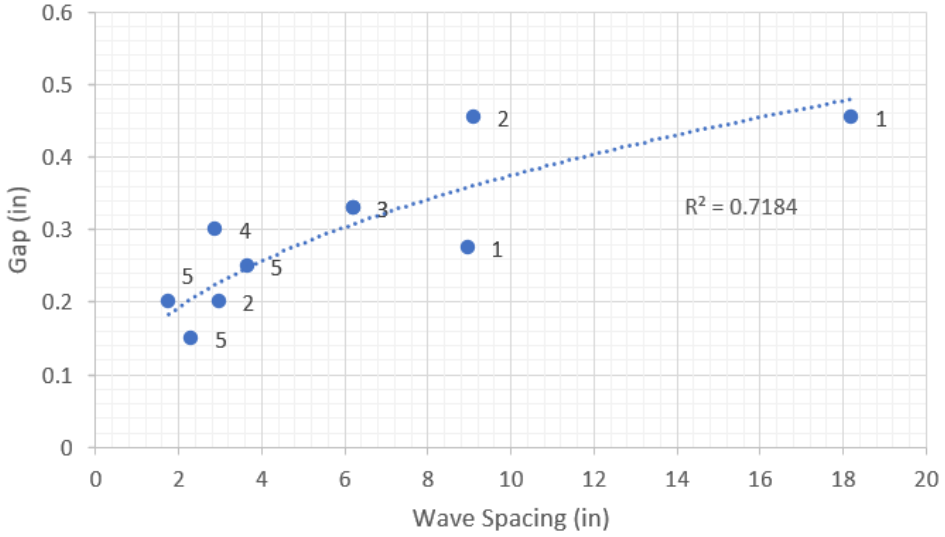

Figure 46. Annular gap width as a function of wave spacing.

Figure 46 shows the annulus gap width as a function of wave spacing for both NASA hardware and data from the experimental literature. The data are labeled with the number of waves observed during that specific test. The R^2 value indicates that 71% of the trend in wave spacing can be explained by the gap width. While not a perfect trend, it does give a good start for the design space of an annular RDRE. This makes sense given that, in most test data to date, the combustor appears to couple with the 1, 2, 3, … n -T modes of the annulus. In addition, the injector is typically hard choked, likely isolating the wave activity to within the annulus itself. However, it should also be mentioned that coupling with the injection system design has been partially observed, meaning this should not be completely ruled out. Other parameters such as mass flux and injection temperature as reported in Martinez et al. [21] are also important parameters that need to be considered.

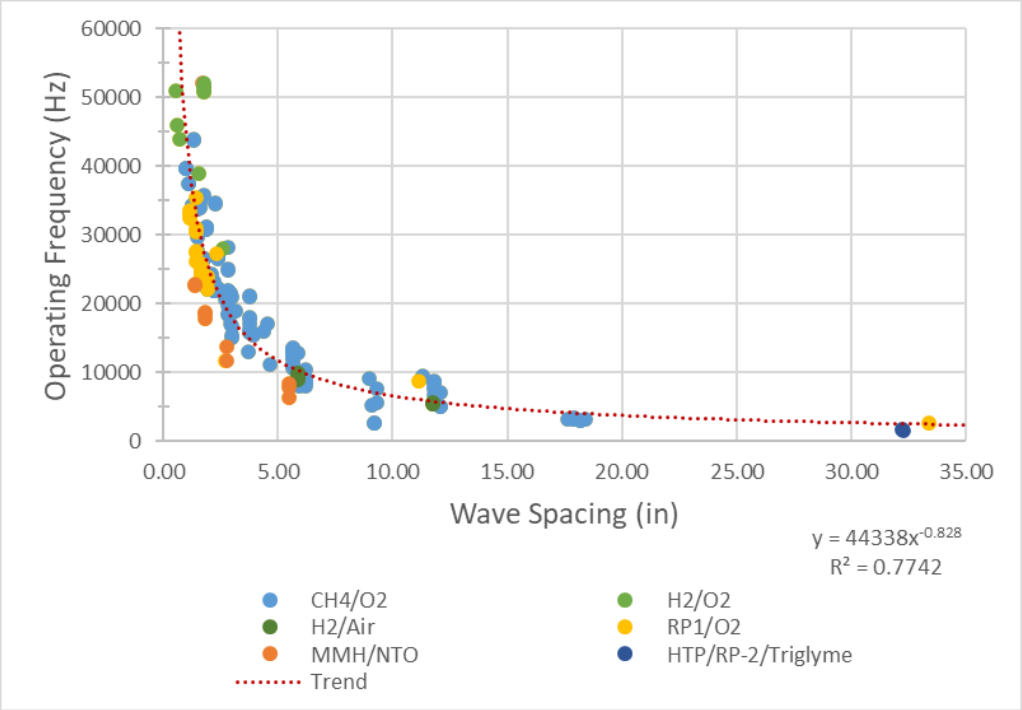

Figure 47. Wave frequency as a function of wave spacing for various propellant combinations.

A major finding from the literature review was a trend in the measured fundamental frequency of various RDRE configurations as it relates to wave spacing. This is somewhat intuitive since wave spacing is analogous to wavelength and frequency is a function of wavelength. Nonetheless, all the experimental data available, regardless of the propellant type, closely aligned to a single trend as seen above in Figure 47. The trend tends to be more consolidated when comparing different propellants with higher R^2 values. In general, these data are seen to shift higher in frequency with increasing injection temperature, increasing reactivity of propellant, higher total mass flux, and with smaller annulus gap widths. These data will be further investigated and results of which presented in later works.

7.2 MICROPHONE DIAGNOSTICS

Microphone diagnostics were implemented to collect free-field acoustic data during RDRE operation for both the SWORDFISH and MARLEN test campaigns. Since RDREs produce a signature “whistle” sound, like that of high-frequency combustion instabilities in deflagration-based rocket hardware, microphones were sought as an additional tool to corroborate high-speed video data. Microphone data was analyzed via Fast Fourier Transform (FFT) and Power Spectral Density (PSD) plots to extrapolate and pinpoint frequency peaks. Using combustor dimensions and number of waves from high-speed video, the recorded sound frequency was also used as a method to assess detonation wave speed. Furthermore, microphone data was plotted using a spectrogram; a valuable tool for analyzing trends in RDRE fundamental frequencies/harmonics over time. Spectrograms allow for quick, visual interpretation of time-resolved wave activity (including mode shift) and can be plotted alongside chamber pressure, upstream propellant temperature, valve sequences, etc., to interrogate the effects of recorded sensor data on (or resulting from) wave activity.

Tests 1, 6, and 9, and highlights from tests 7 and 12 of the SWORDFISH campaign series are discussed in the figures below. PSD plots for microphone data with accompanying spectrograms and chamber pressure profiles illustrate the dominant frequencies of the wave(s) and how they change over time. For interpretation, PSD units of Pa^2/Hz have been converted into Sound Pressure Level (SPL) in dB using a standard reference pressure of 20 µPa. Microphones were placed about 24" laterally from the test article.

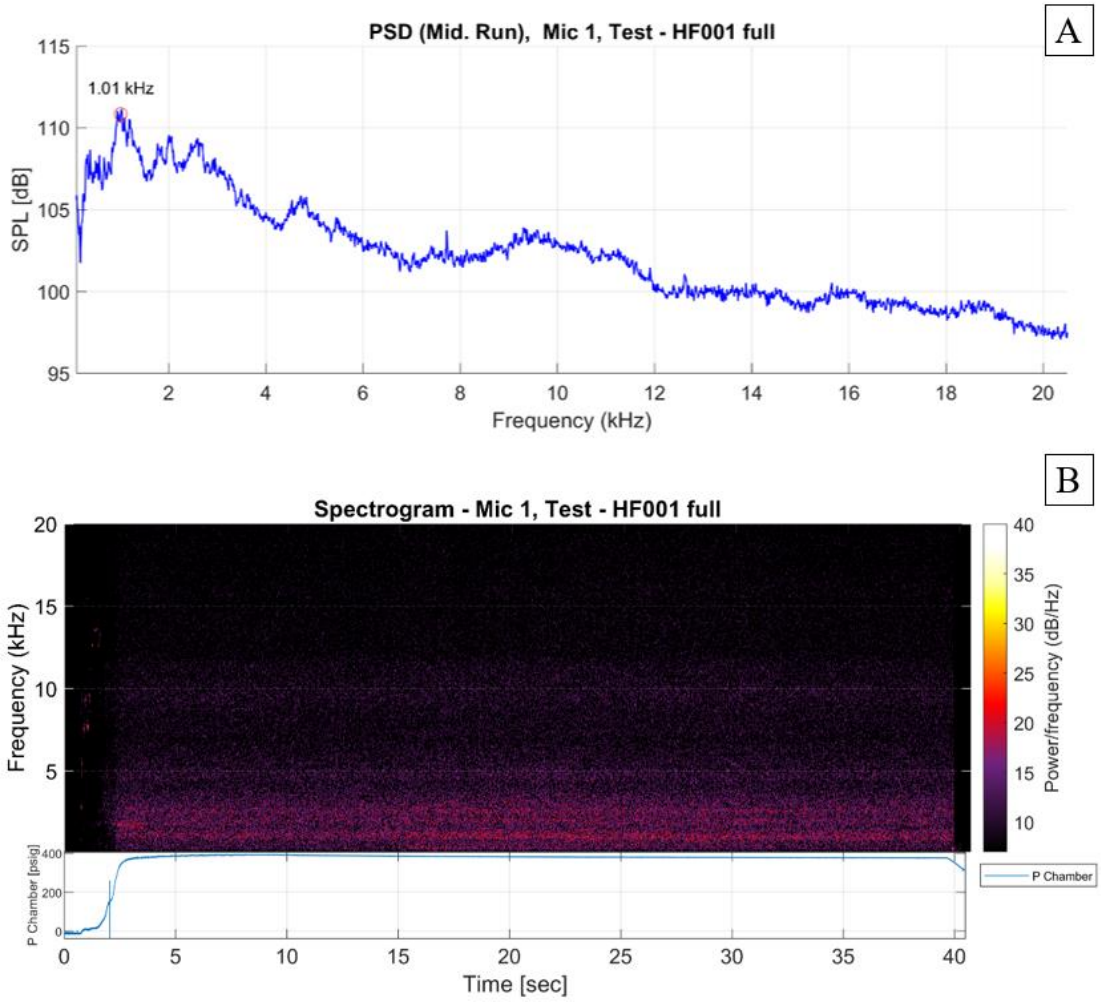

Figure 48. Test 1 PSD (A) and spectrogram (B) – deflagration case.

Test 1 in Figure 48 above shows the deflagration case of the test series. This configuration was the straight annulus with CR of 1. Wave activity was not observed in high-speed video which determined the combustor was operating in a deflagrative mode. Microphone data confirms this, as strong/clear peaks associated with wave activity are not present in the PSD. The spectrogram is primarily recording jet noise for this test.

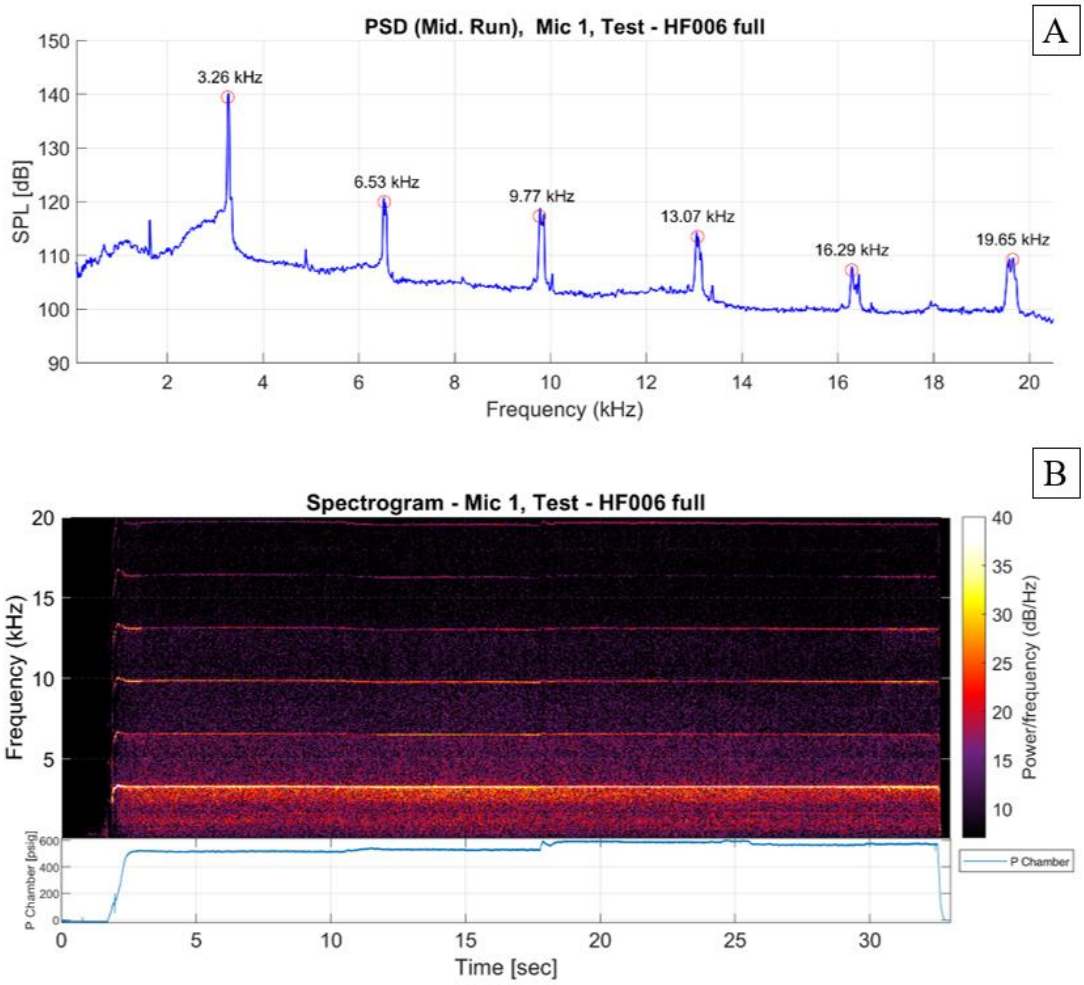

Figure 49. Test 6 PSD (A) and spectrogram (B) – detonation case, 1 wave.

Tests 6 and 9 in Figure 49 above and

Figure 50 below, respectively, show the combustor operating in a detonative mode. Test 6 (CR of 1.3) operates on a single-wave mode and test 9 (CR of 1.13) also operates in a single-wave mode. One hot fire cycle was conducted for test 6 and two consecutive cycles were conducted for test 9. Sharp peaks seen in both the PSD and spectrogram indicate wave activity. The SPL/Hz in these tests are significantly higher than test 1 which operated on a pure deflagrative mode. Comparing the test cases, the second and third harmonics of the fundamental ~3kHz peak in test 9 also have higher amplitude.

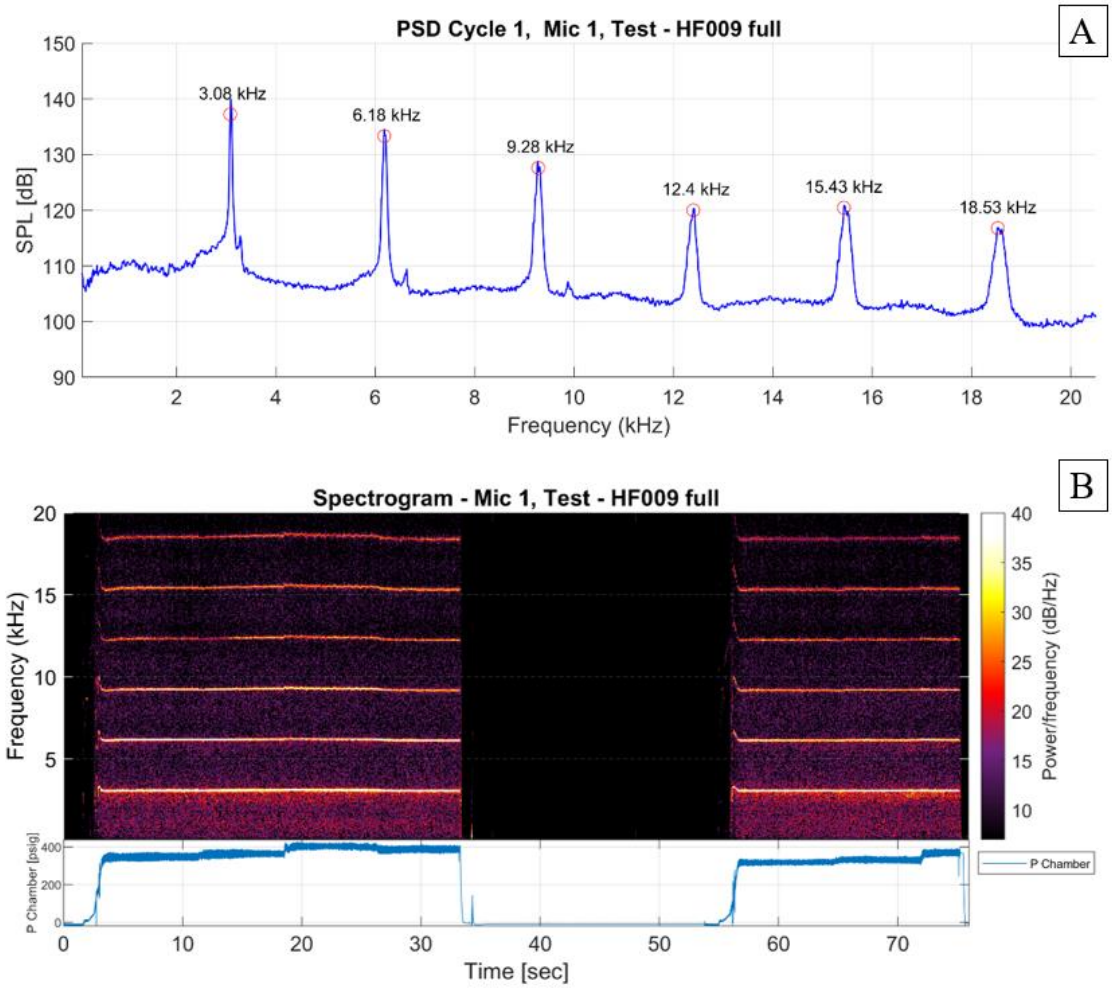

Figure 50. Test 9 PSD (A) and spectrogram (B) – detonation case, 1 wave.

Test 7 (CR of 1) below is shown to illustrate two consecutive cycles with different wave properties. Cycle 1 of test 7 shows operation similar to test 6 (though more unstable), as this appears to be a one-wave mode from the spectrogram. However, upon restart, a different mode appeared than had been encountered in other tests during the campaign. This was likely caused by changes in upstream propellant properties (T or P) between tests from leaks and ports missing between tests. Thrust data from this test indicated that this mode was likely that of a two-wave mode. The peak-to-trough of the thrust data is markedly lower for the second cycle compared to the first. This will be further expanded on in a later section. High speed video was not available for this part of the test due to the total duration of the hot fire and limitations on internal memory. Further plots of sensor data with the spectrogram will be investigated. Note, the chamber pressure sensor connection in cycle 2 of the test 7 spectrogram was damaged and so the pressure shown in cycle 2 is not physical.

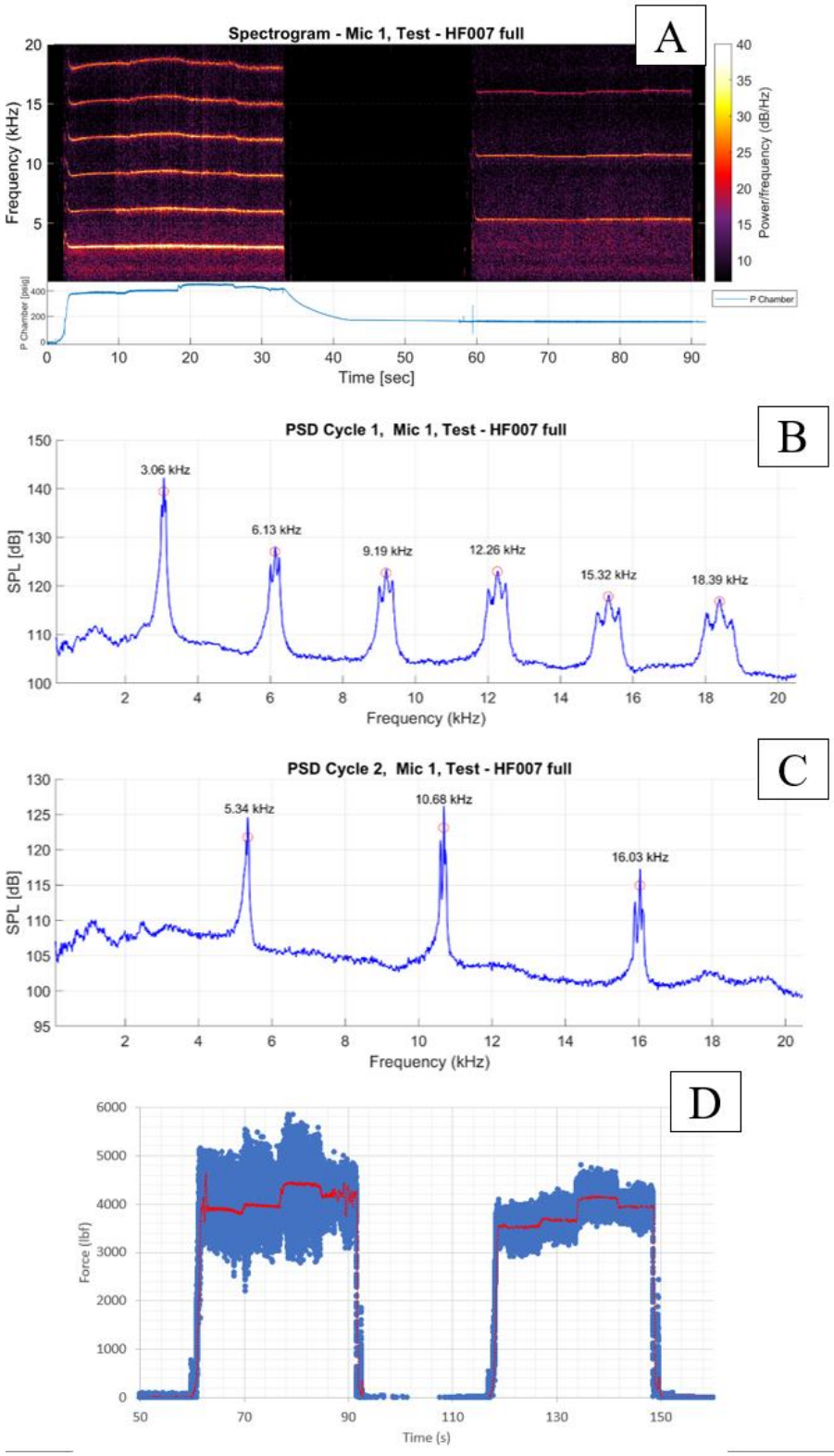

Figure 51. Test 7 spectrogram (A), PSD (B & C) and thrust data (D) – mode shift between hot fire cycles from single wave to likely two-wave mode.

Test 12 (CR of 1.13) below is shown to illustrate wave trends over mission-duration hot fires. This test utilized a new injector that increased the number of elements from 70 to 90; the high-performing and high element density variant led to a shift in the wave fundamental frequency. This test illustrated a two-wave mode with mode switching and counter propagation as indicted by the increase in nonharmonic frequency peaks as the test progressed. These frequencies are deemed nonharmonic (i.e., non-chord tones) as they do not align with the fundamental operating frequency and its harmonics. These are shown in the PSD spectra below along with their growth over time in the spectrogram. Toward the end of the test, the combustor shifted modes entirely; this mode ended up being the same mode seen in test 7 cycle 2. Further analysis will be conducted with sensor data to analyze the cause of these nonharmonic peaks and resultant mode shift. This method for comparison of data could be useful for quick looks of long duration tests without the use of high-speed video to validate if counter propagating modes are present.

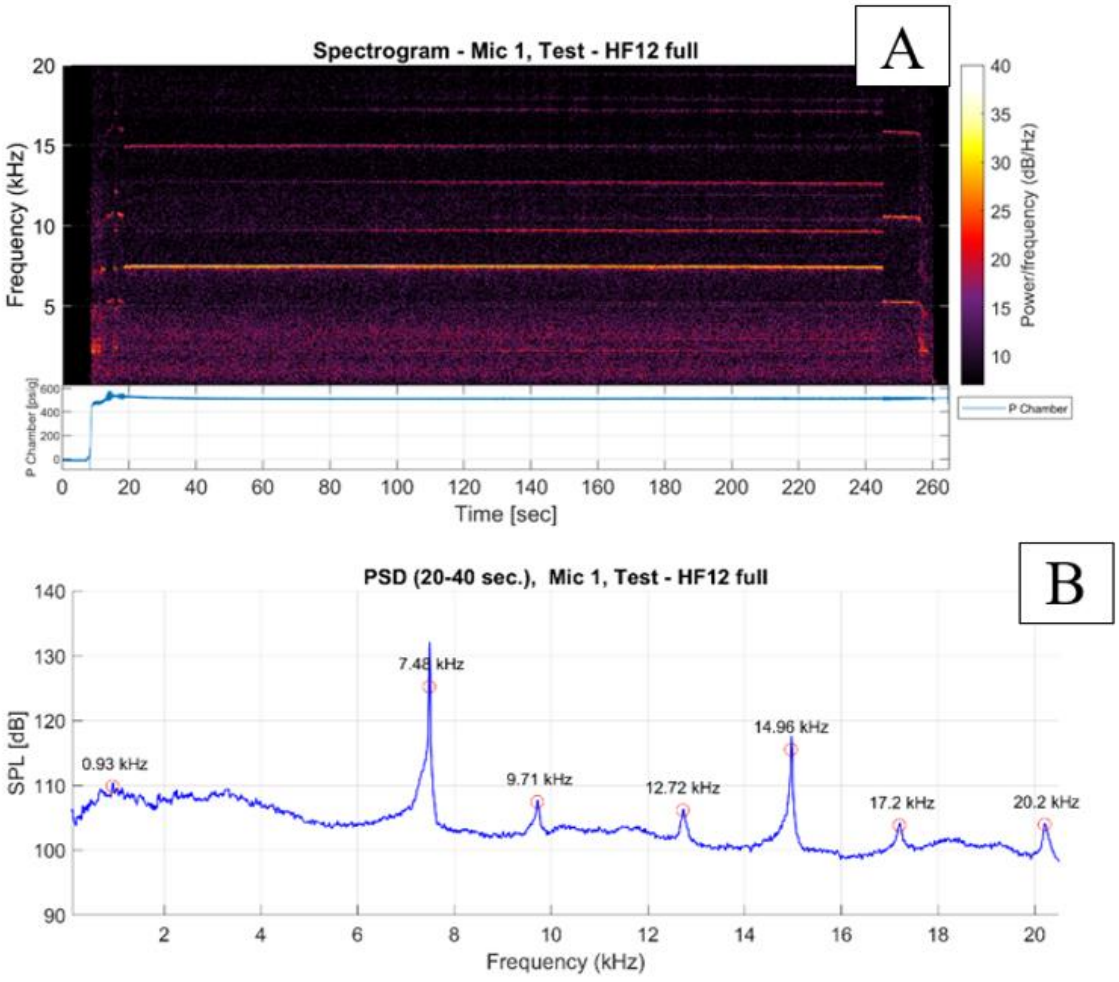

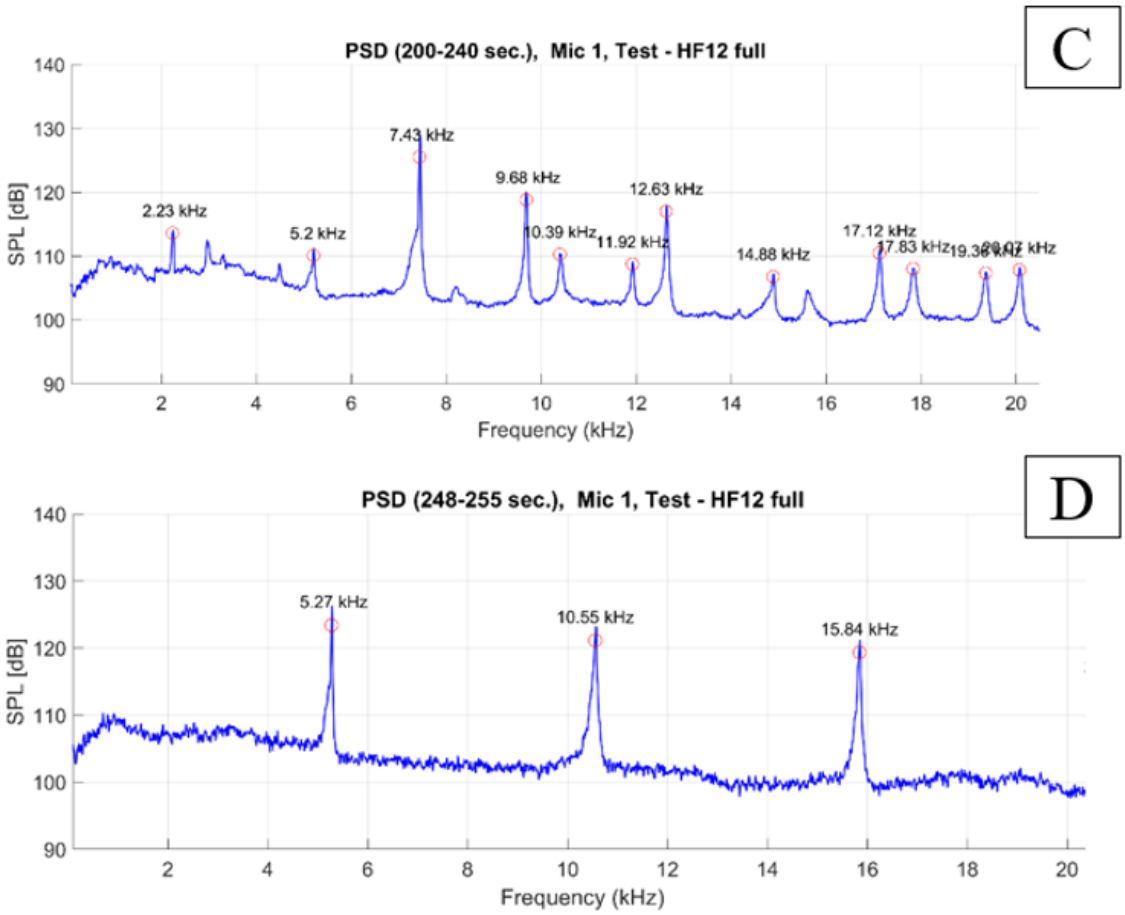

Figure 52. Test 12 spectrogram (A) and PSDs (B, C, D) – mode shift during test.

Total SPL was extracted from the microphone data to aid in discerning between one- and two-wave modes. Both peak and RMS values for the sound pressure level (SPL) were plotted over time. From the plots, one-wave modes are evident by the immense increase in noise (~10dB RMS). For reference, an increase of 10 dB equates to a 10X increase in sound power and a 2X increase in perceived loudness. This trend can be best seen for test 7, where in cycle 1 the peak signal was starting to clip—RMS values shown illustrate this ~10dB drop off between these wave modes, indicating that a two-wave mode or higher is desirable from an acoustics/structural dynamics perspective. Furthermore, comparing the two-wave RMS SPL to the deflagration RMS SPL of test 1, we observe similar noise levels.

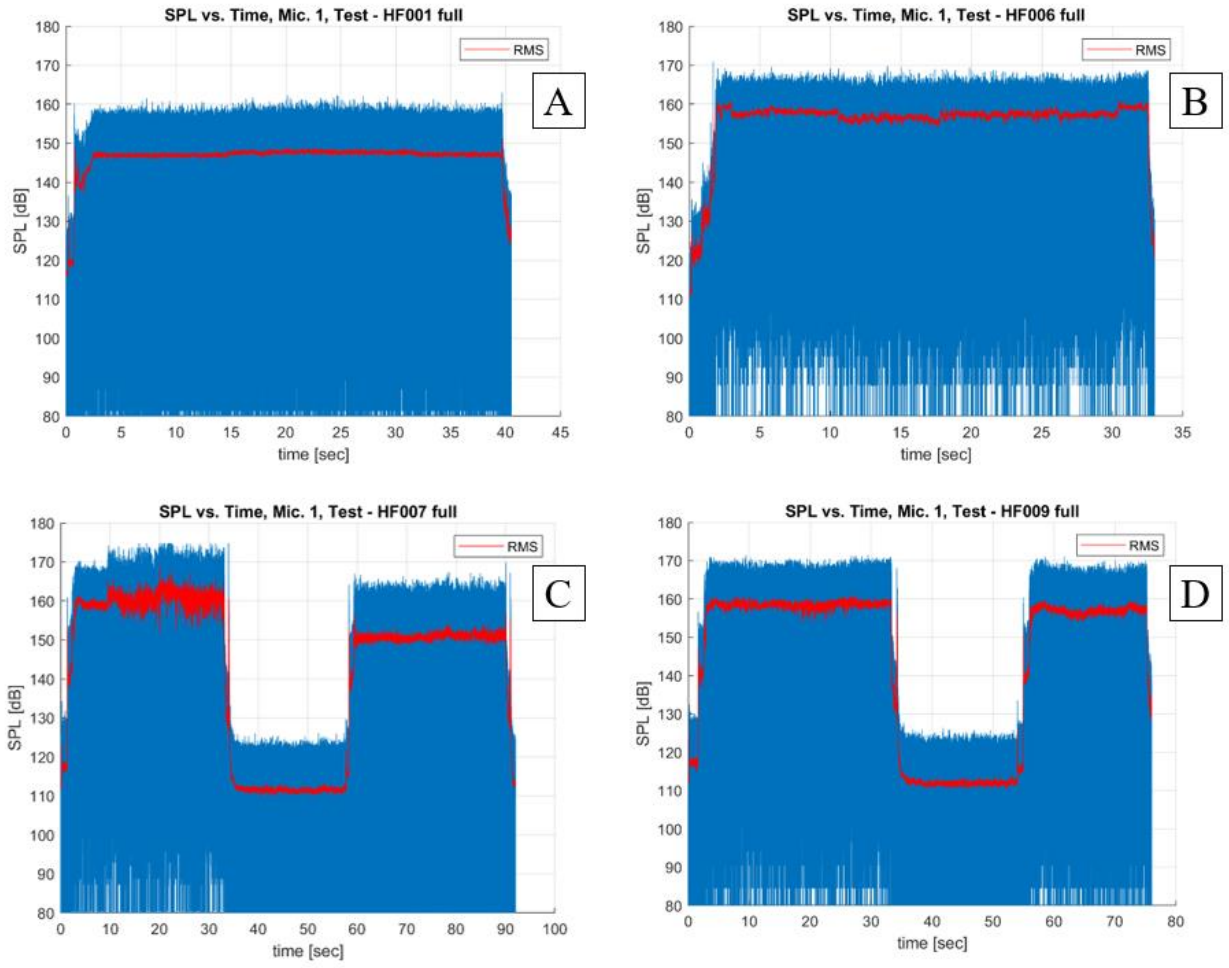

Figure 53. SPL vs. Time – test noise levels from 24" laterally to TA.

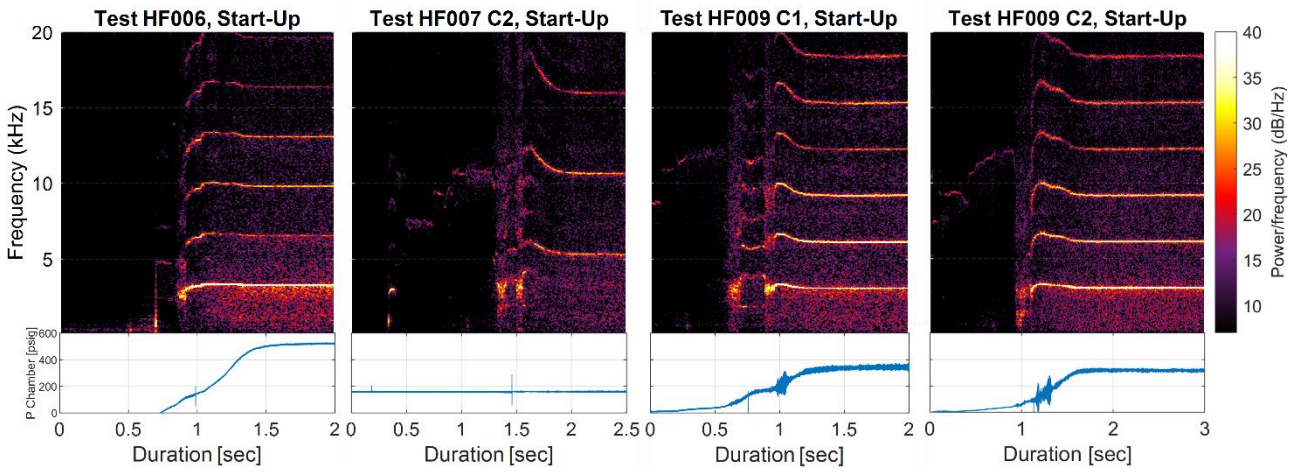

Figure 54. Wave behavior during startup.

An additional trend noted in the spectrograms (and audibly in microphone .wav files) was the wave behavior during startup. Immediately after ignition, the wave frequencies ramped up as the chamber pressure ramped up, and each time the wave speed would overshoot to a degree before settling on a mode at steady state chamber pressure. From these plots, it appears the startup frequency behavior (wave behavior) can potentially be modeled as a damped oscillator. Further analysis will be done to determine the degree of damping (over/under/critical) and how this effect changes between test conditions.

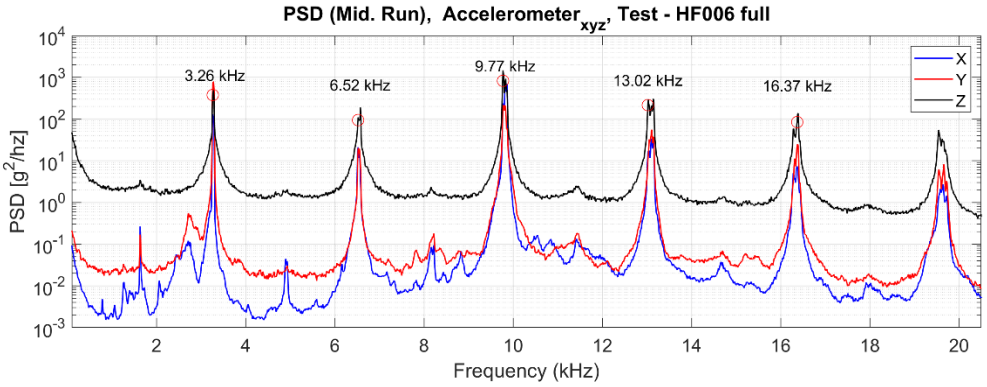

Figure 55. Accelerometer data.

Accelerometer data was taken throughout the SWORDFISH test series. While many tests yielded unusable data resulting from calibration, positional shift, or cable disconnection, test 6 results were clean. A power spectral density was calculated for each of the 3 axes and the data was plotted on top of one another. Comparing the Figure 13 accelerometer PSD and the Figure 7 microphone PSD plots, the frequencies correctly line up. This corroborates that wave activity can be picked up reliably by microphones. The accelerometer data also provides a lens into the high-G forces experienced by the hardware. The units of the PSD are in g^2/hz and can be used to estimate the Gs experienced at each frequency peak. Of final note, the accelerometer used in the SWORDFISH test series had a range of 1000 Gs and several of the one-wave modes resulted in signal clipping. Two-wave modes resulted in data much more like deflagration-based hardware at this thrust class, where signal clipping was not present.

7.3 WAVE BASED TORQUE MEASUREMENTS

Force measurements were taken using a set of 6-degree of freedom triaxial piezoelectric load cells. The four sensors were placed equally around the RDRE thrust mount- in this case, 7 inches in radial direction from the RDRE's center of mass. The equations used to calculate forces and moments about each axis were supplied by the KISTLER Multicomponent Force Link Set, Type 9366CC Instruction Manual. Each sensor takes measurements every 0.001 seconds.

The test cases highlighted in this section include SWORDFISH hot-fire 010 which was selected because it demonstrated two waves with changing wave direction. A single wave mode was observed during SWORDFISH tests 002 through 009, propagating continuously in the same direction (clockwise) for the entirety of each test with no CP waves visible after start-up, which is represented by SWORDFISH hot-fire 006. SWORDFISH hot-fire 001 only yielded deflagration and was included to give a contrasting example of deflagrative moments of the same combustor. Data from WHALE, a NASA constant-pressure liquid rocket engine of similar thrust class, was also included to compare the differences in torque.

A comparison of moments measured about the z-axis for the four hardware configurations is shown below in Figure 56. The Z axis moment with respect to time for WHALE (Figure 56A); SWORDFISH hot-fire 001 (Figure 56B); SWORDFISH hot-fire 006 (Figure 56C); SWORDFISH hot-fire 010 (Figure 56D).

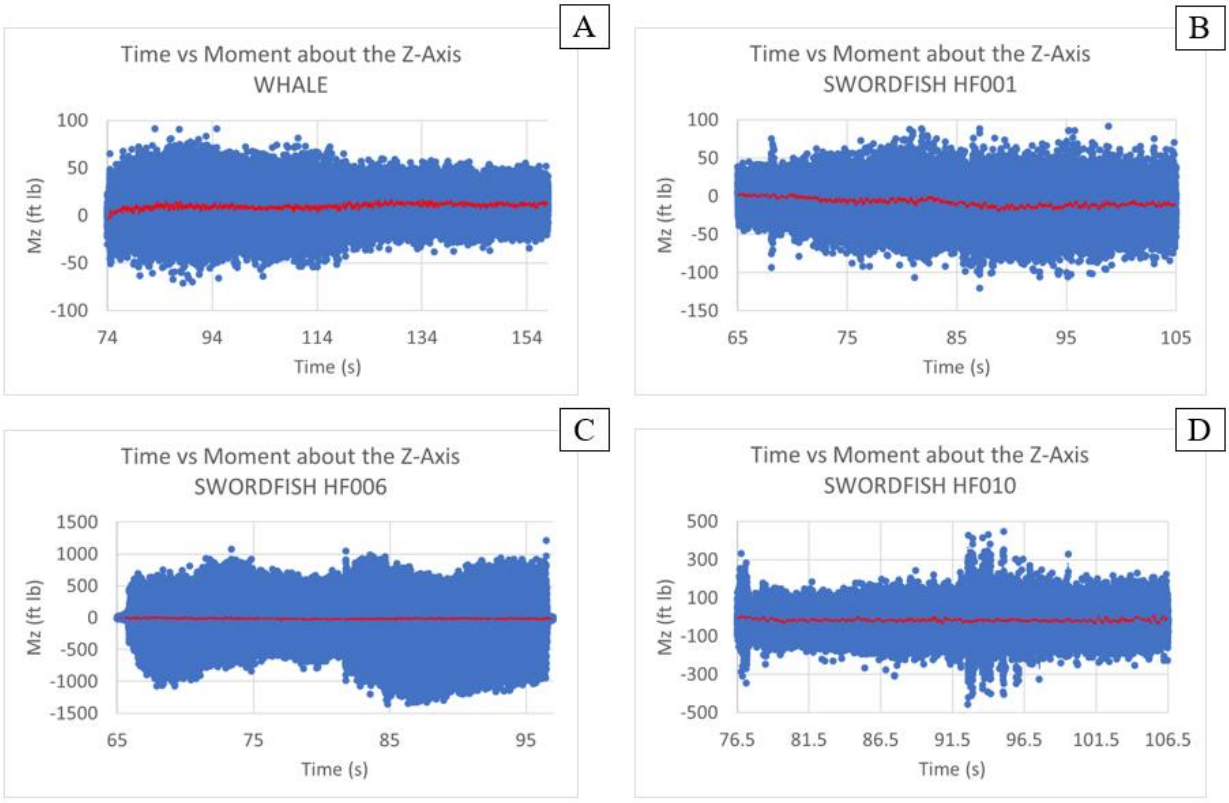

Figure 56. Measured moments about the z-axis for various testing configurations; A) constant pressure deflagrative engine, B) deflagrating RDRE test case, C) RDRE 1-wave test case, D) RDRE 2-wave test case.

The moment about the z-axis for all four test cases were graphed from start-up to shut down. Interestingly, two wave z-axis moment data have a peak-to-trough of approximately 2-3 times larger than the RDRE case with no waves and the constant-pressure case. However, the average moment changes very little throughout the duration of all tests, regardless of the number of waves. SWORDFISH 006 had one wave and showcases even higher z-axis moment measurements, approximately 10 times larger in magnitude than the constant-pressure engine or the deflagrative case.

SWORDFISH used methane/oxygen propellants, while ARDVARC used hydrogen/oxygen. For ARDVARC, only moment data was obtained for phase 1 hydrogen/oxygen testing. A failure of the inner body caused a stand fire which burned through several load cell cables losing the ability to measure moments in the methane/oxygen test phase.

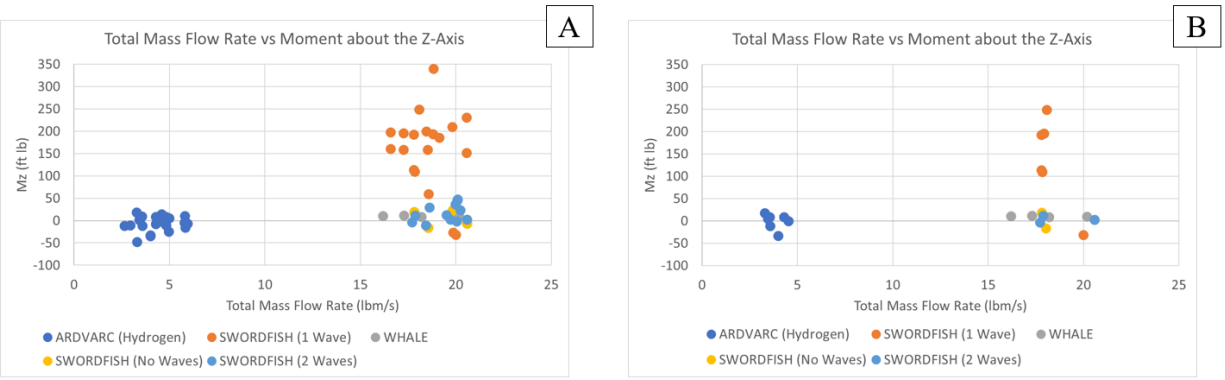

Figure 57. Torque about the Z-axis as a function of total mass flow rate for each level of testing (A) and level 2 specifically (B).

Figure 57A shows the relationship between mass flow rate and torque about the z-axis for each throttle point tested, while Figure 57B shows the relationship between mass flow rate and the torque about the z-axis specific to level 2 of testing. Level 2 was singled out because of the high degree of certainty that the facility had no instances of leaks, while later points in the hot fire, for multiple hardware configurations, did see high instances of leaks and likely induced error in calculating total mass flow rate to the annulus.

At the same mass flow rate, WHALE (a constant pressure thrust chamber) had torque comparable to SWORDFISH with either zero or two waves, and ARDVARC no waves during the hydrogen test phase. This means that in the case of two or more waves (or a balanced dynamical system), the moment about the z-axis is similar to a constant-pressure combustor. If data from SWORDFISH is directly compared (i.e. zero waves, one wave, two waves), one wave cases show a much greater average moment magnitude about the z-axis than tests with deflagration (0 waves) or 2+ waves. Additionally, there does not appear to be a correlation between test conditions and torque, but the majority of torque data points for the SWORDFISH one wave cases coalesce between 150 and 200 ft-lbs. However, this observation is muddled by several single-wave data points converging to a torque near zero. When looking directly at cases from level 2 hot fires, the data appears to indicate that the non-zero torque is reliable for single wave cases with the exception of a single data point.

The data presented in Figure 58 is normalized by the total Z-axis thrust to obtain a fractional percentage of total thrust. These data indicate that the percentage of total thrust is, on average, approximately 5% for single wave test cases. It also appears to be highly variable for ARDVARC hydrogen data centered about 2-5 lbm/s. Further investigation is needed to identify if the measured torque is real.

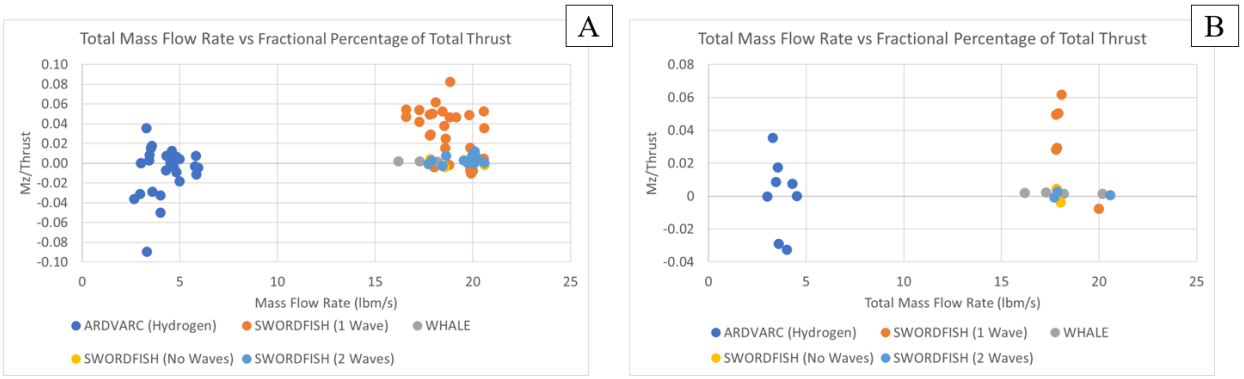

Figure 58. Torque about the Z-axis normalized by the Z-axis total thrust as a function of total mass flow rate for each level of testing (A) and level 2 specifically (B).

Figure 59 illustrates high-speed footage taken at 60,000 frames per second for SWORDFISH hot-fire 011. For this particular test, two waves were observed to change in direction occurring approximately two seconds after ignition and after waves had fully established. In this time period, the wave modes were unstable and multiple CP waves were present, typically four waves in total. The waves changed directions at 208.881 seconds and again at 208.883 seconds. Those times are both peaks in the time vs moment graph Figure 60. Unfortunately, this is not likely meaningful as the data was not sampled at a high enough rate to make any conclusive observations.

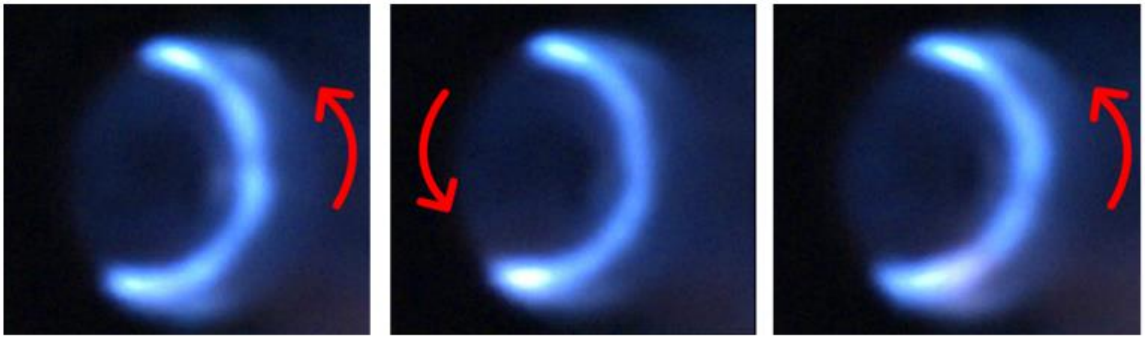

Figure 59. High-speed photographs of waves in RDRE annulus during SWORDFISH HF011.

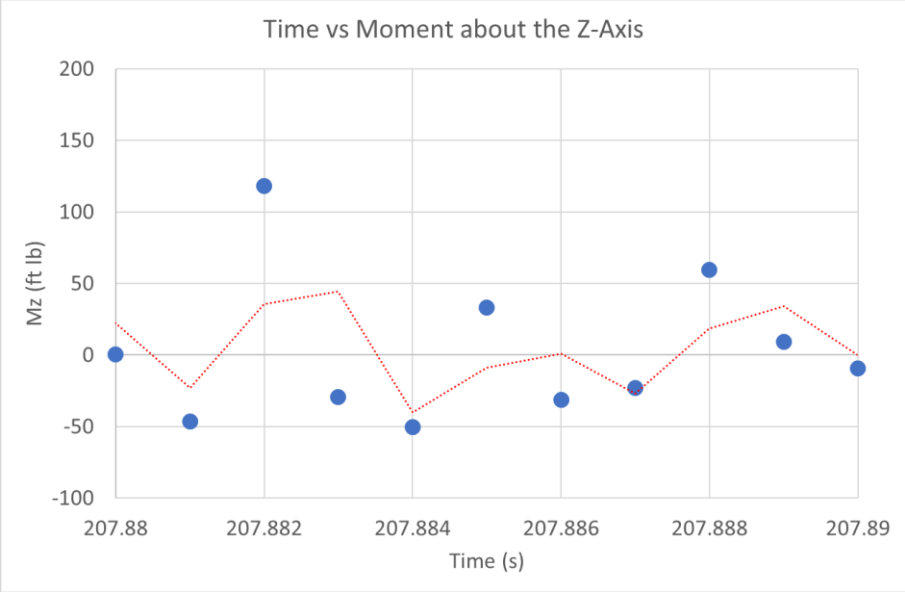

Figure 60. Moment about the Z-axis over time for hardware tested in SWORDFISH HF011.

During SWORDFISH hot-fire test 010, the waves switched direction near the beginning of the test but evened out approximately two seconds after ignition. This specific example was after start-up. Figure 61 shows a positive moment at 78.47 seconds into the test, highlighted by the orange data points. At 78.48 seconds, the waves have begun to rotate clockwise, creating what appears to be a negative moment about the z-axis; and at 78.49 seconds, the waves changed direction back to counterclockwise, which is shown in the graph below as a positive moment about the z-axis. Visually, this looks identical to the images in Figure 59. Similar to the SWORDFISH test case 011, there were multiple CP waves, so it is unclear whether the waves truly impart a moment with changing direction.

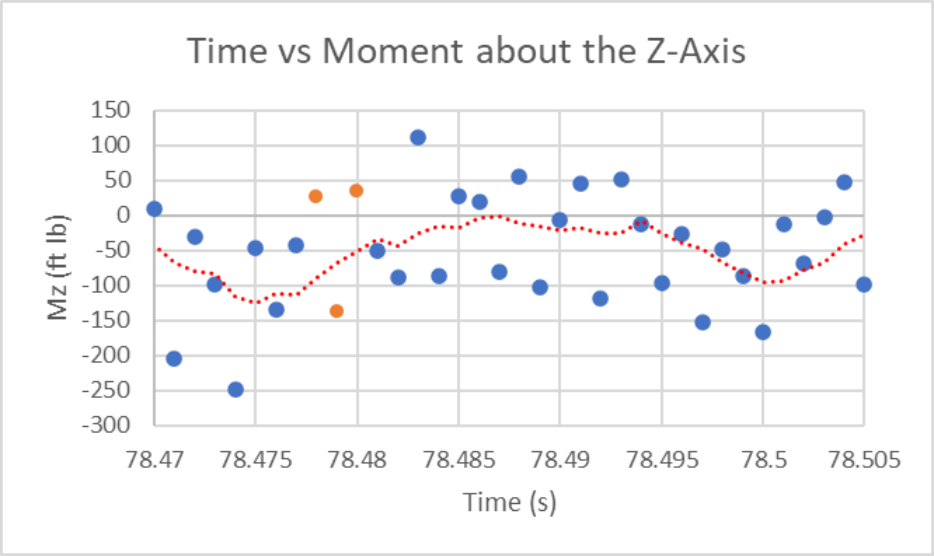

Figure 61. Moment about the Z-axis during a time snippet from SWORDFISH HF010.

To conclude, there is some evidence that suggests when waves change direction, the average trend in torque about the Z-axis shows a shift in moment (from positive to negative slope or vice versa). In addition, for a balanced dynamical system where two or more waves are present, the time average magnitude in torque is near zero. However, a single wave does appear to impart a significant torque of around 4% of the total Z axis thrust.

7.4 PROPELLANT COMPARISON (HYDROGEN VS. METHANE)

Several studies have investigated methane/oxygen RDREs of various scale. [22] [23] [24] [25] but there have been considerably fewer studies that have investigated hydrogen/oxygen RDREs. [22] [26] [27] Generally, at equal mass fluxes, the number of waves observed with hydrogen propellant is greater than the number of waves observed with methane propellant. Possibly in the range of 5-15x more. However, many of the experimental data sets available were conducted with very small annulus gap widths. Based on observations from the literature, a higher chemical kinetic rate of reaction fuel, such as hydrogen, may prefer a larger gap width while slower chemical kinetic rate propellants such as peroxide/hydrocarbon fuels may prefer a smaller annulus gap width and a larger mean circumference. There is not enough data currently to identify specific trends or comparable results between the two propellants, however inferences can be made such as those above.

NASA MSFC conducted further RDRE testing under the SWORDFISH project with hydrogen as fuel in April 2024. Unfortunately, limited results were able to be gathered and those that were did not show evidence of detonation modes. For clarification, the graphs below refer to hot-fire test #13 (HF013). While this test was technically the 13th hot-fire under the SWORDFISH project, it was, in fact, the first test run with hydrogen as the fuel.

Figure 62 depicts the Power Spectral Density and spectrogram from microphone data collected during SWORDFISH hot-fire test #13. Unfortunately, in addition to having no visual evidence of wave activity, the microphone did not pick up indications of wave modes. Figure 62A displays no dominant modes while Figure 62B has no noticeable modes in the spectrogram. These trends are what is expected of a stable, deflagrating rocket.

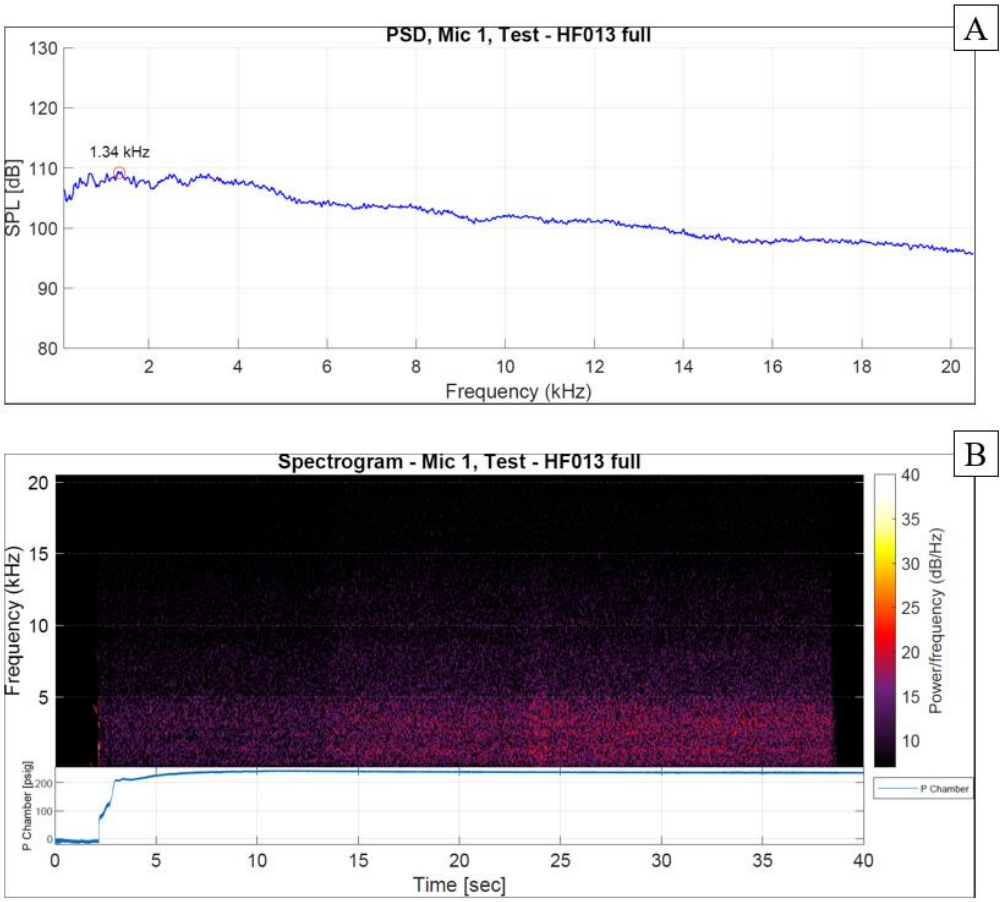

Figure 62. SWORDFISH (H2) test 13 PSD (A) and spectrogram (B) – evidence of deflagration.

However, it is of note that the microphone data did appear to pick up some wave activity at start-up of HF013. These potential pop-up modes are illustrated in Figure 63. These brief, transient wave modes devolve into typical deflagration as discussed above.

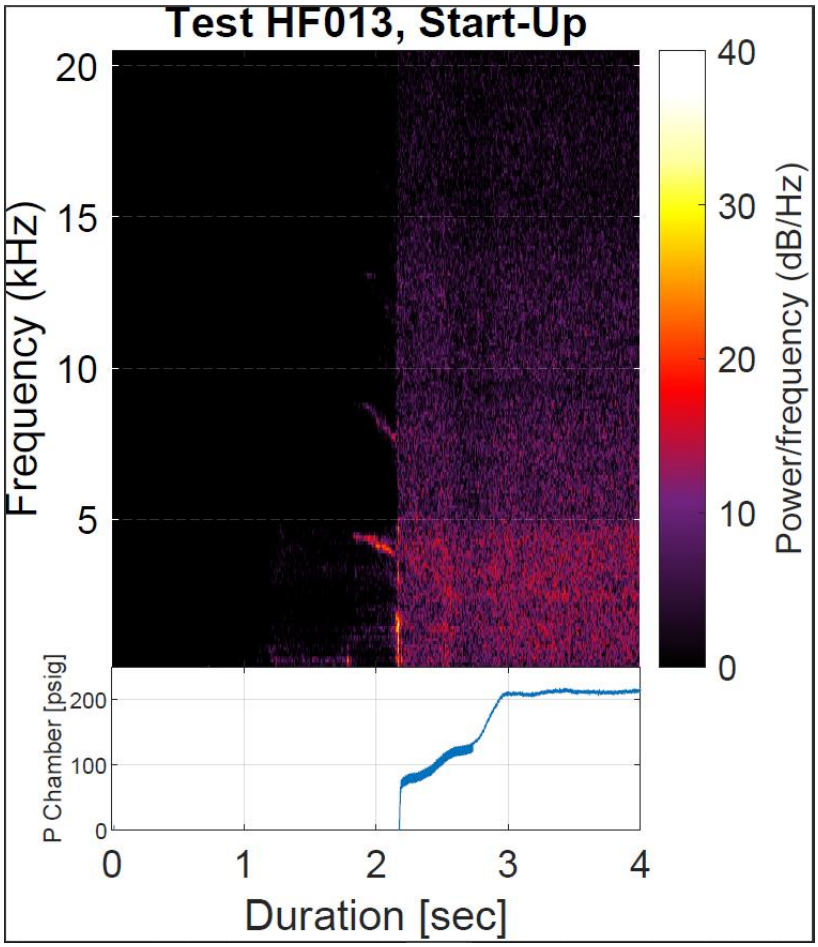

Figure 63. SWORDFISH (H2) test 13 wave behavior during startup.

The SWORDFISH project was not able to generate enough data points to draw conclusive comparisons between the use of hydrogen and methane fuels in like-RDRE hardware. However, the few hydrogen data points that SWORDFISH did generate offer valuable insight into trends that are worth further investigation. Firstly, it was evident that, for both hydrogen and methane testing, the gap width of the SWORDFISH hardware was too large for it's overall circumference to yield high performance. While hardware cooling benefitted from the ratio, both fuels underachieved in efficiency and wave mode generation which indicates that a more optimal gap-to-circumference ratio is worth further exploration. Additionally, hydrogen testing produced significantly lower efficiency with significantly less (zero) wave modes than expected. The highest Characteristic Velocity (C*) seen with hydrogen was ~77%. While there are several factors at play and a dire need for more data, hydrogen's underwhelming performance in this case indicates that there are more optimal RDRE hardware geometries and input parameters that can be used to increase performance. Hardware and parameters may need to be designed specifically for the type of fuel and may not be one-size-fits-all.

7.5 SINGLE WAVE OPERATION

Testing of the SWORDFISH hardware was conducted using both LCH_4/LOx and LH_2/LOx where both fuel and oxidizer were routed through integrated coolant channels in both the inner body and outer bodies. All observed wave activity for methane test cases was found to fall between 45% and 52% of the theoretical Chapman-Jouguet (CJ) velocity, or the maximum

theoretical velocity for a detonation of a specific mixture. This is between 94% and 110% of the medium's constant pressure combustion burned gas sonic velocity. All single wave modes were found to be supersonic while the two wave modes were found to be sonic, or transonic. All wave velocities were found to be between 3900 and 4600 ft/s with the clockwise propagation for most cases. Only a single hot-fire, test 1, did not yield visual or audible evidence of wave activity. The second cycle of test 7 also did not show audible evidence of wave activity, but this was likely due to off nominal operating conditions stemming from a facility leak. The test 1 hardware configuration was a straight annulus with contraction ratio of 1. In terms of wave formation, regardless of total mass flow into the annulus, mixture ratio, or CR tested, a single wave was almost always observed. The exception to this was when a new injector developed in partnership with Venus Aerospace was tested. This injector had 90 injector elements as opposed to 70. An increase in the number of elements caused an increase in the number of waves, albeit at a lower velocity. This is not unexpected given many researchers have report wave slowing when transitioning to a higher number of waves. An image of a single wave mode is shown in Figure 64.

Figure 64. Single wave traveling clockwise about the annulus.

A major takeaway from this test phase was that repeatability of detonation may require a slight contraction ratio. This is consistent with the available literature where cases of deflagration dominated flow fields for select test cases with a straight annulus. [22] [23] [28] However, there may be other variables at play including increased injection temperature, sparseness of injector elements, or nominal operation conditions.

Additionally, single wave modes were found to impart unbalanced dynamic loading on the hardware. Tri-axial thrust measurements were taken in real-time using four piezoelectric force gauges as previously described. Figure 65 graphically depicts the measured thrust over the course of different SWORDFISH hot-fire tests; a single wave mode, 2-wave mode, and deflagration dominated combustion for comparison. The red points are the average thrust at that time stamp. The variation in thrust measurements for the 2-wave mode and deflagration have a much lower amplitude than the single wave mode. This high amplitude thrust measurement demonstrated by the single wave mode is much less desirable for a flight vehicle. Large vibrational dynamic loading on vehicles may interfere or damage critical systems, instrumentation, and the vehicle itself.

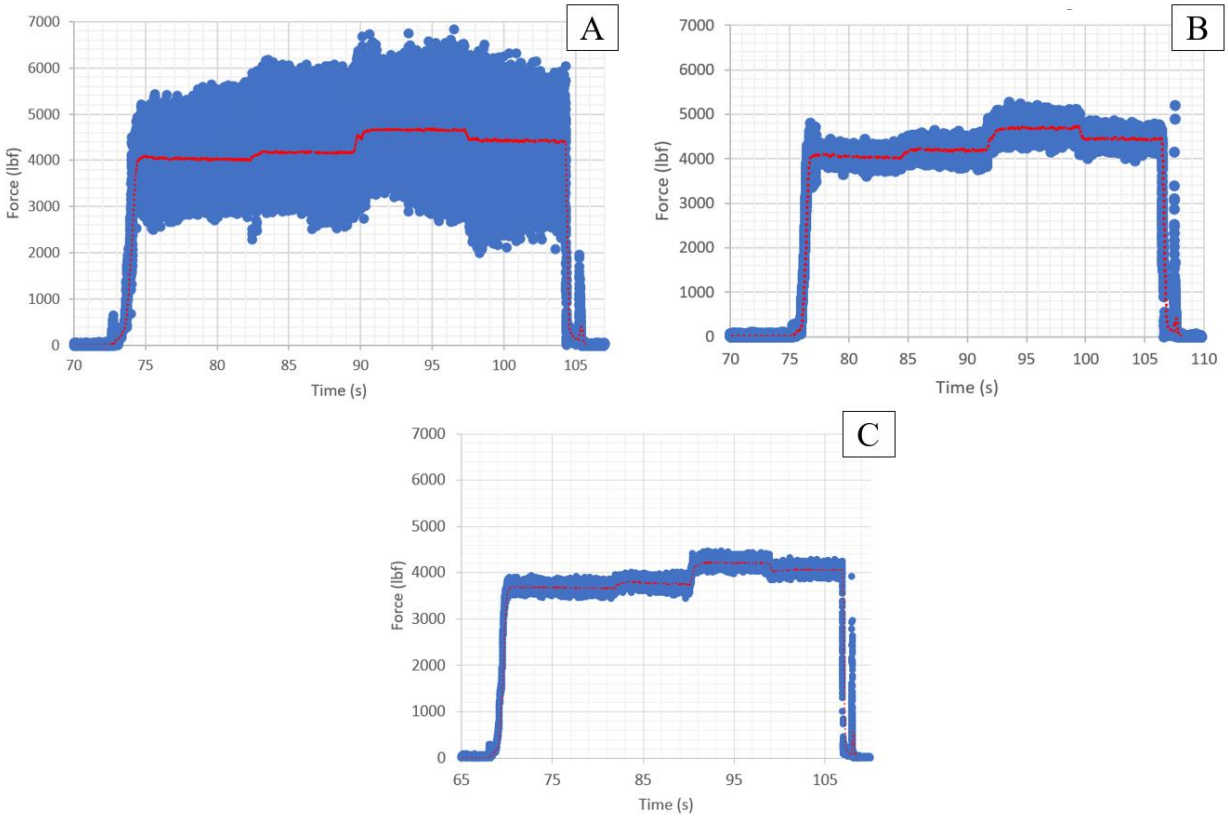

Figure 65. Thrust measurements taken during SWORDFISH full scale hot-fire of a single wave mode operation (A), a 2-wave mode operation (B), and deflagrative mode (C).

The data and trends seen above are corroborated by thrust data collected from sub-scale MARLEN testing. Figure 66 below shows similar trends in thrust and thrust noise with sub-scale hardware as those seen at full scale. This indicates that thrust noise trends are constant between different thrust classes of RDRE.

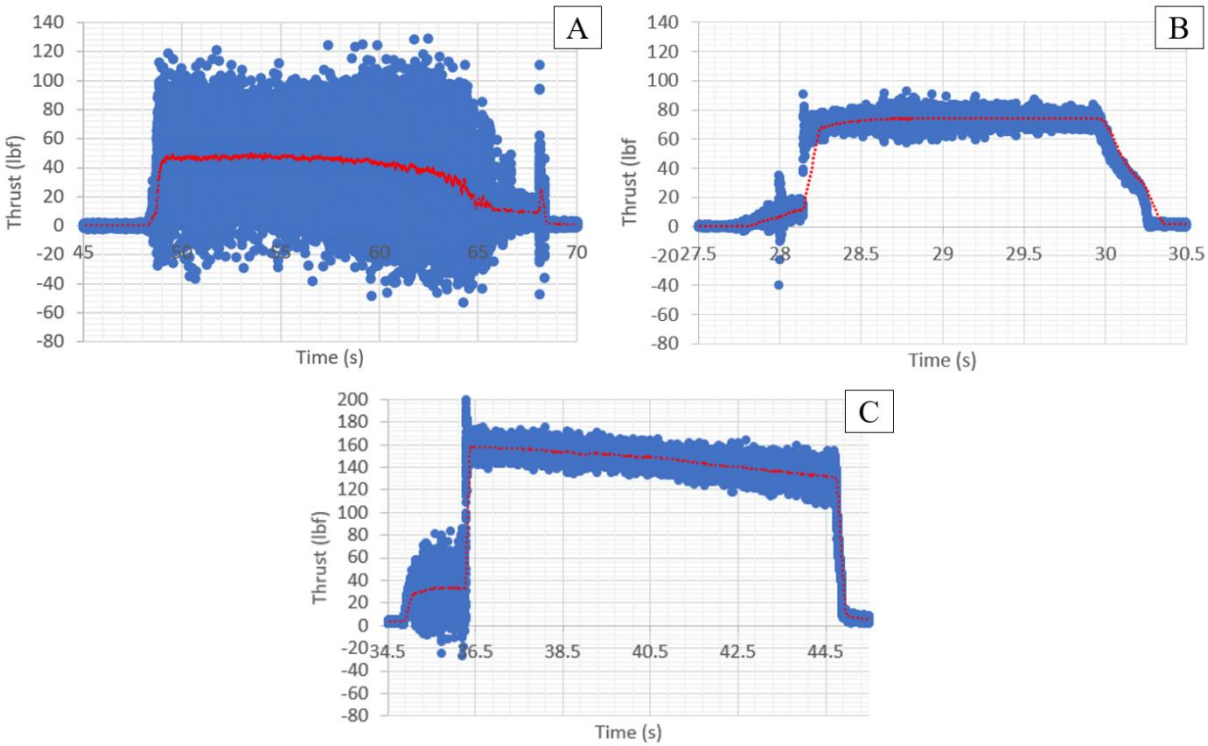

Figure 66. Thrust measurements taken during MARLEN subscale RDRE hot-fire of a single wave mode operation (A), a 2-wave mode operation (B), and 4-wave mode operation (C).

The single wave mode and unbalanced loading was found to be extremely detrimental to hardware. In many test cases, instrumentation tubing, ports, and feed lines were found to shear open or apart mid-test. Metal C-rings used to seal the outer and inner bodies to the injector were found shattered between tests as well. Finally, bolted joints were found post-test to be friction welded, embrittled, and fractured while flange tabs that were not fastened to anything were simply sheared off. A major takeaway from this work is that RDREs should be designed away from a single wave mode. The dynamic loading on hardware and likely future vehicle payloads and passengers would be detrimental to mission success. Figure 67 illustrates the impact that a single wave mode had on the instrumentation ports and lines.

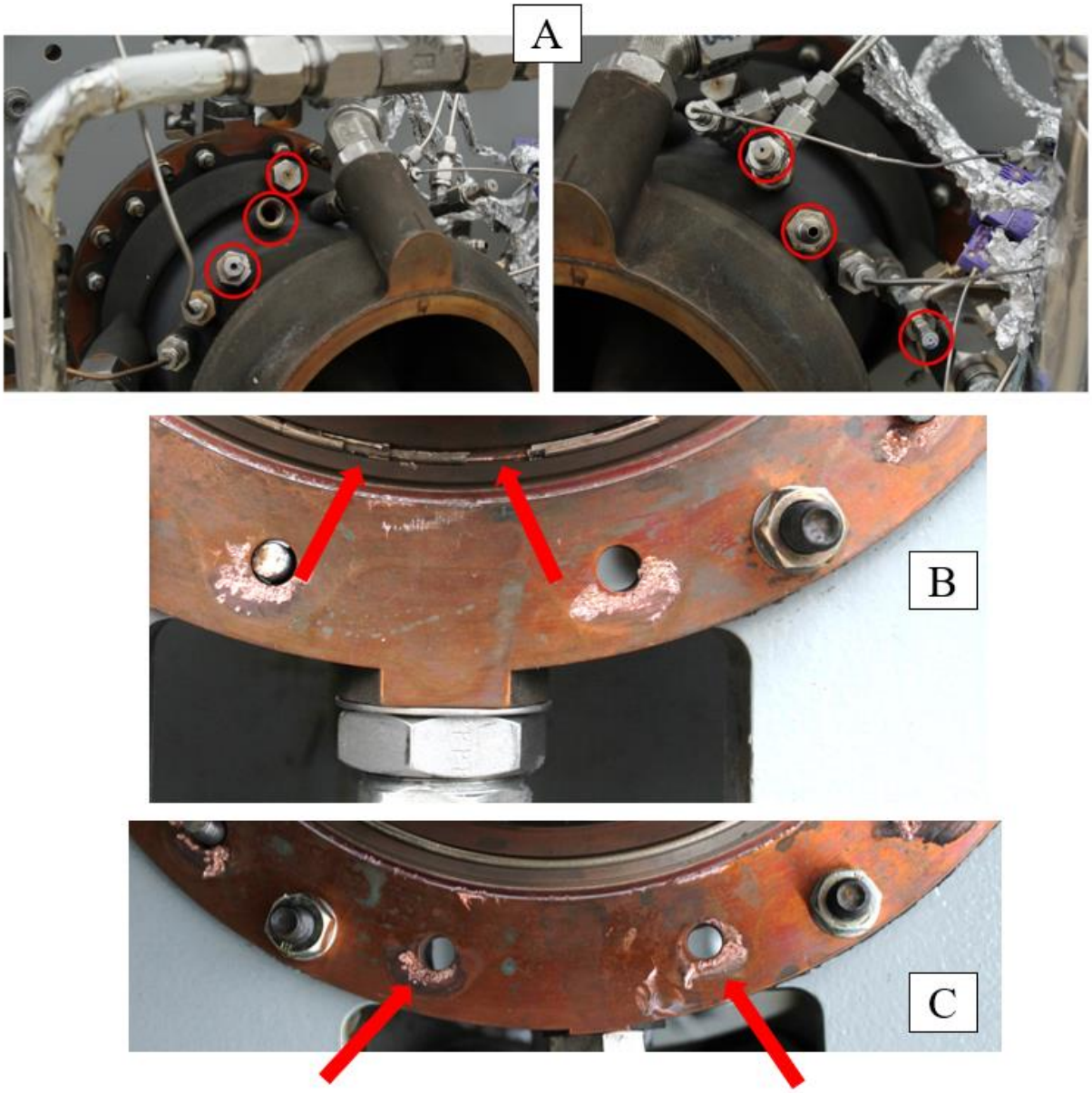

Figure 67. Images of instrumentation ports and lines that were sheared off during single-wave modes (A), broken C-seals (B), and melting/deposition of fused copper on outer body (C).

7.6 SUBSCALE TEST OBSERVATIONS

In an effort to better understand scaling relations and wave activity, a subscale 2-inch RDRE with internal water cooling was tested using gaseous methane-oxygen propellant. The primary means for investigating wave activity was through the use of high-speed videography with frame rates ranging from 60-200 kHz. For several tests, across a broad range of mass fluxes, CR waves were observed in addition to CP waves. Long duration tests lasted an average of 10 seconds which allowed for an analysis of RDRE operation after startup transience had

passed and thermal-steady state had been achieved. This is important because short duration burns may not be sufficient to capture mode switching effects that may only occur at thermal steady state.

The tests can be separated into those which never had CP waves, and those that did. In cases which did have CP wave modes, clockwise (CW) wave sets were usually dominant while counterclockwise (CCW) wave sets were usually dimmer and sometimes seemed to disappear entirely. In the first case, tests which never had CP waves always had higher wave speeds than tests which did have CP waves, for the same number of CW waves. In the second case, for tests which developed CP waves at any point in time, wave sets traveling CW and CCW always had the same speed. This is still the case even when CW waves appear to dominate. Wave velocity remains unchanged even when the CCW waves disappear entirely.

Throughout testing, only 1, 2, and 4 wave modes were observed during the thermal steady state operation. For this test campaign, the 1 and 2 wave modes usually appeared brighter than the 4 wave modes. This may be due to a higher rate of heat release from the larger proportion of well-mixed and available propellants. However, further investigation into the rate of heat release correlating to luminosity is still ongoing.

The straight annulus with a contraction ratio of 1 produced almost exclusively produced single wave modes, while the tapered and contoured inner bodies as shown in Figure 68 produced either 2 or 4 wave modes depending on throat mass flux.

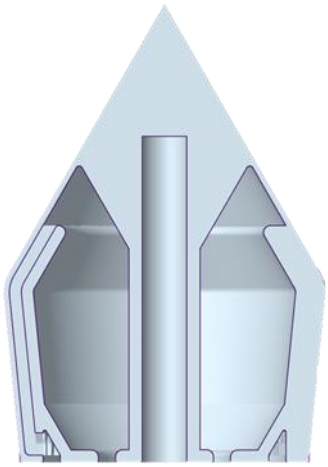

Figure 68. Contoured (left) and tapered (right) inner bodies.

Only a single test case with the straight anulus configuration produced two waves. This case corresponded to chaotic, unpredictable wave modes, where waves could switch direction spontaneously. Damage to the inner body was sustained during this test primarily due to the combustor exceeding its cooling capacity over a long duration run. The damage was confined to the inner body near the throat of the combustor where wall temperatures exceeded the material burnout limits. This suggests that the heat flux of a two-wave mode is higher than a one-wave mode.

In addition, for some tests, a 2-wave mode appeared during shutdown. This 2-wave mode appeared stable and decreased in brightness, but not speed, until extinguishing. It could be that during shutdown a decrease in mass flux and combustion chamber pressure, a change in mixture ratio, or a change in some other parameter caused the combustor to prefer a 2-wave mode. This mode was observed either with or without CP waves for different tests at shutdown. The waves continued propagating and became dimmer until they could no longer be seen. Backpressure and backflow were not observed during shutdown of these tests and no hardware damage was observed.

Finally, test 3 which corresponded to the lowest mass flow rate displayed some unique wave behavior. Instead of achieving a 1, 2, or 4 wave mode like the other tests, test 3 developed a “slapping” mode. This describes an operating mode where a detonation would initiate at one point in the annulus, and then waves originating from that point would travel in opposite ways

around the annulus. The waves would eventually meet at the opposite end of the annulus and extinguish, which was followed by a brief period of no detonation. This process would repeat in a cycle with a period much longer than a normal single wave period. The frequency observed on the slapping mode was roughly 3125 Hz. According to the wave frequency and spacing analysis conducted above, this frequency would correspond to a wave spacing of around 33 inches. This would result in a wave spacing which is larger than the average circumference of the MARLEN engine which is only about 5.93 inches. Ultimately, the mass flow rate was not high enough to sustain a single wave mode in this size combustor.

7.7 CONTRACTION RATIOS IMPACT ON WAVE SPEED

As presented in Figure 69, several variations on throat contraction ratio were tested under the SWORDFISH methane test phase. High speed video was captured for the first ~5-9 seconds of each test where wave performances were extracted. This section overviews the impact of contraction ratio on wave performance parameters, predominantly wave speed. Figure 69 below, plots the average wave speed as a function of contraction ratio for several tests where leaks in the facility were not observed.

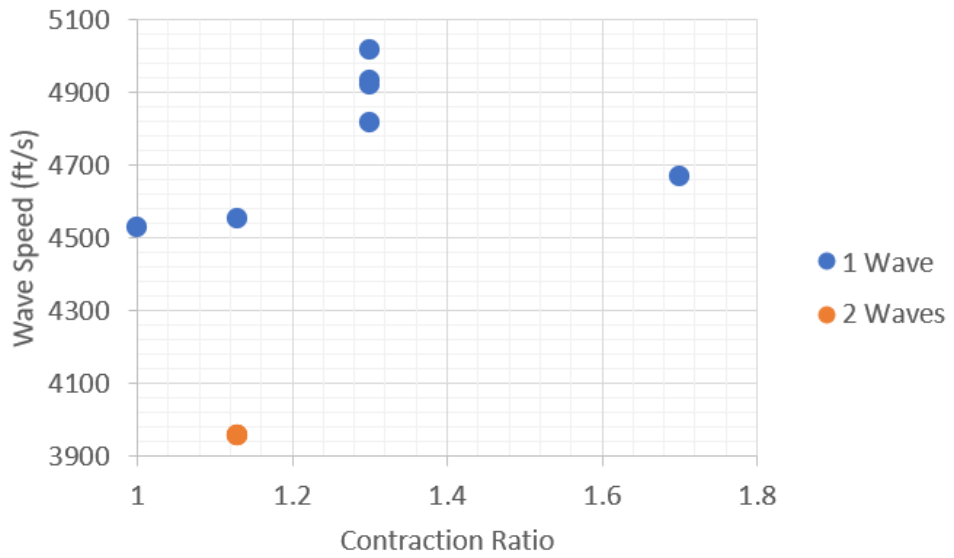

Figure 69. Wave speed as a function of contraction ratio for select tests during SWORDFISH methane test phase.

For most test cases, a single wave was observed with the 70-element pentad injector. When the injector was traded for the 90-element pentad injector, the number of waves increased to two, though at a lower wave speed and with CP modes observed from time to time over the 9 second high-speed video. In general, it does appear that for the RDRE designs tested the wave speed increases with increasing contraction ratio. A jump in wave speed is observed for two different outer bodies that form a contraction ratio of 1.3. This corresponds to a higher-than-average increase in combustion efficiency by about 3-5% but not necessarily a change in specific impulse. Some test cases demonstrated higher Isp, while others were lower on average in Isp. Further evaluation of contraction ratios effects on wave speed will be conducted with subscale NASA hardware in 2024.

8 COMPUTATIONAL EFFORTS

The efforts accomplished during this project have achieved a significant development effort of NASA Glenn's in-house CFD code: OpenNCC. A new chemistry model was created that allows non-ideal gas equations of state to be utilized by future researchers. This required a rewrite of many subroutines and new computational strategies to allow the CFD program to iterate using temperature and pressure as state variables. The chosen equation of state model includes NIST's thermophysical property and mixture models for parahydrogen and oxygen in addition to NASA polynomial fits to open the solution space from cryogenic to ideal gas states (54.361 K to 5000+K). This methodology in stitching together two different equations of state over a temperature interval is currently a part of the developer's PhD dissertation at Case Western Reserve University.

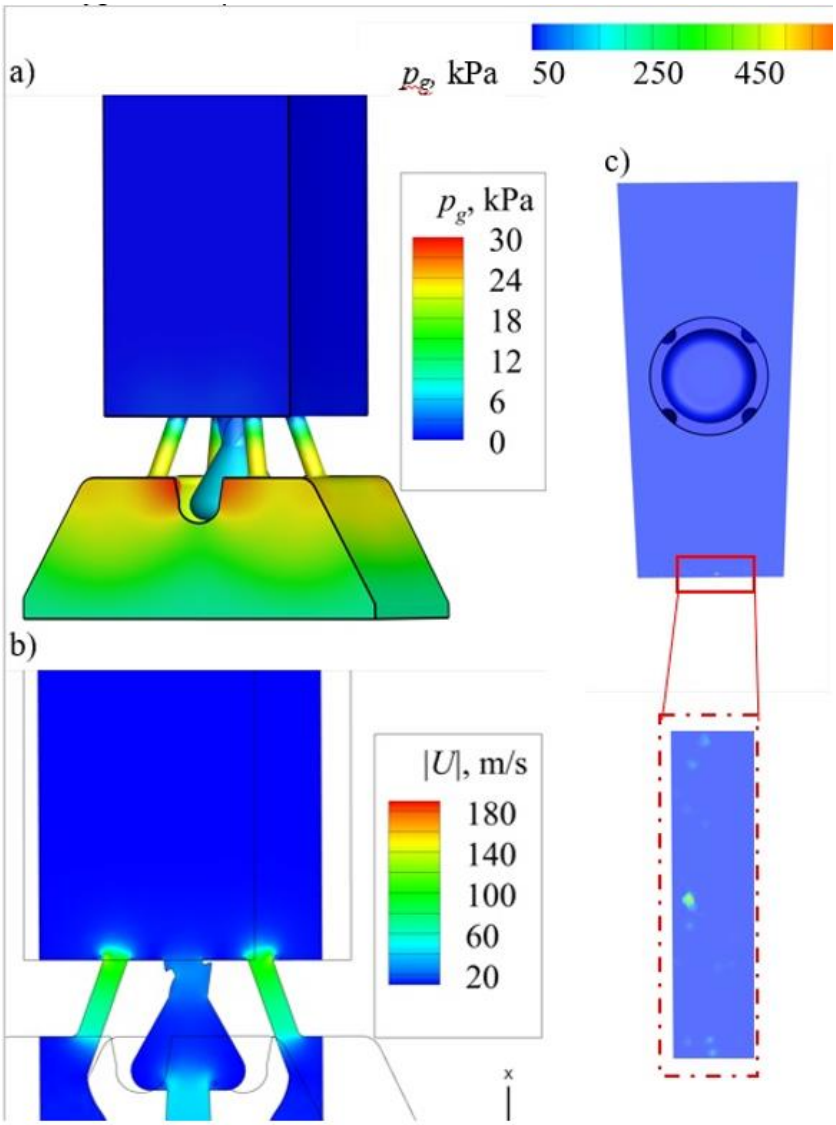

Figure 70. Modeled example of an injector element with unique geometry.

The modeling strategy consists of utilizing the mixture and individual species models selected as an adopted best-practice from NIST for the region below 1,000 K for a mixture of parahydrogen

and oxygen. The species are modeled as semi-empirical finite series equations in the form below. The second term is a new term in α^o which includes species that only have polynomial fits for thermophysical properties.

$$\alpha = \alpha^o(\rho, T, \bar{x}) + \alpha^r(\delta, T, \bar{x})$$

$$\alpha^o(\rho, T, \bar{x}) = \sum_{i=1}^{N} x_i\left[\alpha^o_{o,i}(\rho, T) + \ln x_i\right] + \sum_{k=1}^{N} x_i\left[\alpha^o_{o,k}(T, P) + \ln x_k\right]$$

$$\alpha^r(\delta, T, \bar{x}) = \sum_{i=1}^{N} x_i[\alpha^r_{o,i}(\delta, \tau) + \sum_{i=1}^{N-1}\sum_{j=i+1}^{N} x_i x_j F_{ij}\alpha^r_{ij}(\delta, \tau)$$

These equations can use all species previously modeled in OpenNCC's finite rate chemistry model. Future development could implement other equations of state after the transition point. Above 1,000 K, the model shifts to regular finite-rate models as previously used in OpenNCC as needed for all combustion calculations. This occurs because of Hermite splines for thermophysical properties and the equation of state. This model developed under this work was first presented at the 2024 Spring Technical Meeting of the Central States Section of the Combustion Institute.

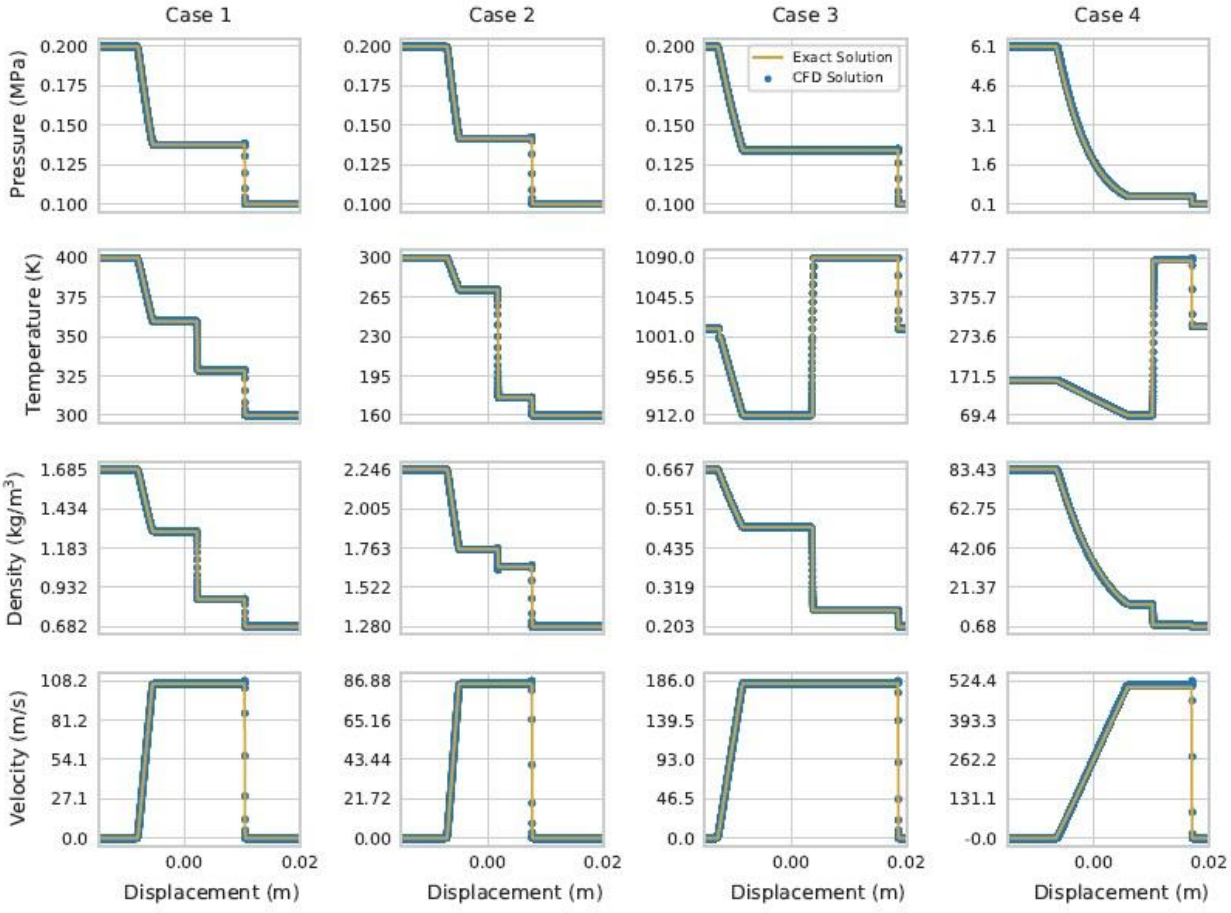

Figure 71 - CFD Validation Results

Table 5 - Selected Cases for CFD Validation

Driver Section			Driven Section		
Case 1 : Ideal Gas					
Pressure	Temperature	Mole Fraction	Pressure	Temperature	Mole Fraction
0.2 MPa	400 K	100% N_2	0.1 MPa	300 K	50% H_2 - 50% O_2
Case 2 : Cryogenic Region					
Pressure	Temperature	Mole Fraction	Pressure	Temperature	Mole Fraction
0.2 MPa	300 K	100% N_2	0.1 MPa	160 K	50% H_2 - 50% O_2
Case 3 : Transition Temperature Region					
Pressure	Temperature	Mole Fraction	Pressure	Temperature	Mole Fraction
0.2 MPa	1010 K	100% N_2	0.1 MPa	1010 K	50% H_2 - 50% O_2
Case 4 : Cryogenic Region at Condition					
Pressure	Temperature	Mole Fraction	Pressure	Temperature	Mole Fraction
6.1 MPa	160 K	50% H_2 - 50% O_2	0.1 MPa	300 K	50% H_2 - 50% O_2

The validation cases studied under this effort included Sod's shock tube, as seen in Figure 71, and a 1D detonation wave, as seen in Figure 72 and Figure 73. The shock tube cases studied for the displayed results are shown in Table 5. These were selected as cases that can compare to other equations of state and test the limits of the CFD code. Python codes were created to determine the exact solution of this equation of state and two others (comparing calorically and thermally perfect solutions). The CFD results successfully match the exact solutions of the four displayed cases.

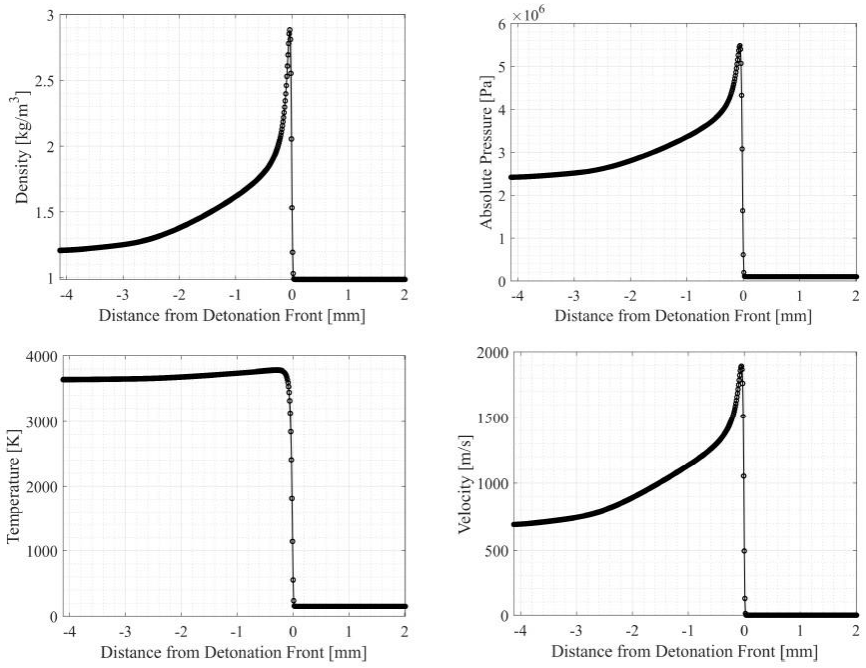

Figure 72 - 1D Detonation Wave CFD Result

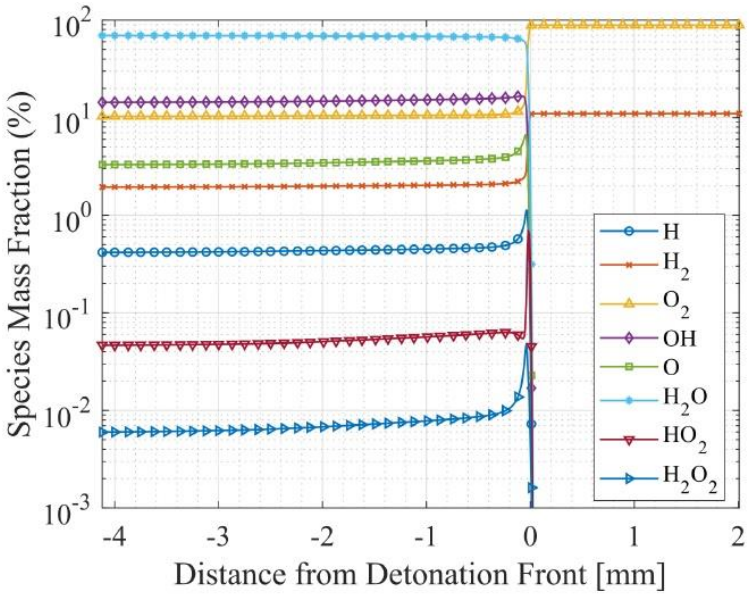

Figure 73 - 1D Detonation Wave Combustion Species

The work involved in creating this new chemistry model in OpenNCC involved significant reprogramming for a general equation of state that can use the semi-empirical model presented here. OpenNCC was previously written using ideal gas assumptions and this rework took the first year of the ECI to complete. The second year involved code validation to the shock tube problem presented above, a 1D detonation wave, and generating a mesh suitable for a single injector in the combustor of the SWORDFISH engine. Some initial results of a combustor injector are displayed in Figure 74 and Figure 75. The methods developed under this ECI and the meshing strategies developed are suitable for CFD modeling that can investigate different geometries of RDRE combustors. Ongoing work includes implementing transport property calculations that also use the best practices chosen by NIST, expected to be completed before the end of FY25.

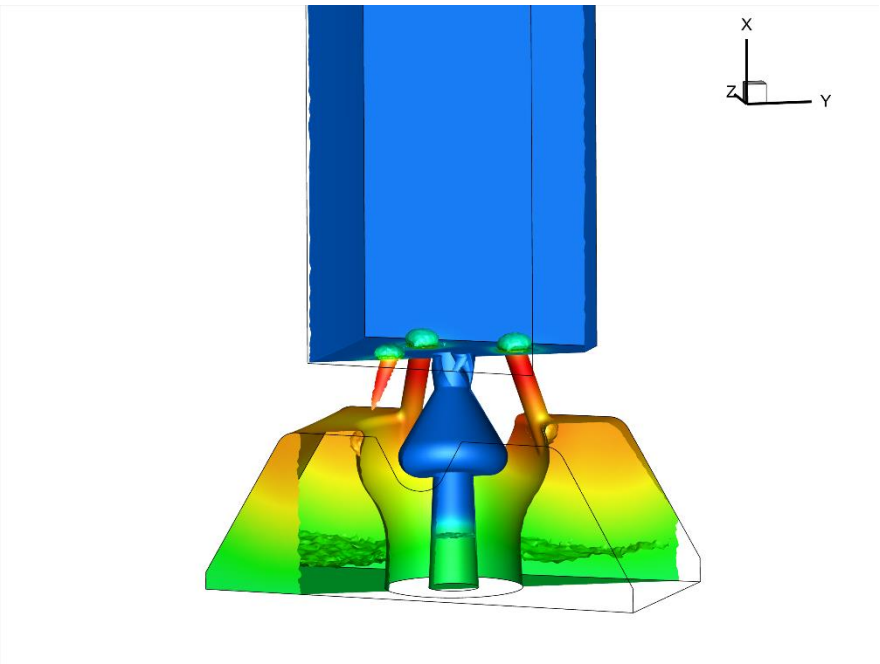

Figure 74 - Initial CFD Results of a Single Injector

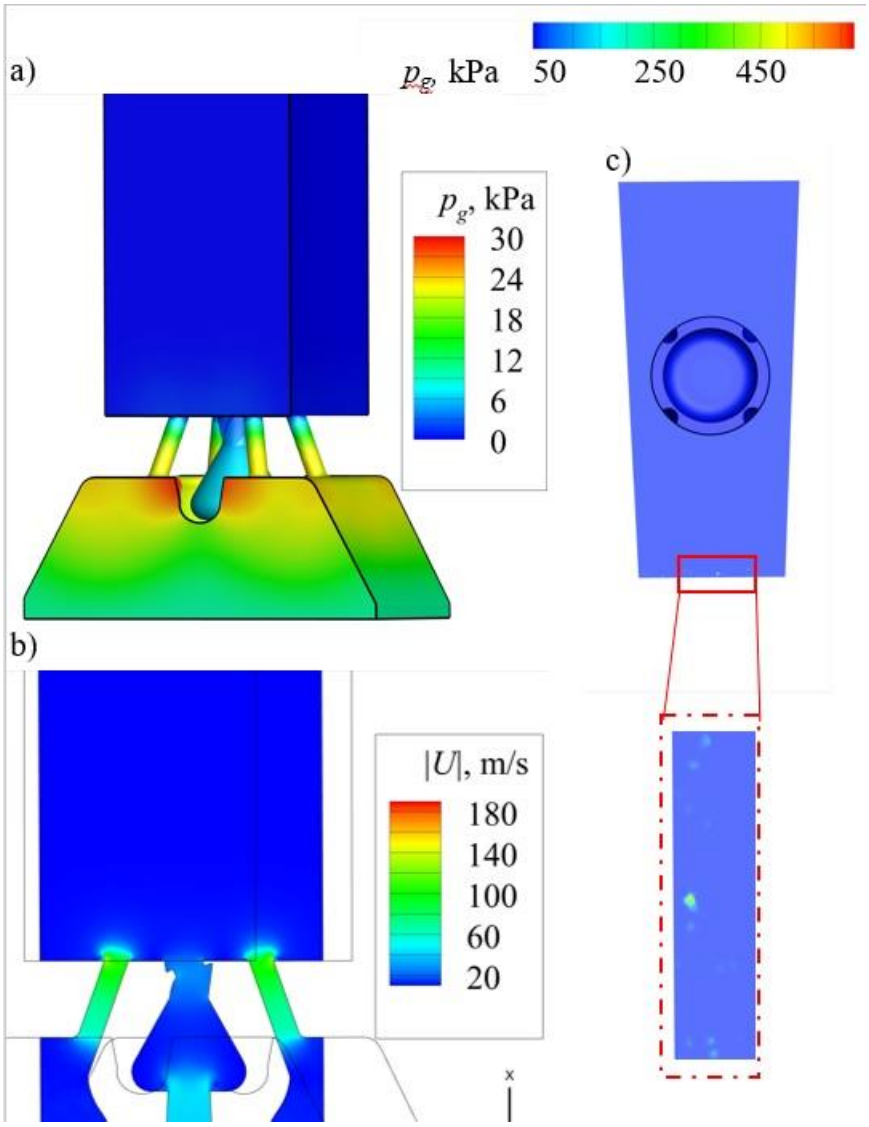

Figure 75 - Cutaway Views of Single Injector

The work conducted over this CFD effort included discussions with Ian Bell from NIST to replicate output from REFPROP. Due to the effort required to create this model in OpenNCC, a number of students from various Universities through OSTEM were brought in as interns for code development and mesh creation. The work involved in the implementation of thermophysical and transport properties could not have been possible without these interns. One of these interns became a part of NASA's Pathways program at Kennedy Space Center for cryogenic modeling for operational systems.

9 CONCLUSIONS

This early career initiative work was conducted over the course of 2 years with experimental data obtained across 7 hot fire test projects. The primary fuels of comparison were methane, hydrogen, and Kerosene. The primary oxidizer was oxygen. Numerous configurations of hardware were evaluated with many direct comparisons made to the existing experimental and computational literature. Each of these are documented and contrasted. The RDRE has been found to be a viable technology for near term infusion into space missions. It offers clear advantages over traditional rocket technology such as compactness of design and completion of combustion and at minimum can yield the same Isp as state-of-the-art liquid rocket engines.

Annulus parameters considered under this work include gap width, contraction ratio or throat area, L', injection stiffness and stiffness ratio, injector elements, injector element scheme, wall profiling or contouring, injector face dead space, and impingement angle. Operability parameters were also considered including average chamber pressure, mixture ratio, propellant mass flux, and injection phase and temperature.

Parameters that do not appear to directly impact combustor Isp include the contraction ratio, impingement angle, available dead space on an injector face, and injection stiffness ratio. Parameters such as average chamber pressure, mixture ratio, propellant, and nozzle configuration impact Isp as would be expected. The nozzle should be a proper aerospike or have an exterior shroud extending a significant length down the plug nozzle for the best Isp. As chamber pressure increases, so does Isp.

More generally speaking, the performance gain to date over traditional rockets appears to be modest compared to theory. Heat flux to the walls of the inner body, outer body, nozzle extensions, and injector face heating have been evaluated and are found to be far higher compared to traditional liquid rocket engines. Critical heat transfer data has been obtained and is reported in this effort giving industry a starting point for the design of their own RDRE.

Many more technology challenges are still present but a great deal of the technology gaps have been addressed including those listed in Table 1. These include steady state operation with flight realistic propellants, self-sustained cooling without the use of water, reduced injector pressure losses, internal and rapid ignition, high thrust, and hardware lifecycle. While the technology is being invested in in the near term for its dramatic length and mass savings, the Isp benefit is showing to be real and will become an enabling feature of the technology. It is expected that in the next decade the RDRE will become a dominant propulsion technology in the space industry.

Much of the critical data mentioned in this work is reported in a separate document and can be released to CUI, ITAR, and export control qualified individuals and institutions.

10 FUTURE WORK

A technology demonstration mission (TDM) project has been funded by NASA Space Technology Mission Directorate (STMD) to investigate integrating turbomachinery with an RDRE thrust chamber assembly. A full engine system demonstration will be conducted near the end of 2028 at Marshall Space Flight Center. Simultaneously, significant development work will be conducted to identify high performing hardware geometries, dependencies on injection temperature, injection pressures, heat flux trends with varying gap widths, and significant modeling activities to identify critical performance trends.

11 ACKNOWLEDGMENTS

Without the support of NASA's Space Technology Mission Directorate, this work would not have been possible. Additionally, collaboration between the RAMBO, ORCA, and RAMPT projects have all greatly advanced RDRE technology and even enabled it. This work has also allowed for numerous early career civil servants and student interns the opportunity to address major challenges with this technology and advance their own understanding of engineering.

12 REFERENCES

[1] T. W. Teasley, D. R. Petty, and M. R. Hemming, “PL155 Test Summary Report for ARDVARC Rotating Detonation Rocket Engine LOX/Methane and LOX/GH2 Testing,” Huntsville, AL, 2022.

[2] T. A. Kaemming and D. E. Paxson, “Determining the pressure gain of pressure gain combustion,” in *2018 Joint propulsion conference*, 2018, p. 4567.

[3] D. E. Paxson, K. Miki, H. D. Perkins, and S. Yungster, “Computational Fluid Dynamic Optimization of an Experimental Rotating Detonation Rocket Engine Nozzle,” in *AIAA AVIATION 2022 Forum*, 2022, p. 4107.

[4] T. W. Teasley, “Test Summary Report for Test Program PJ062 "1.2K GRCop Chamber and HR-1 Nozzle Cycle Testing”,” Huntsville, AL, 2021.

[5] G. P. Sutton and O. Biblarz, *Rocket propulsion elements*. John Wiley & Sons, 2016.

[6] J. W. Bennewitz, B. Bigler, S. Danczyk, W. A. Hargus, and R. D. Smith, “Performance of a rotating detonation rocket engine with various convergent Nozzles,” in *AIAA Propulsion and Energy 2019 Forum*, 2019, p. 4299.

[7] A. R. Keller, A. P. Nair, N. Kuenning, N. Minesi, and R. M. Spearrin, “Annular chamber geometry effects on a hypergolic liquid rotating detonation rocket engine,” in *AIAA AVIATION 2023 Forum*, 2023, p. 4385.

[8] D. P. Stechmann, S. Sardeshmukh, S. D. Heister, and K. Mikoshiba, “Role of ignition delay in rotating detonation engine performance and operability,” *J Propuls Power*, vol. 35, no. 1, pp. 125–140, 2019.

[9] P. R. Gradl, T. W. Teasley, C. S. Protz, C. P. Garcia, and S. E. Greene, “Hot-fire Performance of Additively Manufactured GRCop-42 and GRCop-84 Channel-Cooled Combustion Chambers,” pp. 1–36, 2019.

[10] D. L. Ellis, “GRCop-84: A high-temperature copper alloy for high-heat-flux applications,” 2005.

[11] T. W. Teasley, P. R. Gradl, M. B. Garcia, B. B. Williams, and C. S. Protz, “Extreme Environment Hot Fire Durability of Post Processed Additively Manufactured GRCop-Alloy Combustion Chambers,” in *AIAA Propulsion and Energy 2021 Forum*, 2021, p. 3233.

[12] A. Harroun and S. D. Heister, “Liquid Fuel Survey for Rotating Detonation Rocket Engines,” in *AIAA SCITECH 2022 Forum*, 2022, p. 0088.

[13] S. E. Greene, “Test Summary Report for PJ030: Modified Methane Engine Thrust Assembly for 4K lbf with a 4” Diameter Chamber (META4X4),” Huntsville, AL, 2020.

[14] T. W. Teasley, “Test Summary Report for Test Program PJ062 "1.2K GRCop Chamber and HR-1 Nozzle Cycle Testing”,” Huntsville, AL, 2021.

[15] T. W. Teasley and P. R. Gradl, “PJ116 Test Summary Report - Composite Overwrap Methane Engine Thruster (COMET) GRCop-42 7K lbf LOX/Methane Testing,” Huntsville, AL, 2021.

[16] T. Teasley, “Test Summary Report for PK129: Cycle Testing of GRCop-42 Long Life Additively Manufactured Assembly (LLAMA) 7K lbf Phase 2,” Huntsville, AL, 2021.

[17] T. Teasley, “Test Summary Report for Test Program PK058 & PK129 "Cycle Testing of 7K lbf GRCop-42 Long Life Additively Manufactured Assembly (LLAMA)”,” Huntsville, AL, 2021.

[18] A. Martinez, B. Cabot, K. Blong, T. W. Teasley, and S. D. Heister, “Experimental Study of a Watercooled GOX/RP-1 Rotating Detonation Rocket Combustor for Application to Ox-Rich Staged Combustion Engine Cycles,” in *AIAA SCITECH 2024 Forum*, 2024, p. 2791.

[19] D. H. Huang and D. K. Huzel, *Modern engineering for design of liquid-propellant rocket engines*. American Institute of Aeronautics and Astronautics, 1992.

[20] F. A. Bykovskii, S. A. Zhdan, E. F. Vedernikov, and A. N. Samsonov, “Scaling factor in continuous spin detonation of syngas–air mixtures,” *Combustion, Explosion and Shock Waves*, vol. 53, no. 2, pp. 187–198, 2017, doi: 10.1134/S0010508217020095.

[21] A. Martinez, B. Cabot, K. Blong, T. W. Teasley, and S. D. Heister, “Experimental Study of a Watercooled GOX/RP-1 Rotating Detonation Rocket Combustor for Application to Ox-Rich Staged Combustion Engine Cycles,” no. January, pp. 1–11, 2024, doi: 10.2514/6.2024-2791.

[22] T. W. Teasley, T. M. Fedotowsky, P. R. Gradl, B. L. Austin, and S. D. Heister, “Current State of NASA Continuously Rotating Detonation Cycle Engine Development,” no. January, pp. 1–24, 2023, doi: 10.2514/6.2023-1873.
[23] D. Stechmann, “Experimental Study of High-Pressure Rotating Deontation Combustion in Rocket Environments,” Purdue, 2017.
[24] J. W. Bennewitz, B. R. Bigler, M. C. Ross, S. A. Danczyk, W. A. H. Jr, and R. D. Smith, “Various Convergent Nozzles and Chamber Lengths,” pp. 1–30, 2021.
[25] B. R. Bigler, J. R. Burr, J. W. Bennewitz, S. A. Danczyk, and W. A. Hargus, “Global performance effects of mode transitions in a rotating detonation rocket engine,” *AIAA Propulsion and Energy 2020 Forum*, no. August, pp. 1–15, 2020, doi: 10.2514/6.2020-3852.
[26] J. Sosa, R. Burke, K. A. Ahmed, D. J. Micka, J. W. Bennewitz, S. A. Danczyk, E. J. Paulson, and W. A. Hargus, “Experimental evidence of H2/O2 propellants powered rotating detonation waves,” *Combustion and Flame*, vol. 214, pp. 136–138, 2020, doi: 10.1016/j.combustflame.2019.12.031.
[27] W. Armbruster, B. S. Hermannsson, M. Börner, J. Martin, and J. Hardi, “Experimental Investigation of a Small-Scale Oxygen-Hydrogen Rotating Detonation Combustor,” 2023.
[28] M. L. Fotia, F. Schauer, T. Kaemming, and J. Hoke, “Experimental study of the performance of a rotating detonation engine with nozzle,” *Journal of Propulsion and Power*, vol. 32, no. 3, pp. 674–681, 2016, doi: 10.2514/1.B35913.